The optimisation of a preselection methodology of heterotypic spheroids for the *in vitro* investigation of angiogenesis in lung cancer.

Trinity College Dublin, the University of Dublin

Master of Science in Clinical Medicine

Daniella Anthea de Agrela Gomes. BSc, MSc

22328524

Supervisors

Dr. Adriele Prina Mello

Dr. Dania Movia

2025

Declaration

I declare that this thesis has not been submitted as an exercise for a degree at this or any other university and it is entirely my own work.

I agree to deposit this thesis in the University's open access institutional repository or allow the Library to do so on my behalf, subject to Irish Copyright Legislation and Trinity College Library conditions of use and acknowledgement. I consent to the examiner retaining a copy of the thesis beyond the examining period, should they so wish (EU GDPR May 2018).

Acknowledgements

This work was funded by Breakthrough Cancer Research [Grant Number BCR-MBPhD-0222] I am forever grateful for their generous financial support, which made this research possible. I would like to thank everyone at Breakthrough Cancer Research for their support and training provided. I would also like to acknowledge and appreciate the amazing work they do for researchers and patients.

I would like to extend my deepest gratitude to all the individuals who have contributed to the success of this research project. Special thanks go to the nanomedicine research group. I would also like to thank Dr Stephen Mayer for providing access to western blot equipment and David Hackett for training on conducting western blots. I would also like to thank Dr Anthony McElliot for his kind donation of endothelial cells, without which this project would not have been possible. Additionally, I would like to thank Dr Gina Renata Leisching for her mentorship and assistance.

I would like to thank my supervisors, Dr. Adriele Prina Mello and Dr. Dania Movia, whose guidance, support, and expertise have been instrumental throughout this project. Their mentorship has greatly shaped the direction and quality of the research conducted within this project. I would like to also thank Sive Mullen, a friend and researcher who has always offered support, advice and debate, inside and outside of the lab.

On a personal note, I wish to acknowledge my partner, Stephen Gibson, for his unwavering support, encouragement, and patience throughout this journey. His belief in me has been a source of strength.

Thank you to all who have contributed in any way, both directly and indirectly, to the completion of this work.

Table of Contents

Declaration ii

Acknowledgements iii

Presentations and Modules 7

List of abbreviations viii

List of Figures x

List of Tables xiii

Abstract 1

Lay Abstract 3

1. Introduction 4

1.1. The tumour microenvironment in non-small cell lung cancer. 4

1.2. 3D Cell Models 6

1.2.1. Tumour spheroids as a basic 3D model 7

1.2.2. Tumour Angiogenesis 11

1.2.3. Mechanisms of angiogenesis in NSCLC 13

1.2.4. The role of fibroblast in the angiogenic process in NSCLC 15

1.2.5. Project rationale 16

1.3. Hypothesis and Aims 18

2. Materials and methods 19

2.1. Cell culture, preparation, handling and cryopreservation 21

2.1.1. Cell Lines 21

2.1.2. Mycoplasma testing 21

2.1.3. Cell subculture 22

2.1.4. Cryopreservation of cell lines 22

2.1.5. Cell count using Trypan blue exclusion. 23

2.1.6. 3D spheroid formation using ULA plates. 24

2.2. Morphological assessment of Spheroids using Brightfield Microscopy 25
2.2.1. FIJI image analysis 25
2.2.2. MATLAB image analysis 27
2.3. Viability Assessment of Spheroids 29
2.3.1. Cell proliferation 29
2.3.2. Spheroid Dissociation 30
2.3.3. ATP quantification 30
2.4.1. Immunofluorescent Microscopy 31
2.5. Western blotting 32
2.5.1. Preparation of cell lysates from 3D spheroids 32
2.5.2. Quantification of Protein Content in spheroid cell lysates 32
2.5.3. Sample preparation 33
2.5.4. SDS-PAGE gel electrophoresis 33
2.5.5. Protein transfer 33
2.5.6. Blocking 34
2.5.7. Primary Antibody and secondary antibody 34
2.5.8. Detection 34
2.6. Statistical Analysis 35
3. Results 36
3.1. Co-culture optimisation 36
3.1.1. Optimisation of cell media for co-cultures 36
3.2. Spheroid Morphology 37
3.2.1. Brightfield images of spheroids captured using the Lionheart Fx microscope. 37
3.2.2. Spheroid Morphology Characteristics 43
3.3. Cell Number Quantification and Viability Using Flow Cytometry 49
3.4. Cell viability using Trypan Blue Exclusion 52

3.5. Cell Viability using ATP Quantification using CellTiter-Glo® 53
3.6. Internal characteristics using Immunofluorescent microscopy.....56
3.7. Confirmation of VEGF-A and HIF-1α expression using western blot.....61
4. Discussion.....62
4.1. Limitations.....74
5. Conclusion.....75
5.1. Future Outlook.....76
6. References.....78
Appendix I – Methodology used to generate multivariate graphs.....86
Appendix II – Flow cytometry gating 87
Appendix III -Confirmation of spheroid dissociation using brightfield imaging of haemocytometers:.....88
Appendix IV – Gel preparation for western blot.....88
Gel preparation. 88
Appendix V – Additional spheroid images 90
Appendix VI – Standard curve for BCA.....91
Appendix VII –Full western blot image 91

Presentations and Modules

- TSJCI Christmas Research Blitz– 8 December 2023
- Patient and Public Involvement (PPI) engagement with BCR – 7th June and 19 October 2023
- CA7000 – Research integrity and impact in an open scholarship era (5 ECTS) – Completed December 2022
- Key Skills for Biomedical Research Module (5 ECTS) – Completed March 202

List of abbreviations

2D	2 dimensional
3D	3 dimensional
A549	Human Lung Adenocarcinoma cell line
AnaSP	Analysis of SPheroids
ANG-1	Angiotensin-1
ATP	Adenosine triphosphate
CAF	Cancer associated fibroblast
CD31	cluster of differentiation 31
DMEM	Dulbecco's Modified Eagle Medium
DMSO	Dimethyl sulfoxide
EC	Endothelial cell
ECM	Extracellular matrix
FGF-2	Fibroblast Growth Factor-2
HIF-1α	Hypoxia-inducible factor-1α
HUVEC	Human umbilical vein endothelial cell
IL-8	Interleukin-8
IMS	Industrial methylated spirits
Ki-67	Antigen Kiel 67
LSCM	Laser scanning confocal microscopy
MATLAB	matrix laboratory
MEF	Mouse Embryonic Fibroblasts
MEM	Minimum Essential Media
MMPs	Matrix metalloproteinase

MRC-5	Medical Research Council cell strain 5
NSCLC	Non-small cell lung cancer
PBS	Phosphate-buffered saline
PD1	programmed cell death protein 1
PEG	polyethylene-glycol
PI	Propidium iodide
PMSF	Phenylmethyl Sulfonyl Fluoride
TAC	Tacrine
TME	Tumour microenvironment
ULA	Ultra low attachment
VAL	valinomycin
VEGF	Vascular endothelial growth factor
VEGF-A	Vascular endothelial growth factor - A
VEGF-B	Vascular endothelial growth factor - B
VEGF-R1	Vascular endothelial growth factor – Receptor 1
VEGF-R2	Vascular endothelial growth factor – Receptor 2
α-SMA	Alpha smooth muscle actin

List of Figures

Figure 1.1 The flow-chart of the image-based approach proposed by Zanoni *et al.*

Figure 1.2 An overview of vascularisation and angiogenesis.

Figure 2.1 Workflow for the formation, selection, and characterisation of spheroids.

Figure 2.2 Visual representation of the Fiji settings used to adjust the threshold to encompass the spheroid as 1 particle.

Figure 2.3 Visual representation of the FIJI settings used to measure and analyse the spheroid.

Figure 2.4 Representative images of the analysis process used in FIJI.

Figure 2.5 Visual representation of the AnaSP software interface used to analyse spheroids.

Figure 2.6 Example of the gating used for flow cytometry.

Figure 3.1 Viability of A549 cells (A) and MRC-5 cells (B).

Figure 3.2 Representative images captured on the lionheart FX Microscope.

Figure 3.3 Brightfield images of A549 spheroids taken at various time points using the Lionheart FX Automated Microscope.

Figure 3.4 Brightfield images of MRC-5 spheroids taken at various time points using the Lionheart FX Automated Microscope.

Figure 3.5 Brightfield images of A549-MRC-5 heterotypic spheroids taken at various time points using the Lionheart FX Automated Microscope.

Figure 3.6 Brightfield images of A549 spheroids (A), HUVEC spheroids (B) and Heterotypic spheroids composed of A549, MRC-5 and HUVECs (C).

Figure 3.7 Graphs displaying the circularity of different seeding densities of A549 (A) and MRC-5 (B) spheroids and different ratios of A549:MRC-5 (C) spheroids measured after 1, 4, 8 and 12 days of growth using AnaSP software.

Figure 3.8 3D morphology graphs displaying the circularity, Solidity and Diameter measurements of homotypic A549 (A) and MRC-5 (B) spheroids.

Figure 3.9 3D morphology graphs displaying the circularity, Solidity and Diameter measurements of A549-MRC-5 heterotypic spheroids with a ratio of 1:1 (A) 2:1 (B) 5:2 (C) and 1:2 (D).

Figure 3.10 Graph displaying the circularity of homotypic and heterotypic spheroids.

Figure 3.11 3D morphology graphs displaying the circularity, Solidity and Diameter measurements of A549-MRC-5-HUVEC heterotypic.

Figure 3.12 Flow Cytometry Population Analysis of A549 and MRC-5 Cells.

Figure 3.13 Viability as a percentage generated from PI staining of A549 (A) and MRC-5 (B) cells.

Figure 3.14 Viability as a percentage generated from PI staining of 4 day old A549-MRC-5 heterotypic spheroids compared to 4 day old homotypic spheroids (5000 cells/well/cell line).

Figure 3.15 Flow Cytometry Population Analysis of A549 and MRC-5 spheroids.

Figure 3.16 Cell viability as a percentage (%) derived from the trypan blue exclusion.

Figure 3.17 Graph displaying the mean relative ATP luminescence of A549 (A) and MRC-5 (B) spheroids seeded at different densities.

Figure 3.18 Graph displaying the mean relative ATP luminescence of A549 and MRC-5 heterotypic spheroids at varying rations of A549: MRC-5 cells.

Figure 3.19 Graph displaying the mean relative ATP luminescence of tri-cultured heterotypic spheroids at different time points.

Figure 3.20 Confocal images of A549, MRC-5 and heterotypic spheroids stained with Hoechst, Rhodamine phalloidin and Ki-67.

Figure 3.21 Confocal images of 4 day old A549, MRC-5 and heterotypic spheroids stained with Hoechst, Rhodamine phalloidin and α-SMA.

Figure 3.22 Confocal images of 4 day old A549, MRC-5 and heterotypic spheroids stained with Hoechst, Rhodamine phalloidin and CD31.

Figure 3.23 Confocal images of 4 day old A549, MRC-5 and heterotypic spheroids stained with Hoechst, Rhodamine phalloidin and HIF-1α.

Figure 3.24 Western blot for HIF-1α and VEGF-A. Cell lysates were harvested from 16 tri-cultured heterotypic spheroids grown for 4,8,12 and 16 days.

Figure 6.1: Results extracted from Zanoni *et al* which indicates the impact of spheroid shape on viability.

Figure 6.2 Image showing the development of hypoxia in growing spheroids.

Figure II.1 Flow cytometry sample gating.

Figure III.1 Representative brightfield image showing the dissociation of a spheroid.

Figure V.1 Additional images of A549 - MRC-5 spheroids with a ratio of 1:1 to show consistency in the production of spheroids.

Figure VI.1 Standard Curve for the BCA assay

Figure VII.1: Unedited Images of western blot.

List of Tables

Table 2.1 Exclusion and inclusion criteria used for preselecting spheroids.

Table 2.2 Primary antibodies used in immunofluorescent staining of spheroids

Table 2.3 Counter stains used in immunofluorescent staining of spheroids

Table 2.4 Primary antibodies used for protein quantification

Table IV.1 Low molecular weight proteins need a higher gel percentage.

Table IV.2 Reagents and quantities used to make specific percentages of resolving gel for western blots

Table IV.3 Reagents and quantities used for the stacking gel for western blots

Abstract

Lung cancer, particularly non-small cell lung cancer (NSCLC), is a leading cause of cancer-related deaths. Angiogenesis, the formation of new blood vessels, is essential for disease progression. The tumour microenvironment significantly influences angiogenesis in NSCLC. Despite challenges in accurately modelling lung anatomy, current *in vitro* 3D cell models can provide insights into NSCLC interactions and potential therapeutic targets. 3D cell model advancements such as heterotypic spheroids have led to more relevant models for tumour growth mechanism study. However, determining if spheroids are well-formed for consistent use in subsequent experiments or complex cell models such as lung-on-a-chip needs to be addressed.

This study is aimed to develop a 3D spheroid model made of multiple cell lines as tools for investigating the angiogenic switch, which is known to trigger the rapid growth of malignant cells in association with new blood vessel formation. Tumour spheroids, self-assembling structures composed of multiple cells, can replicate key tumour features compared to 2D cultures. The hypothesis behind the proposed multicellular 3D spheroids for the lung is that the spheroids can facilitate early expression of angiogenic markers in complex models and was evaluated by assessing spheroid morphology, viability, proliferation, hypoxia, and angiogenic marker expression. Viability assessment of homotypic and heterotypic spheroids showed stable ATP production, indicating sustained cell viability.

Preselecting spheroids based on size and morphology, such as circularity and solidity, minimises variability in experimental outcomes. This study highlights that larger spheroids (≥ 400 μm) with uniform morphology are critical for replicating hypoxic conditions in NSCLC models. Co-culturing A549 spheroids with MRC-5 fibroblasts enhances ECM formation and spheroid aggregation, improving the physiological relevance of these 3D models. Immunofluorescence staining and western blot analysis preliminary confirmed increased HIF-1α expression. It demonstrates spheroid size correlates with hypoxia and supports the use of this model for studying tumour microenvironments.

In conclusion, my work demonstrates that by precisely controlling the cell seeding parameters (cell types, densities and ratios), it is possible to fabricate highly reproducible tumour spheroid models that mimic key aspects of the tumour.

Graphical Abstract

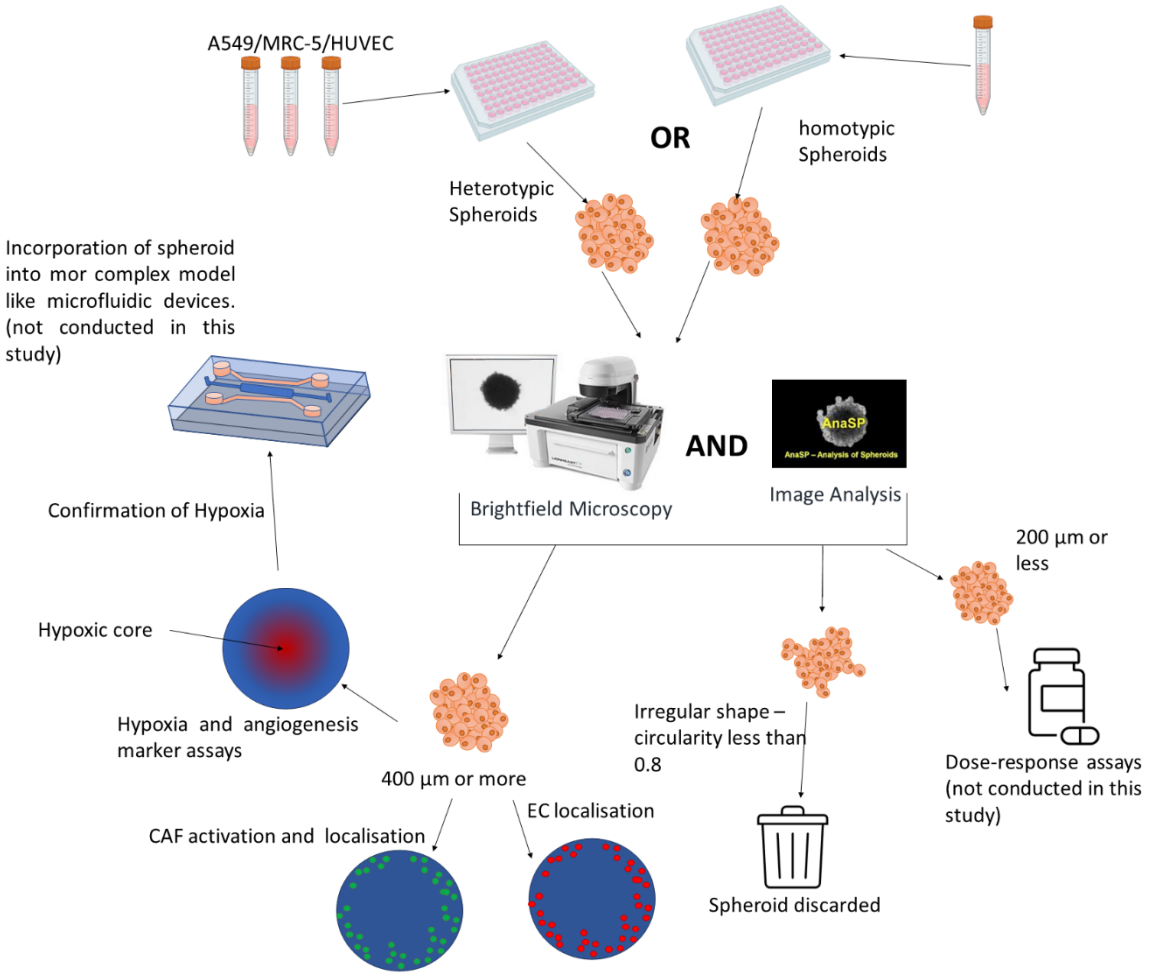

A graphical abstract for my project. The schematic shows a top-down approach on how the optimisation of the preselection methodology for homotypic and heterotypic spheroids for the *in vitro* investigation of angiogenesis in lung cancer is constructed. After the homotypic and heterotypic spheroids are put together and imaged under different conditions the use of AnaSP software assists in the selection and exclusion of homotypic and heterotypic spheroids that are irregular in shape (circularity of less than 0.8) and are more than 400 µm. Spheroids that met the criteria were then assessed for CAF activation and localisation, EC localisation and the expression of hypoxic and angiogenic markers. This should be the first steps in the process of developing more complex models like microfluidic devices that can be used to research angiogenesis in NSCLC.

Lay Abstract

Lung cancer, particularly non-small cell lung cancer (NSCLC), is a leading cause of cancer-related deaths. Angiogenesis—the formation of new blood vessels—is crucial for its progression. This study aims to develop three-dimensional (3D) spheroid models made from various cell types to investigate how new blood vessel formation begins, known as the "angiogenic switch." By creating these models, we can better simulate the tumour environment compared to traditional two-dimensional cultures. This research highlights the importance of larger, well-formed spheroids in replicating the conditions of lung cancer.

Results showed that combining lung cancer cells with normal fibroblast cells enhances the relevance of these models, making them more similar to actual tumours. Larger spheroids displayed characteristics associated with low oxygen levels, which are common in cancer, indicating that they effectively mimic tumour conditions. Using techniques like immunofluorescence staining, it was confirmed that spheroid size correlates with key hypoxia-related markers. This work shows that precise control over cell arrangements can lead to reliable 3D cell models for studying lung cancer and testing new treatments.

1. Introduction

Between 2019 and 2021, the National Cancer Registry of Ireland determined that the average annual cancer incidence was 41,767 cases [1]. Among males, lung cancer was ranked as the third most frequently diagnosed type of cancer; while among females, it was the second most common [1]. Furthermore, lung cancer contributed to 21% of male and 19% of female deaths related to cancer during the same period [1]. Lung cancer can be classified into two main types: small-cell lung cancer and non-small-cell lung cancer (NSCLC) [2]. NSCLC is the more common type, accounting for 82% of all cases [2-4]. Adenocarcinoma is the most common subtype, accounting for 40% of NSCLC cases, whilst squamous cell carcinoma accounts for 30% and large cell carcinoma accounts for 10-15% [5].

Angiogenesis significantly impacts tumour growth and progression in NSCLC [5]. Angiogenesis, the development of new blood vessels from pre-existing ones, is widely recognised as a crucial factor in tumour progression and metastasis [6]. Lung adenocarcinoma is particularly associated with increased angiogenesis in NSCLC [7]. Despite the significant efforts made to progress the understanding of tumour growth mechanisms, the interaction between tumours and vasculature is much less understood. There is a strong need for tools that enable research into tumour-vasculature mechanisms to support the development of new treatments [8]. 2D cell cultures are traditionally used for *in vitro* drug discovery and screening, but they are not the most effective method for investigating the influence of mechanical, biomedical, and tumour microenvironment factors.

1.1. The tumour microenvironment in non-small cell lung cancer.

Lung adenocarcinomas account for 50% of all NSCLCs and displays extensive cellular and mutational heterogeneity that spans across the tumour microenvironment (TME) of lung adenocarcinomas. The TME of lung adenocarcinomas plays a critical role in tumour development. Different microenvironments are observed in the proximal and distal lung, especially regarding the composition of the formed extracellular matrix (ECM). As with most tumours, lung adenocarcinomas have the capacity to recruit stromal cells that then aid in ECM formation. One stromal cell type that has a significant role in tumour progression in NSCLCs are fibroblasts [9]. Stromal cells, including fibroblasts, that infiltrate

the TME are often reprogrammed by the hypoxic conditions of the TME mediated by HIF-1α.

Fibroblasts are activated into cancer associated fibroblasts (CAFs) in response to hypoxia through Hypoxia-inducible factor 1α (HIF-1α). Some studies have demonstrated the importance of HIF-1α on fibroblast activation by inducing HIF-1α expression in mouse embryonic fibroblasts (MEF) with and without HIF-1 knock outs [10]. Results indicated that HIF-1α knock out fibroblasts exhibited no response to hypoxia and had no change in the expression of CAF markers [10]. CAFs recruited into the TME develop the ability to produce ECM proteins, growth factors and cytokines. This allows the various components of the TME to respond and regulate each other to construct the scaffolding that forms the tumour ECM. The modified ECM displays a phenotype which aids tumour progression, fibronectin and collagen offer physical support and stiffness whilst proteoglycans bind growth factors and cytokines [11]. Additionally, fibronectin has been shown to play a key role in angiogenesis, showing the importance of Lung CAFs are capable of mediating several process in tumour progression including proliferation, metastasis, drug resistance and angiogenesis through several different pathways and signalling cascades [9, 11]. Research indicates that CAFs from NSCLCs show increased glycolytic metabolism and autophagy, however, the significance of this remains unclear. Furthermore, CAFs isolated from NSCLCs express the programmed cell death protein 1 (PD1) receptor that in turn suppresses T cell functions [9].

In addition to CAFs, the TME of NSCLCs show enhanced ECM-mediated signalling that promotes tumour growth. Furthermore, lung adenocarcinomas have been shown to have a loss of function mutation in the tumour suppress gene LKB1. This loss of function has been associated with the upregulation of specific ECM proteins such as lysyl oxidase which can then facilitate the crosslinking of collagen with β1 integrin. However, most of what is understood about the TME in NSCLC has been established through mouse models, limiting the applicability to humans and as a result the mechanistic functions of angiogenesis and ECM formation in lung tumours is still not fully understood. In addition to ECM formation, CAFs can mediate angiogenesis by stimulating the upregulation of VEGF in tumourigenic cells through paracrine signalling, further promoting angiogenesis [12]. Understanding the impact of the TME on tumour angiogenesis in NSCLC is crucial for developing effective therapeutic strategies that can target tumour cells and angiogenesis [9].

1.2. 3D Cell Models

In vitro modelling has provided researchers with a valuable tool to mimic the cellular and molecular interactions involved in tumour angiogenesis. Through the use of *in vitro* systems, researchers have been able to explore the molecular mechanisms underlying angiogenesis and the surrounding tumour microenvironment (TME), assess the effects of several factors, including growth factors and inhibitors, on tumour angiogenesis, and evaluate the efficacy of potential therapeutics [13-16]. Furthermore, *in vitro* models provide a cost-effective and time-efficient approach, reducing the need for animal models and allowing for high-throughput screening of drugs and compounds. With the advancements in the making of *in vitro* three-dimensional (3D) cell models (from here onwards referred to as 3D models) and their assembling techniques, it is possible to gain even better insights into the cellular and molecular processes that drive tumour angiogenesis in NSCLC [14, 17].

It is widely accepted that human cells cultured in 2D models display abnormal behaviours including flattened morphology, altered polarisation, loss of differentiated phenotype and skewed pharmaceutical response [18, 19]. Furthermore, tumour progression is heavily influenced by the spatial structure and 3D organisation of the TME, with signalling cascades by tumour-associated cells influencing the rate of progression. 2D cultures often lack the ability to mimic these interactions and therefore respond to pharmaceutical agents differently than patients would [18-21]. These limitations can be overcome by employing human-specific 3D preclinical cellular models. 3D models can provide a more accurate representation of the interactions between tumour cells, endothelial cells (ECs) and other components of the microenvironment [18, 20, 23]. Moreover, as compared to *in vivo* studies, these models allow for the study of angiogenesis in a more controlled environment, providing researchers with the means to manipulate specific factors and assess their impact on tumour growth and angiogenesis [22].

Bazou *et al* have shown that developing 3D models that offer vasculature, tumourigenic tissues derived from both mice and patient explants could be cultured long-term. This offers the opportunity to develop patient-specific treatments [23]. This further shows how fundamentally important it is to develop models that incorporate angiogenesis and vasculature. As the technology used to form these models improves, the complexity of the

models can increase which further allows the models to more accurately mimic human tumour angiogenesis within the lungs. By developing novel models such as microfluidic systems seeded with heterotypic spheroids and organoids, researchers can further investigate the mechanisms of lung tumour angiogenesis, whilst also optimising anti-angiogenic therapeutic strategies that target the tumour vasculature. Bazou et al have shown this by developing a PDMS microfluidic device capable of showing angiogenic sprouting of HUVEC cells which can then be exposed to shear stress [24]. This highlights the benefits of using 3D models to investigate angiogenesis as physiological factors such as shear stress can be incorporated. Furthermore, scaffold based models which are capable of incorporating hydrogels to mimic the ECM are being developed. Hydrogels are a gel-like matrix that can mimic the ECM that surrounds and supports tissues. The development of sophisticated hydrogels has ultimately allowed the advancement of models that are more physiologically relevant, mimicking the growth dynamics seen *in vivo*. Hydrogels provide researchers with a versatile matrix that are capable of being customised [18]. Hydrogel scaffolds can be both non-synthetic or synthetic, with synthetic scaffolds often providing a more controlled and user defined matrix [18, 25, 26].

Synthetic hydrogel scaffolds using polyethylene-glycol (PEG) have been used to mimic the ECM for angiogenesis studies with promising results, replicating the basic physiological properties of the ECM without contribution biochemically [18, 25, 26]. Furthermore, PEG allows for more user defined designs including crosslinking chemistry and ligand presentation to cells [18, 25]. Although collagen I or fibrin non-synthetic hydrogel scaffolds have been used in angiogenesis investigations, batch to batch variability and unknown compositions limits their application [18]. However, research using synthetic hydrogels with RGD motifs have shown that NSCLC cell lines are capable of being incorporated into tumour angiogenesis models [27]. This research showed that some NSCLC cell lines when grouped by genetic mutations take longer to inhibit growth and secrete the lowest amount of VEGF and FGF-2. This is indicative of a less aggressive tumour that grows slower and is not angiogenic

1.2.1. Tumour spheroids as a basic 3D model

Spheroids are one of the basic methods used to reproduce some of the phenotypes of functional tumours and are self-assembling aggregated structures that can be composed of multiple cell types which are capable of resembling the architecture and biological

characteristics of solid tumours [16]. Spheroids have emerged as a promising tool for investigating cellular behaviour, cell-cell interactions and to screen for drug delivery platforms [28]. They have been used extensively as tools to investigate fundamental biological research questions in cancer research as well as drug screening [29]. The earliest publication of an *in vitro* 3D model of the lungs dates back to 1961, where the hanging drop technique was used to create spheroids of lung cells [30]. Spheroids can exhibit typical features and key hallmarks of tumours including sustained proliferative signalling better than that of 2D cultures [31, 32]. These simple cell aggregates are capable of replicating the *in vivo* features such as hypoxia and reduced response to therapeutics [32, 33].

Additionally, heterotypic spheroids have been used to investigate the tumour-stromal cell interactions as they enable gradient formation, complex cell-to-cell interactions and cell-extracellular matrix (ECM) adhesions [16, 33, 34]. With increasing complexity by incorporating 2 or more cell lines, heterotypic spheroids have further assisted the understanding of tumour-stroma interaction, therapy resistance and mechanistic functions [33, 34]. For example, heterotypic spheroids of tumour cells with fibroblasts have demonstrated more *in vivo-like* architecture and gene expression and exhibit enhanced angiogenic potential compared to homotypic spheroids [16]. Amann *et al* indicated that 3D models of NSCLC that incorporate the co-cultures of tumour cells and cancer-associated fibroblasts (CAFs) can promote angiogenesis, effectively mimicking the TME of NSCLC and angiogenesis when combined with ECs [35].

The use of spheroids in angiogenesis research was first introduced in 1998, where ECs were cultured into spheroids to better imitate *in vivo* TME to research the response of ECs [36]. ECs were seeded with medium containing 20% methocel (water-soluble cellulose ethers) into non-adherent culture dishes, spheroids were spontaneously formed after 4 h. Methocel prevents cell attachment, forcing cells to aggregate. This research showed that ECs spontaneously organise into 2 compartments, an inner core of unorganised cells that overtime recedes due to apoptosis and an outer layer of differentiated, quiescent and elongated cells [36]. Quiescent cells in the outer layer were shown to be sensitive to angiogenic stimulation, similar to that seen with *in vivo* ECs in blood vessels. Furthermore, the inner core could be kept viable when treated with vascular endothelial growth factor (VEGF) and fibroblast growth factor-2 (FGF-2). This research showed that in addition to better mimicry of *in vivo* conditions, EC spheroids treated with VEGF maintained the

expression of CD34. CD34 is a surface molecule expressed by most *in vivo* ECs, predominantly in larger blood vessels such as arteries and veins [37]. The expression of CD34 on ECs is largely associated with proliferation as a differentiation antigen which is often downregulated when ECs are transferred to *in vitro* cultures [36, 37]. Therefore, ECs that are CD34 positive have a greater capacity to proliferate. Furthermore, ECs transferred to *in vitro* cultures which are CD34 positive have been shown to exhibit more characteristics that are in line with EC tip cells, indicating the importance of CD34 expression in angiogenesis [37, 38].

One of the key aspects taken into consideration when assessing the quality of spheroids is morphology. The morphology of spheroids, specifically their shape and size can have a crucial influence on the response of spheroids to therapeutic treatments. It has been suggested that variability in these parameters may contribute significantly to inconsistent and unreliable experimental outcomes [13, 15, 39, 40]. However, 3D models that incorporate tumour spheroids rarely instil a preselection method. Consequently, these studies do not account for the variation in their morphology which can significantly impact their internal features. [15, 39, 41]. Establishing the parameters of homogeneous shape and size is challenging, especially with heterotypic spheroids as the interactions between cell lines could affect spheroid morphology. Therefore, establishing a set of consistent parameters is a fundamental aspect of developing a novel model that uses spheroids. This enhances reproducibility and reliability in the 3D model used. It is therefore important for spheroids to undergo a screening process using a systemic approach, such as a pre-screening method which considers consistent parameters like circularity, to address their variability. This is necessary if the scientific community wants to increase the biological relevance of data obtained from these models [15]. Thus, establishing a set of consistent parameters will allow the user to select spheroids, which meet certain criteria, before advancing to more sophisticated experiments or models. Zanoni *et al* have suggested that volume and shape, including circularity, are parameters that can be rapidly assessed through the use of software like Analysis of Spheroids (AnaSP) to preselect spheroids to maintain homogeneity amongst the spheroids used in subsequent assays (figure 1.1) [15].

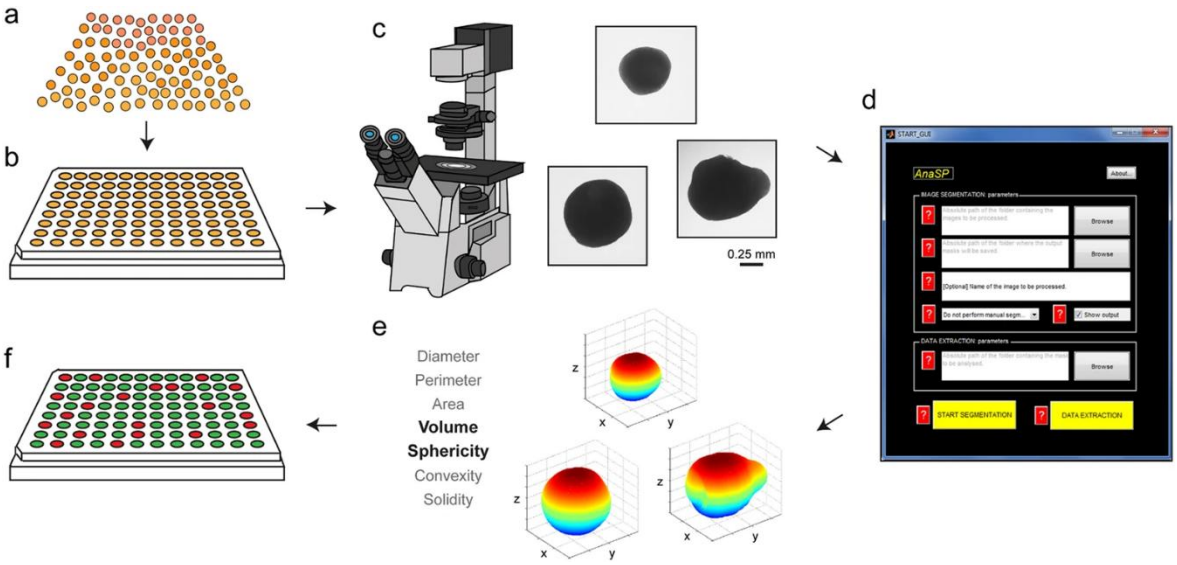

Figure 1.1: The flow-chart of the image-based approach proposed by Zanoni *et al.* Image extracted from (Zanoni, et al., 2016). [15].

Additionally, Lee *et al* show that compactness and diameter can be assessed using AnaSP to select spheroids that were more likely to have developed a necrotic core [42]. The use of specific parameters is therefore dependent on the requirements of the user, for example, if the requirements are that spheroids have a necrotic core, compactness can be used, or if homogenous spheroids are the aim, circularity can be used. whilst circularity, solidity and diameter are key morphology characteristics which can be used as a preselection method, spheroids also have several other key characteristics. These characteristics include proliferative capacity, gene expression, and response to treatments. The proliferative capacity and growth kinetics of spheroids are a key characteristic. the cell heterogeneity of spheroids results in differences in growth kinetics, where the outer layers proliferate at a faster rate compared to the inner core regions. This is a significant feature of spheroids which aid in their mimicry of *in vivo* tumours [43, 44]. Furthermore, gene expression profiles of spheroids are often altered compared to 2D cultures, where spheroids demonstrate upregulation of genes related to hypoxia, angiogenesis and invasiveness [45, 46]. These expression profiles are more reflective of the *in vivo* TME compared to 2D cultures and thus are more suitable for investigating tumour-stromal interactions involved in angiogenesis. Additionally, the expression of ECM proteins within spheroids further contributes to their physiologically relevant response to treatments, including anti-angiogenic agents [9, 45-47].

Spheroids grown with NSCLC cells such as A549 cells, a Human Lung Adenocarcinoma cell line, and lung fibroblasts such as MRC-5 cells have the potential to upregulate angiogenic

factors such as vascular endothelial growth factor–A (VEGF-A) in response to hypoxia [48, 49]. In addition, MRC-5 cells interacting with A549 cells could become activated into CAFs [10, 12, 50, 51]. Therefore, incorporating both cell lines into a spheroid model may more accurately represent the *in vivo* conditions of early onset NSCLC and its angiogenic potential. Furthermore, HUVECs, an EC cell line, can be co-cultured with A549 and MRC-5 cells to investigate the interaction between the 3 cell lines and provide some insight into their interactions *in vivo*. As spheroids are often being incorporated into more complex culture systems, understanding these interactions and the angiogenic potential of tri-cultured heterotypic spheroids, more complex models to investigate angiogenesis in NSCLC can and should be developed.

1.2.2. Tumour Angiogenesis

Mammalian cells are typically 100 to 200 µm from blood vessels to be within oxygen diffusion distances [52]. Solid tumours begin as a small cluster of mutated cells that can only proliferate until they reach a distance of 100 to 200 µm from a blood supply, at which point an independent blood supply becomes necessary to sustain further growth. [52-54]. As tumours proliferate, the inner core becomes hypoxic and necrotic (figure 1.2A). This tips the balance of angiogenic growth factors within the cellular microenvironment towards pro-angiogenic factors in a process known as the angiogenic switch [52-54].

Homeostatic angiogenesis processes affect ECs. ECs line blood vessels in a monolayer and are connected by tight junction molecules (figure 1.2B). Pericytes, which are cells present at intervals along the walls of capillaries stabilise the blood vessel structure. In response to pro-angiogenic factors including VEGF-A, pericytes detach from the vessel wall. This is mediated by the degradation of the local extracellular matrix (ECM) that forms the basement membrane of blood vessels [53, 55, 56]. The process of basement membrane degradation is facilitated by metalloproteinases (MMPs). The tight junctions between ECs are then loosened, which increases vessel permeability allowing plasma proteins to leak from the vessel. This results in a provisional matrix that facilitates EC migration guided by angiogenic factor gradients (figure 1.2C). The migrating ECs may differentiate into two distinct phenotypes, a “tip” or a “stalk” phenotype, where tip cells lead the migration using filopodia to detect chemical cues within the microenvironment [57]. Stalk cells can then proliferate behind the tip cells to elongate the forming sprout [58]. These sprouts are then stabilised by angiopoietin-1 (Ang-1) which aids in EC chemotaxis and promotes the

recruitment and association of pericytes [58]. ECs can then form tight junctions and develop a continuous closed lumen which allows perfusion. Vessels that are incorrectly perfused will recede over time.

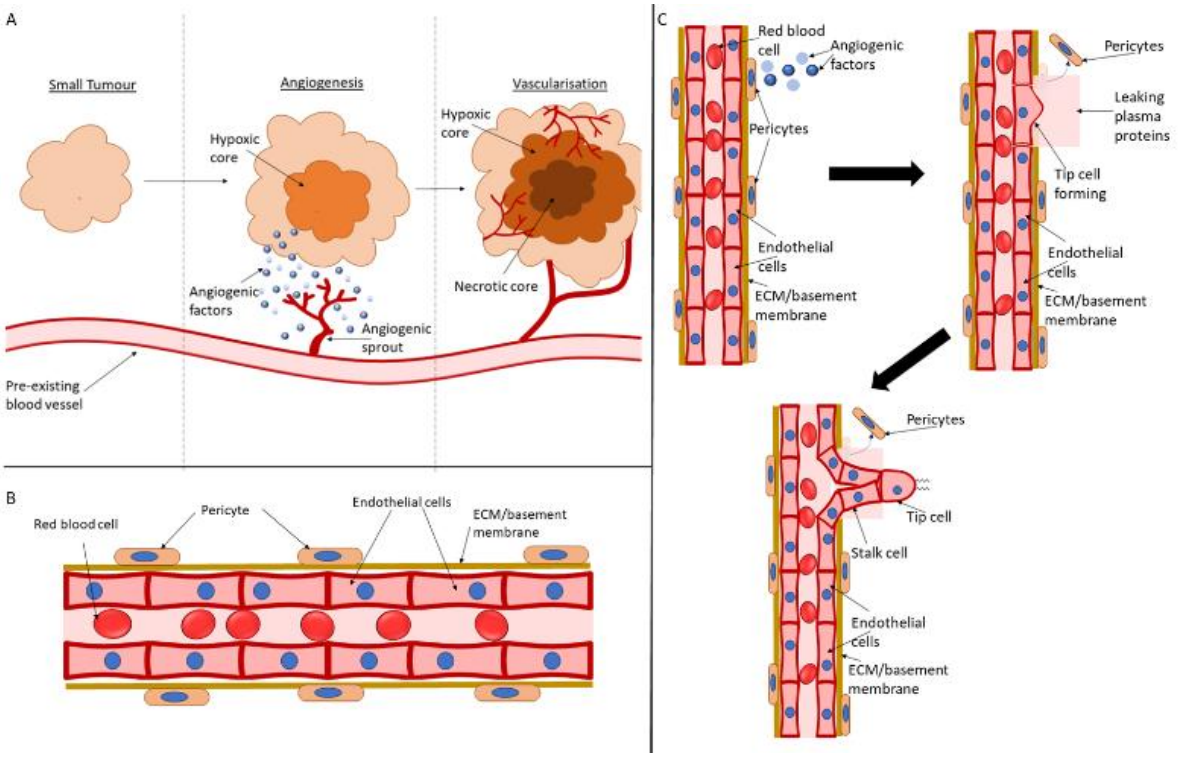

Figure 1.2: An overview of vascularisation and angiogenesis. A. Tumours start as small clusters of cells that will continue growing until the diffusion distances limit the nutrients and oxygen that can enter the mass centre. This hypoxic core secretes angiogenic factors that stimulate the formation of angiogenic sprouts. The tumour then becomes vascularised over time. B. the structure of a typical blood vessel. Blood vessels are lined with a monolayer of ECs and are stabilised by pericytes that produce the ECM that forms the basement membrane. C. A summary of the angiogenic process on blood vessels shows the basement membrane breakdown, detachment of pericytes, the leaking of plasma proteins to provide a provisional matrix on which ECs can migrate and the forming of tip and stalk cells.

In tumour-induced angiogenesis, the angiogenic cascade starts in response to tumour hypoxia and stimulates the migration of ECs as seen in normal angiogenesis. However, due to the continuous stimulation of angiogenesis, immature vessels do not recede, resulting in dysregulated vessel formation. This affects the structure and functionality of the tumour vasculature, resulting in often dilated and haemorrhagic vasculature with many vessels leading to dead ends [52]. ECs that form tumour vasculature show upregulated angiogenic activity and increased resistance to chemotherapeutics and anti-angiogenic drugs [59, 60]. Furthermore, ECs associated with tumours are more motile and have increased adhesion molecules compared to ECs isolated from normal tissue. Research supports the idea that tumour vasculature plays a significant role in clinical prognosis, for example, studies have demonstrated that in early breast cancer, patients with highly vascular tumours often have

a worse prognosis [61]. Studies have shown that ECs isolated from lung microvasculature have a restrictive barrier compared to vasculature from other tissue types [62-65]. Furthermore, ECs within the lungs are highly heterogeneous dependent on the type of vasculature they are derived from [63-66].

It is well-established that angiogenesis plays a significant role in NSCLC and tumour progression [63-65, 67]. Several studies have demonstrated a strong correlation between the degree of angiogenesis induced by a tumour and the advancement of the tumour and systemic metastasis [68, 69]. Tumours with high levels of angiogenesis have been found to have a poorer prognosis and are associated with shorter overall survival rates [70]. Angiogenesis in NSCLC is regulated by the interaction of several growth factors, cytokines, proteolytic enzymes, adhesion molecules, and extracellular matrices [71]. One of the core driving factors of angiogenesis in NSCLC is VEGF which can influence cell survival pathways [8, 10, 13, 14]. During the angiogenic switch, the overstimulation of pro-angiogenic factors results in aberrant vasculature. This has a significant impact on the TME and affects several downstream pathways that ultimately result in modification to immune cells, mesenchymal-derived cells and vascular cells [11, 20, 57]. Notably, research has shown that some NSCLC types might also be non-angiogenic. For these types, tumour growth is sustained through a process known as vascular co-option [30]. Vascular co-option is the ability of some tumours to surround the vasculature and take over the pre-existing vessel of the pulmonary circulation [72, 73]. However, more research into vessel co-option in NSCLC needs to be conducted to understand how this process manifests [57]. The potential for NSCLC to stimulate angiogenesis or vessel co-option has added more difficulty in the development of *in vitro* modelling of NSCLC Moreover, angiogenesis in NSCLC is not fully understood, understanding the mechanisms and effects of angiogenesis on tumour progression of NSCLC and the TME is an essential step to developing novel and more effective treatments [19, 20]. Therefore, developing a novel 3D model designed to research NSCLC requires a comprehensive understanding of the mechanisms of tumour angiogenesis and the TME which influences it.

1.2.3. Mechanisms of angiogenesis in NSCLC

Understanding the processes of angiogenesis in the lung is particularly challenging due to the two circulatory systems supplying the lung with blood flow. Pulmonary circulation is a high-flow, low-pressure circulatory system that transports deoxygenated blood to the

lungs from the right ventricle of the heart which is the entire cardiac output. Bronchial circulation is part of the systemic circulation and this is subject to systemic arterial pressures, supplying the tissues of the lung with nutrients and oxygen [74, 75]. The angiogenic potential of these two circulatory systems are being further researched as some studies show that the bronchial circulation has a greater angiogenic potential and increased proliferation capacity. Furthermore, research has proven that pulmonary circulation has reduced angiogenic potential, however, there are suggestions that both circulatory systems play a role in tumour perfusion with tumour size and histology correlating to the circulatory system implicated in tumour perfusion [74, 75].

The endothelium is a membrane consisting mostly of ECs. In the lung, it is highly heterogenous with differences in surface receptors, proliferative capacity and bioenergetics of the ECs, specifically between the vasculature of the pulmonary and bronchial circulation [75]. Some studies have explored the differences between tumour angiogenesis in the two circulatory systems within the lungs [75]. A rat model of NSCLC was used to quantify bronchial and pulmonary circulatory alterations as the tumour grew and showed that the disruption of the bronchial circulation had the capacity to stop tumour growth as well as reduce tumour size. Whilst perfusion of the tumour by bronchial circulation increased as tumour size increased, the perfusion of the tumour by pulmonary circulation remained unchanged as tumour size increased further indicating the significance of bronchial circulation in NSCLC progression [75]. Targeting the ECs of the bronchial circulation is therefore a novel avenue of research that should be explored to improve therapies for NSCLC.

As ECs are the key targets for angiogenic factors such as VEGF-A, their surface marker expression and proliferative capacity holds a significant role in EC response to the angiogenic switch [74]. Once the angiogenic switch occurs, associated with NSCLC presentation, ECs accelerate glycolysis and increase glucose uptake allowing faster adenosine triphosphate (ATP) production and rendering more hypoxia-resistant ECs. Glycolytic differences between the endothelial subtypes result in varied responses to angiogenic factors and therefore, the angiogenic response stimulated by lung tumours is dependent on their location and proximity to arterial, arteriole and microvasculature [74]. Furthermore, EC response to angiogenic factors such as VEGF-A is affected by the expression of VEGF receptors on ECs [76]. Research has shown that VEGF-A exerts its pro-

angiogenic effects via VEGF receptor 2 (VEGF-R2) signalling, therefore the expression of VEGF-R2 on tumour-associated ECs is crucial for angiogenic activity, whilst VEGF receptor 1 (VEGF-R1), which has a higher affinity with VEGF-B, has a reduced effect on VEGFR-2-mediated angiogenesis [76, 77]. VEGF-R1 has been implicated to affect homeostasis and vascular development, its overexpression has been shown to inhibit the expression of VEGF-R2 and thus suppress VEGF-A-stimulated angiogenesis [77, 78]. Furthermore, hypoxia has been shown to affect the expression of VEGF receptors within the tumour microenvironment, with HIF-1α inducing the expression of VEGF-R2 [77, 78].

One likely reason for the lack of research conducted on the influence of the two circulatory systems in lung cancer may be due to limited lung cancer models that investigate lung vasculature and the sources of vasculature for lung tumours. Mouse models are inefficient at these types of investigations as mice lungs do not have a separate bronchial circulation and therefore cannot model the human lung circulatory sources for tumour vasculature accurately [75]. Human-specific models are therefore necessary to further understand how the two circulatory systems influence tumour angiogenesis in NSCLC. Whilst there has begun to explore the influence of the two circulatory systems, as described above, more relevant models that can effectively mimic the TME of NSCLC can help further progress the understanding of tumour angiogenesis in NSCLC [74, 75].

1.2.4. The role of fibroblast in the angiogenic process in NSCLC

The tumour microenvironment in lung adenocarcinomas is characterised by extensive cellular and mutational heterogeneity, which significantly influences tumour progression and angiogenesis. Fibroblasts are one of the key components of the TME in non-small cell lung cancer [9]. When recruited into the NSCLC TME, fibroblasts undergo reprogramming to become CAFs due to the hypoxic conditions within the TME, primarily mediated by HIF-1α. This transformation is crucial for tumour development, as CAFs contribute to multiple aspects of tumour progression, including the angiogenic process. Studies have shown that the activation of fibroblasts into CAFs under hypoxic conditions is largely dependent on HIF-1α. Experiments involving mouse embryonic fibroblasts with and without HIF-1α knockout have demonstrated that fibroblasts lacking HIF-1α do not exhibit the typical activation into CAFs under hypoxia and do not express CAF markers. This highlights the essential role of HIF-1α in fibroblast activation and their subsequent contributions to tumour angiogenesis [10].

Once activated, CAFs in the TME produce a variety of extracellular matrix proteins, growth factors, and cytokines, including collagen and fibronectin, which are crucial for creating a supportive ECM that aids in tumour progression. The ECM modified by CAFs not only provides structural support but also facilitates the binding of growth factors and cytokines, which are vital for angiogenesis [79]. For instance, fibronectin, a key ECM protein produced by CAFs, has been shown to play a significant role in angiogenesis by promoting the proliferation and migration of endothelial cells, which are essential steps in angiogenesis [80]. Furthermore, CAFs can promote angiogenesis through paracrine signalling mechanisms. One critical pathway involves the upregulation of VEGF in tumour cells. By enhancing VEGF expression, CAFs indirectly foster an environment conducive to angiogenesis, thereby facilitating tumour survival and expansion [12].

Through the transformation into CAFs, fibroblasts play a pivotal role in the angiogenic process in NSCLC. Their ability to modulate ECM composition, secrete angiogenic factors, and upregulate VEGF demonstrates their importance in promoting angiogenesis. Understanding the role of fibroblasts in the angiogenic process in NSCLC can provide insights into developing targeted therapies that disrupt these processes, potentially inhibiting tumour growth and spread [9]. Consequently, to develop a model that can effectively mimic the TME of NSCLC, it is important that the incorporation of CAFs is considered, not only for the production of the ECM but also for their influence in angiogenesis in NSCLC [50].

1.2.5. Project rationale

This project aims to address the feasibility of the use of homotypic and heterotypic 3D multicellular spheroid models as a basic step toward developing a more complex model capable of mimicking tumour angiogenesis in NSCLC. Given the distinct roles that the different components of the TME play in NSCLC angiogenesis, including ECs, CAFs, and the ECM, it is necessary to consider these elements when constructing an *in vitro* model. 3D multicellular spheroid models have emerged as a promising *in vitro* platform for studying the complex interactions between different cell types within the TME [81]. Therefore, spheroids comprised of NSCLC cells, ECs, and CAFs may serve as a suitable starting point for developing a more representative model of NSCLC angiogenesis. These spheroids should mimic the hypoxic conditions that are characteristic of the NSCLC TME and induce the activation of fibroblasts into CAFs, enabling the evaluation of their impact on

angiogenesis. Consequently, spheroid shape, size, and metabolic activity of spheroids generated using NSCLC cells, ECs and CAFs, are significant physical and functional characteristics that should be assessed to determine the suitability of using such spheroids for studying NSCLC angiogenesis. Producing and selecting spheroids that are predictable with a consistent phenotype is necessary for the development of a robust *in vitro* model of NSCLC angiogenesis. For example, to develop a microfluidic lab on a chip system that is robust and reliable to research the impact of shear stress on angiogenesis, it is essential for the spheroids used to be reproducible in addition to other components that are essential for the model [82-84]. Spheroids that exhibit heterogeneity in size, shape, and cellular composition may lead to inconsistencies in the evaluation of therapeutic interventions and angiogenic processes. The generation of consistent and reproducible 3D multicellular spheroids is essential for the development of a robust and reliable *in vitro* model that can effectively mimic the TME and facilitate the evaluation of therapeutic treatments and angiogenic processes [84].

Therefore, this project aims to investigate the feasibility of using homotypic and heterotypic 3D multicellular spheroids, produced using ultra-low adhesion (ULA) 96-well round bottom plates, as a building block for constructing a more complex *in vitro* model of NSCLC angiogenesis. This will involve establishing a systematic approach to evaluate and assess the physical and functional characteristics of the formed spheroids, such as size, shape, and metabolic activity, and implementing a preselection method to ensure the consistent production of spheroids. This will be done through the use of reliable imaging techniques and software with the capacity to evaluate spheroids that are acceptable to progress to subsequent research. This will provide a crucial first step towards the development of a robust and reliable *in vitro* model of NSCLC angiogenesis. The generation of consistent and reproducible 3D multicellular spheroids is essential for the development of a robust and reliable *in vitro* model that can effectively mimic the complex TME and facilitate the evaluation of therapeutic interventions and angiogenic processes in NSCLC.

1.3. Hypothesis and Aims

1.3.1. Hypothesis: Commercially available ultra-low attachment (ULA) multi-well plates can be used to produce 3D spheroids from a human NSCLC cell line that are consistent in shape (circularity) allowing for their incorporation into more complex models such as lung-on-a-chip that have been proven useful for investigating angiogenesis in NSCLC.

1.3.2. Project Aim: The aim of this study is to establish a preselection approach for the evaluation of in-house developed multicellular 3D spheroid models for NSCLC that can be used to produce reproducible and consistent spheroids. Additionally, to evaluate the feasibility of using these spheroids as *in vitro* models of the angiogenic switch in NSCLC for research in lung cancer treatment.

1.3.3. Objectives: The objectives of this study were dual:

1. To form heterotypic spheroids consisting of A549, MRC-5 and HUVEC cells in ULA plates
2. To assess the morphological characteristics of the 3D spheroids formed; and
3. To determine the ability of the 3D spheroids to express markers characteristic of the angiogenic switch (HIF-1α and VEGF-A) at various time points.

2. Materials and methods

In my project, I developed A549 or MRC-5 homotypic and heterotypic spheroids, which were then monitored over time. The workflow is presented in figure 2.1. Heterotypic spheroids were then optimised to establish a ratio of A549 to MRC-5 cells to produce spheroids with a consistent morphology. Additionally, a preselection method was established by assessing spheroid morphology using FIJI and MATLAB analysis to determine parameters that can be used to assess spheroid morphology consistency. Spheroid characterisation was then conducted to further assess viability, and the presence of CAF markers, EC markers and hypoxia markers.

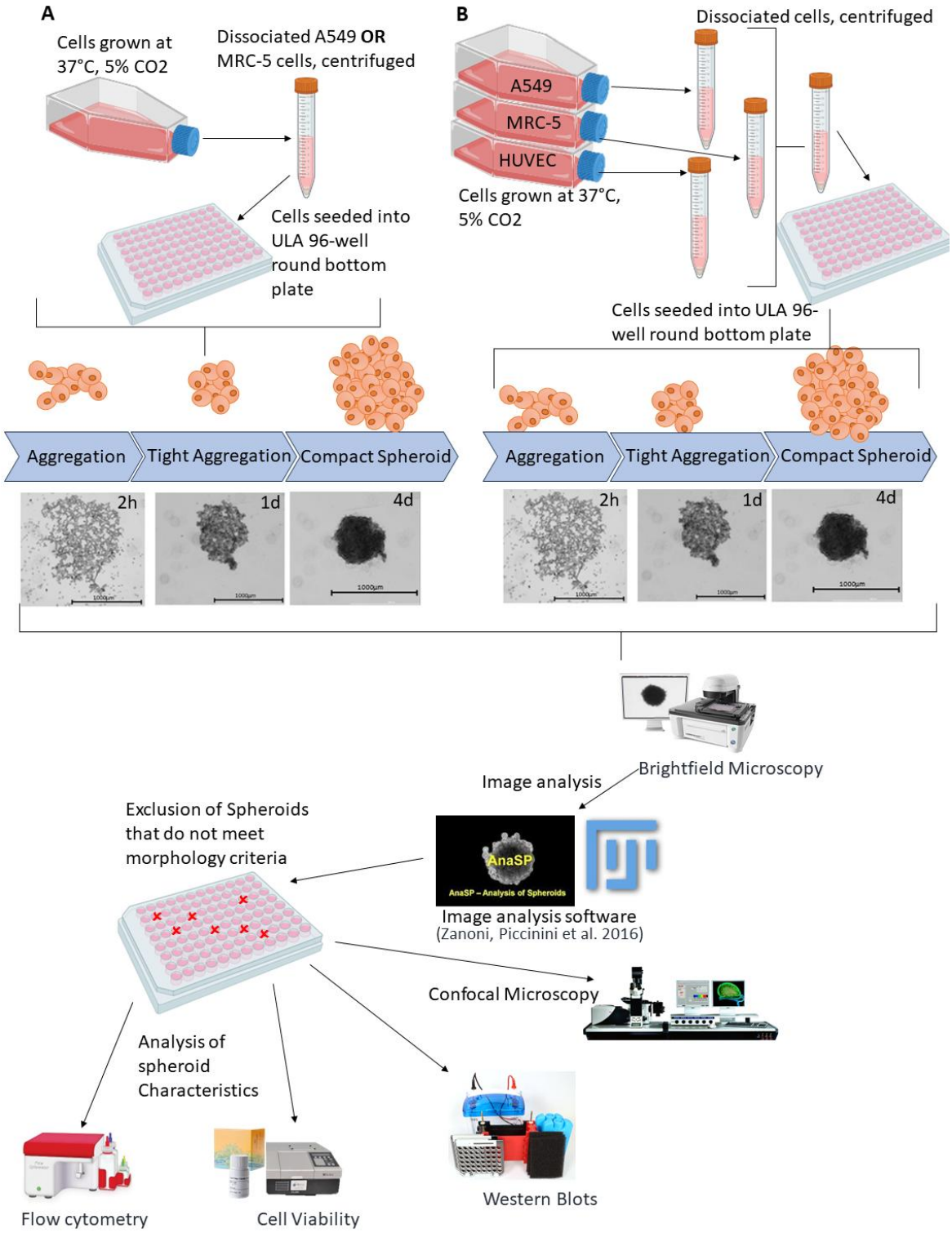

Figure 2.1: Workflow for the formation, selection and characterisation of A549 or MRC-5 homotypic spheroids (A) and heterotypic spheroids (B). 3D spheroids were formed using ULA 96-well round bottom plates. Spheroids were imaged using the Lionheart FX automated microscope and then analysed using image analysis software. Morphology analysis was used to preselect spheroids that were then assessed for proliferation using flow cytometry, and viability using CellTiter-Glo® 3D Cell Viability Assay. Functional endpoints included structure assessment using immunocytochemistry and confocal microscopy and angiogenesis potential using Western blot.

2.1. Cell culture, preparation, handling and cryopreservation.

2.1.1. Cell Lines

Human lung adenocarcinoma (A549) cell line was obtained from the American Tissue Culture Collection (ATCC, LGC Standards, Middlesex, UK) and was maintained in Dulbecco's Modified Eagle Growth Medium (DMEM) containing 4500 mg/L glucose, L-glutamine, and sodium bicarbonate, without sodium pyruvate, supplemented with 10% heat-inactivated foetal bovine serum (FBS) (Sigma-Aldrich, Ireland) and gentamicin (5 µg/mL) (Sigma-Aldrich, Ireland). Healthy human lung fibroblasts (MRC-5 cells) were obtained from the American Tissue Culture Collection (ATCC, LGC Standards, Middlesex, UK) and were maintained in Minimum Essential Med (MEM), low glucose with L-glutamine and no sodium pyruvate (Bio-Sciences Ltd, Ireland) supplemented with 10% FBS and 1% penicillin-streptomycin (Gibco, Invitrogen Ltd, VWR). Human umbilical vein ECs (HUVECs) were kindly supplied by Dr Anthony McElliot (Trinity College Dublin) and were maintained in endothelial cell media (ECM) (PromoCell, Ireland) supplemented with 10% foetal calf serum (PromoCell, Ireland) , growth factors (namely, 5 ng/mL Epidermal Growth Factor, 10 ng/mL Basic Fibroblast Growth Factor, 20 ng/mL Insulin-like Growth Factor (Long R3 IGF), 0.5 ng/mL Vascular Endothelial Growth Factor 165, 1 µg/mL Ascorbic Acid, 22.5 µg/mL Heparin, and 0.2 µg/mL Hydrocortisone.) (PromoCell, Ireland) and 1% penicillin-streptomycin. All cell lines were grown at 37 °C and 5% CO_2 in a humidified atmosphere in tissue culture flasks (Greiner Bio-One, Ireland) and were confirmed as mycoplasma negative.

2.1.2. Mycoplasma testing

In order to test cultures for mycoplasma contamination, Polymerase Chain Reaction (PCR) was conducted. Briefly, 1 mL of cell culture supernatant from a confluent cell culture flask was collected and centrifuged for 1 min at 644 xg to pellet any cell debris. PCR master mix was prepared on a volume per reaction basis. For each sample, the following reagents were added to form the master mix: DreamTaq Green Master Mix (Promega, M7122) (12.5µL), forward primer (0.5 µL), reverse primer (0.5 µL) and molecular biology grade water (11 µL). Master mix (24.5 µL) was then added to a PCR tube and 1 µL of sample was then added to the PCR tube. A positive control and negative control (molecular biology grade water.) sample was also prepared. The PCR tube was then placed in the thermocycler and the following program was selected: 1 cycle of Initialization (95 °C for 5 min); 40 cycles for denaturation (94 °C for 30 secs), annealing (55 °C for 30 s) and extension (72 °C for 1 min)

and 1 cycle for final extension (72 °C 10 for mins 1) and Hold at 4 °C. The PCR was then run on 2% (w/v) agarose gel (Sigma-Aldrich, A9539-250G) with 0.01% (v/v) SYBR Safe DNA gel stain (Thermofisher, S33102) in 1x Tris/Borate/EDTA (TBE) buffer. The DNA ladder was prepared, whilst the PCR gel set, using the following reagents: 2 µL DNA ladder, 1 µL loading Dye, and 3 µL water. The DNA ladder (6 µL) was pipetted into the first well of the gel, and PCR product (10 µL) was added into subsequent wells for each sample, including the positive and negative samples. The gel was electrophoresed at 100 V for 15 mins and then imaged on the chemiluminescent imaging system (Molecular Imager ChemiDoc XRS with ImageLab 3.0 Software, Bio-Rad). The expected product size for a positive sample is 270 bp.

2.1.3. Cell subculture

All cell culture work was conducted using aseptic techniques and carried out in a Faster BH-EN 2004 laminar air flow unit (Faster S.r.l, Italy). Briefly, this involved thoroughly cleaning the laminar flow hood with 1% Virkon (W/V) (SLS Scientific Laboratory Supplies Ireland) followed by 70% industrial methylated spirit (IMS). All reagents and equipment were sterilised using 70% IMS before entering the laminar flow hood. All cultures were subcultured once flasks were 70-85% confluent. Media from the culture flasks were discarded to waste and cells were washed with 5-10 mL sterile 1X phosphate buffered solution (PBS). PBS was prepared using PBS tablets (Fisher Scientific Ltd, 11435015). Cells were detached from flask substrates using TrypLE™ (Gibco, Ireland) for 5 min at 37 °C. Cells were checked for complete detachment using a light microscopy (Olympus, MA, USA). TrypLE was neutralised with complete growth media. The cell suspension was then resuspended in complete media at varying concentrations depending on experimental requirements.

2.1.4. Cryopreservation of cell lines

All cell lines were regularly frozen at -80 °C to keep passage numbers as low as possible. Briefly, confluent flasks were washed with PBS, cells were dissociated with TrypLE which was neutralised by complete growth media as previously described. Cell suspension was then collected in 15 mL sterile tubes and centrifuged for 3 min at 1450 xg. The supernatant was then discarded, and the cell pellet was resuspended in 1 mL complete growth media. 50 µL of dimethyl sulfoxide (DMSO) was then added to the cell suspension directly to a final concentration of 5%. Cells were then transferred to previously labelled cryovials (Sarstedt,

Germany). Cryovials were then placed into Mr Frosty freezing containers (Sigma-Aldrich, Ireland) for at least 48 h in a -80 °C freezer before being moved to labelled storage boxes and stored at -80 °C.

Cryopreserved cell suspensions were reconstituted by removal from the freezer with subsequent thawing. The cell suspensions were then added to previously labelled tissue culture flasks with 10-15 mL prewarmed complete growth media. Cells were then incubated at 37 °C and 5% CO_2 in a humidified atmosphere to allow attachment. After 24 h, media was removed, cells were washed with PBS and fresh media was added to the flask to remove residual DMSO.

2.1.5. Cell count using Trypan blue exclusion.

Cells were dissociated using TrypLE™ (Gibco, Ireland) for 5 min at 37 °C. Cells were checked for complete detachment using a light microscopy (Olympus, MA, USA). TrypLE was neutralised with complete growth media. Cell suspensions were then pelleted by centrifugation for 5 min at 1450 xg. Supernatants were discarded and cells were resuspended in 1 mL prewarmed complete media, ensuring that the cell suspension was mixed well. Using a pipette, 10 µL of the well-mixed cell suspension was added to an Eppendorf tube with 10 µL of Trypan blue solution and thoroughly resuspended (1:1 ratio). The trypan blue-cell solution was then loaded into the haemocytometer covered by a glass cover slip and allowed to settle briefly. The haemocytometer was then placed under the light microscope, and viable cells (cells that were white due to dye exclusion) were counted using the 4 large corners of the haemocytometer grid. Dead cells (cells that were dyed blue due to dye exclusion) were also counted. The total number of cells was calculated by the adding the number of viable and dead cells, allowing for the assessment of viability. A tally counter was used to ensure cell counts were accurate.

For seeding spheroids, only the number of viable cells was used. The average cell number of viable cells across the 4 grids was calculated (total number of viable cells / 4) and multiplied by 10,000 (10^4). This value was then multiplied by 2 to correct for the 1:1 dilution from adding trypan blue, yielding the total number of live cells per mL.

For viability assessment, cell counts of dissociated spheroids were used to calculate the percentage of viable cells. This was done by dividing the total live cell count by the total number of cells counted (this includes dead cells) and multiplying by 100. As shown by the formulas below:

$$Total\ number\ of\ cells = \ number\ of\ live\ cells + number\ of\ dead\ cells$$

$$Viability\ (\%) = \frac{number\ of\ live\ cells}{total\ number\ of\ cells} \times 100$$

The cell suspension can then be adjusted to the desired concentration of cells. The accuracy of initial cell counts was confirmed with flow cytometry, as described in section 2.4.1.

2.1.6. 3D spheroid formation using ULA plates.

For spheroid formation of A549, MRC-5, and heterotypic spheroids, cells were seeded into ultra-low attachment (ULA) CellStar® 96 well round bottom cell repellent plates (Gibco, Invitrogen Ltd, VWR). These plates have been shown to assist spheroid formation without the need for specific supplements or culture substrates, generating scaffold-free spheroids [85, 86].

A549 cells were seeded at varying densities (1000, 2500 and 5000 cells/well) to determine which cell density produced more consistently circular/spherical spheroids, in accordance with previously published research [87]. Briefly, cells were harvested as described in section 2.2. and a cell count was performed as described in section 2.2.1. Following the cell count, cell concentration was adjusted to 10^4, $5x10^4$ and 10^5 cells/mL. 100 µL of the cell suspension was then dispensed into each well of ULA 96 well round bottom plates. PBS was dispensed to the wells on the outer edge of the plate to reduce media evaporation and edge effect. The plate was then incubated at 37 °C and 5% CO_2 in a humidified atmosphere. After 2 hours, plates were imaged before adding an additional 100 µL of growth media. The growth media was changed every 2-4 days by aspirating the 200 µL of growth media from each well, followed by pipetting 200 µL back into the wells. This was done carefully so as not to remove the spheroid whilst removing media or dispensing media too harshly to keep the spheroids from being disrupted too much.

Heterotypic spheroids were formed using varying A549 to MRC-5 ratios. The number of A549 cells was kept constant at 5,000 cells/well. MRC-5 cell densities used were 10,000, 5,000, 2,500 and 2,000, cells/well (corresponding to a A549 to MRC-5 cell ratio of 1:2, 1:1, 2:1, and 5:2, respectively).

MRC-5 spheroids were grown as homotypic spheroids using densities comparable to those employed in heterotypic spheroids to enable comparisons in morphology, viability and cell numbers between the monocultures and the co-cultures.

2.1.6.1. Optimisation of cell culture media for co-cultures

The effect of different culture media was evaluated to select the optimal media for the co-culture of A549 and MRC-5 cell lines. A 96-well flat bottom plate was used with MRC-5 and A549 cells seeded separately. Both cell lines were grown in supplemented DMEM, MEM or a 50:50 mix thereof for 3 days. Viability was assessed using CellTiter-Glo® 3D Cell Viability Assay (Promega, MyBio, Ireland) as described in section 2.4.2. Valinomycin at a concentration of 120 µM per spheroid (IC50 for A549 cells) was used as a positive control [88-90]. Data was plotted into graphs using GraphPad Prism 10 using 3 spheroids per repeat.

2.2. Morphological assessment of Spheroids using Brightfield Microscopy

Spheroids were imaged using brightfield microscopy (Lionheart FX microscope (BioTek) equipped with Gen5 imaging software (BioTek)) at 2 h, 24 h, 4 d, 8 d, 12 d and 16 d after cell seeding, to monitor cell aggregation and spheroid morphology over time. Each well in the 96-well plates were imaged at a magnification of 4X. The software was programmed to capture images 600 ms after the automated stage moved to the next well to allow the spheroid to settle in the well before image capture. Images were then saved as tif files and analysed using FIJI and MATLAB as described below.

2.2.1. FIJI image analysis

The effects of cell density on the circularity of A549 and MRC-5 homotypic spheroids were assessed using FIJI and AnaSP software. This was done to determine seeding densities that would generate spheroids with consistent circularity and to establish the minimum acceptable circularity. Initially, circularity was used to compare 3 different cell densities of A549 and MRC-5 homotypic spheroids. Following circularity assessment of homotypic spheroids. I was able to determine that spheroids with a circularity of less than 0.8 showed more variability in viability. Thus, spheroids with a circularity of less than 0.8 were not used for further assays. This was therefore used as an exclusion criteria and spheroids with a circularity of less than 0.8 were deemed poor quality and were removed from future experimentation.

Briefly, this involved opening the tif image on FIJI and converting it to a 16-bit image. The threshold was then adjusted so that the spheroid was selected as a whole entity (figure 2.2).

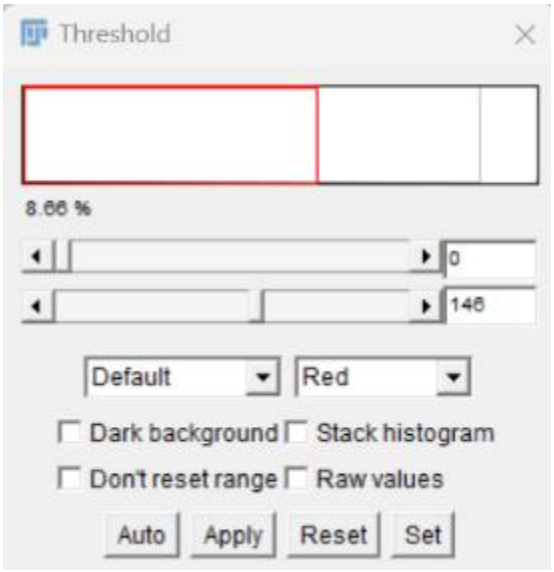

Figure 2.2: Visual representation of the Fiji settings used to adjust the threshold to encompass the spheroid as 1 particle.

Following the threshold adjustment, the image was converted to a black on white image and analysed using the analyse particle function of FIJI. Size was set to 200-infinity so that the spheroid gets analysed as a whole particle, circularity was set to 0.00 – 1.00 where 1 is a complete circle and 0 is a straight line (figure 2.3). Images of the mask and threshold adjusted images were saved as tif images and stored with the original images (figure 2.4). Measurements analysed included total area, average size, area, perimeter, circularity, solidity, Feret, Feret's X, Feret's Y, Feret angle and minimum Feret.

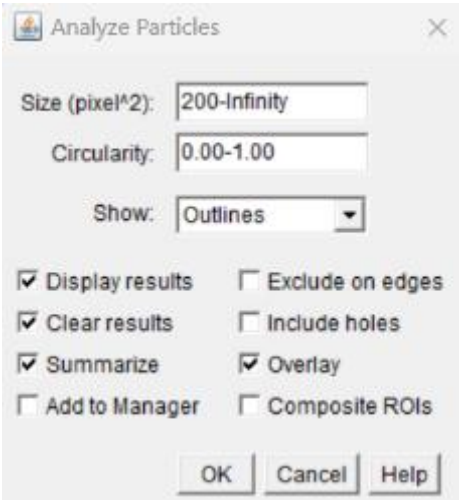

Figure 2.3: Visual representation of the FIJI settings used to measure and analyse the spheroid.

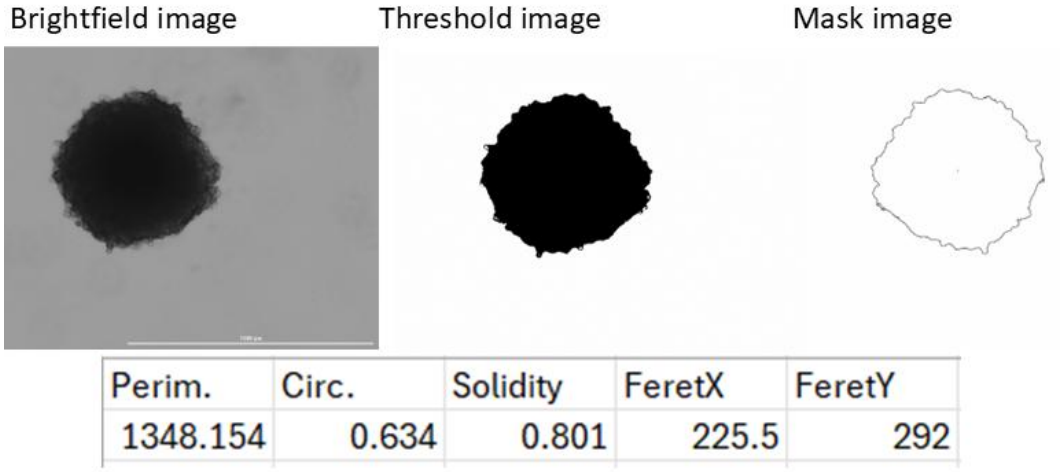

Perim.	Circ.	Solidity	FeretX	FeretY
1348.154	0.634	0.801	225.5	292

Figure 2.4: Representative images and measurements of the analysis process used in FIJI which shows the original brightfield image, the image produced after adjusting the threshold, the mask produced after analyse particle is conducted and the resultant measurements obtained. Measurements obtained are Perim. (Perimeter in µm), Circ. (Circularity), Solidity and FeretX and FeretY diameters (measured in µm).

2.2.2. MATLAB image analysis

Analysis of SPheroids (AnaSP), a software suite written in MATLAB (©, The MathWorks, Inc., Natick, MA, USA) and distributed as an open-source tool at http://sourceforge.net/p/anasp/, was used to further evaluate the parameters and morphology of spheroids. AnaSP is a software developed to analyse images of spheroids taken with entry-level brightfield microscopes with the aim of showing that spheroids with varying morphological parameters is a major source of variability in viability and response to treatments [15, 91]. The benefit of using AnaSP was that image analysis could be conducted in bulk, allowing for the rapid selection of spheroids that meet the selection

criteria (table 2.1). The selection criteria were circularity of 0.8 or more, solidity of 0.4 or more and a diameter of more than 400 µm. Furthermore, the ability to analyse images taken on entry-level brightfield microscopes makes the methodology transferrable to any microscope that can capture brightfield images. Spheroid morphological characteristics include circularity, solidity and diameter. Solidity is a measure of the smoothness of the spheroid where 1 is indicative of perfect smoothness and 0 indicates rough or ruffled edges. The spheroid diameter was calculated using the average between Feret's X and Feret's Y diameters of a spheroid.

This introduced an alternative approach to the selection of spheroids prior to treatments to improve the reproducibility of results.

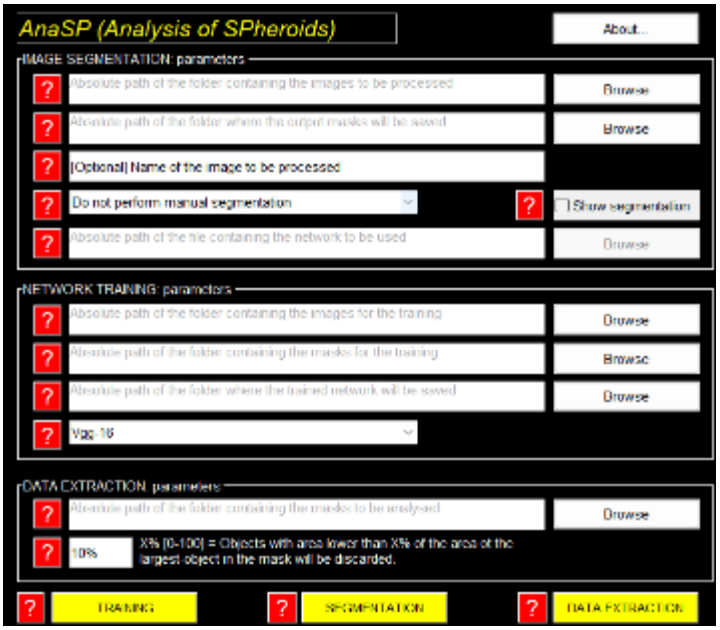

Figure 2.5: Visual representation of the AnaSP software interface used to analyse spheroids. The image shows the user interface of AnaSP, a user-friendly software developed to analyse images of spheroids in bulk. The image shows the network training potential of AnaSP that allows the software to be programmed for deep learning and better analysis of brightfield images.

Table 2.1: Exclusion and inclusion criteria used for preselecting spheroids.

	Circularity	Solidity	Diameter (µm)
Inclusion	>0.8	>0.4	>400
exclusion	<0.8	<0.4	<400

MATLAB was then used to generate multivariate graphs. The methodology used to generate the graphs can be found in Appendix I. Multivariate graphs were used to show the differences in Feret's x (z-axis) and Feret's Y diameter (x-axis) vs Time (y-axis) and

viability (colour map). Multivariate graphs were generated using MATLAB software (Appendix I).

2.3. Viability Assessment of Spheroids

2.3.1. Cell proliferation

Flow cytometry was used to assess cell proliferation. During cell seeding (t = 0 h), 1mL of the cell suspensions prepared for cell seeding in ULA plates was collected into an Eppendorf tube and centrifuged at 1450 xg for 1 min. The supernatant was removed, and cells were resuspended in 1 mL of pre-warmed PBS. To each Eppendorf, 5 µL of Hoechst 33342 (Thermo Fisher Scientific, Ireland) (5mg/mL stock) (dilution 1:200) and propidium iodide (PI) was added and then incubated at room temperature for 10 min protected from light. Eppendorf tubes were then centrifuged for 1 min at 1450 xg, supernatants were removed, and samples resuspended in 500 µL of 3.7% formaldehyde in PBS was added. The samples were then left to incubate at room temperature for 15 min. Samples were then centrifuged for 1 min at 1450 xg. The supernatant was aspirated and 1mL of PBS with 1% BSA was added before resuspending cells using a pipette and vortexed. Cells were then analysed by flow cytometry using excitation/emission of 350/461 nm on an Accuri Flow Cytometer (BD Accuri C6). The number of events per 100 µL was assessed setting a threshold of 20 000. Water and PBS with 1% BSA were used to gate out debris, and an unstained control was also used to assist with gating (figure 2.6). Samples with 1,000 events/100 µL were kept and used for seeding.

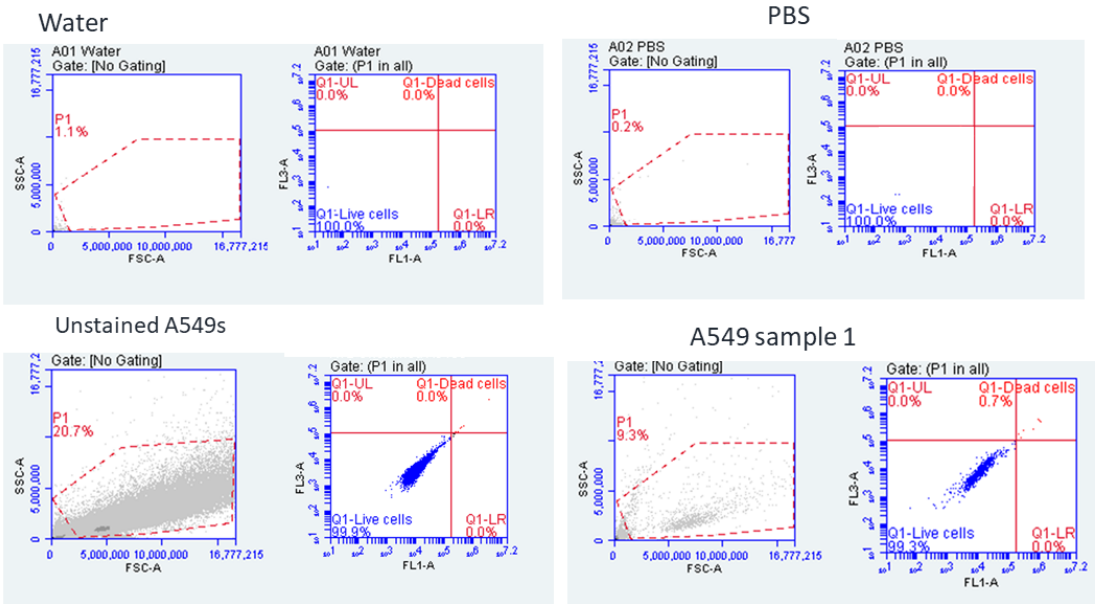

Figure 2.6: Example of the gating used for flow cytometry. Gating was done using water and PBS with 1% BSA to gate out debris.

2.3.2. Spheroid Dissociation

At 4, 8 and 12 d after cell seeding, spheroids were harvested from the ULA plates into Eppendorf tubes (1 spheroid/Eppendorf tube) using a pipette. Supernatants were discarded carefully with a pipette, ensuring spheroids were not lost in the process. 500 µL of prewarmed PBS was added to wash excess media off the spheroids. PBS was removed carefully using a pipette and 50 µL of 0.25% Trypsin-EDTA (Gibco) was added. Spheroids were then incubated for 10 min at 37 °C. Following incubation, 150 µL of media was added and spheroids mechanically dissociated in single cells by pipetting up and down several times. Dissociation of spheroids into single cells was confirmed using a haemocytometer (see Appendix III). The Eppendorf tubes were then centrifuged for 5 min at 200 xg. Supernatants were then discarded, and cells resuspended in 200 µL of pre-warmed PBS. 1 µL of Hoechst 33342 (5mg/mL stock) (dilution 1:200) was added to each Eppendorf. Samples were then incubated at room temperature for 10 min, protected from light. Following incubation, the samples were centrifuged for 1 min at 1450 xg, supernatant removed and 500 µL of 3.7% formaldehyde in PBS was added and incubated at room temperature for 15 min. Samples were then centrifuged for 1 min at 1450 xg, supernatant aspirated and sample resuspended in 1 mL of PBS with 1% BSA. Samples were then analysed by Accurri Flow Cytometer (BD Accuri C6) using excitation/emission of 350/461 nm (FL1 channel). For each sample, the events in 100 µL were measured. Gating was applied as shown in figure 2.6.

2.3.3. ATP quantification

The ATP content of spheroids was assessed at 4, 8 and 12 d after cell seeding using CellTiter-Glo® 3D Cell Viability Assay (Promega, MyBio, Ireland) as an indirect measurement of the cell culture viability. CellTiter Glo® is optimised for viability assessment through Adenosine triphosphate (ATP) quantification of spheroids up to 900 µm[92]. This involved harvesting spheroids at the relevant time point into Eppendorf tubes (1 sample/tube). Supernatants were discarded and spheroids washed with 100 µL of prewarmed PBS to remove any extracellular ATP. PBS was then removed and 100 µl of CellTiter-Glo® reagent was to each sample. Samples were incubated at room temperature on a plate shaker for 30 min. Following incubation, 50 µL was aspirated and added to opaque-walled 96-well plate (1 sample/well). The luminescence was then recorded using excitation/emission of 528/20 nm and an integration time of 0.5 second/well was used (gain = 135) on a Biotek FL x800 fluorescence and luminescence reader (Biotech, Ireland). The negative control used was 50

µL of growth media with 50 µL of CellTiter Glo®. Positive control used was 120 µM Valinomycin.

2.4. Phenotypic Assessment of Spheroids

2.4.1. Immunofluorescent Microscopy

Spheroids were harvested at 4, 8 and 12 d after cell seeding into Eppendorf tubes (1 spheroid/Eppendorf tube). Supernatants were discarded and spheroids washed with prewarmed PBS. PBS was then removed, and spheroids fixed using 200 µL of 3.7% formaldehyde for 15 min at room temperature. Formaldehyde was then removed carefully using a pipette, and spheroids washed 3 times with 200 µL of PBS. Cells were then permeabilised using 200 µL of 1% Triton X-100 in 1X PBS and incubated at room temperature for 15 min. Triton-X-100 was then removed, and the cells washed 3 times with 200 µL PBS. Spheroids were then incubated for 1 hr at room temperature with 200 µL of 2% BSA for blocking. Primary antibodies (table 2.2) were prepared in 0.1% BSA and 200 µL of staining solution was added to each spheroid and incubated for 3 h at room temperature.

Table 2.2: Primary antibodies used in immunofluorescent staining of spheroids

Antibody	Dilution	Secondary used
α-SMA	1:300	Alexa Fluor® 488
Ki-67	1:250	Already conjugated with FITC
CD31	1:300	Alexa Fluor® 488
HIF-1α	1:300	Alexa Fluor® 488

The staining solution was then removed, and spheroids were washed by adding 200 µL PBS using a pipette, followed by aspirating carefully with a pipette and repeated 3 times. Specimens were then incubated with fluorescently labelled secondary antibodies along with compatible counterstains (table 2.3) diluted in 0.1% BSA for 45 min at room temperature protected from light. Spheroids were then washed by adding 200 µL PBS using a pipette, followed by aspirating carefully with a pipette and repeated 3 times. Spheroids were then stored at 4 °C in PBS till imaging. To image using confocal microscopy, spheroids were removed from Eppendorf tubes using a 200 µL pipette and placed in an uncoated µ-slide well (Ibidi, Germany). Any excess PBS was removed and 50 µL Slowfade mounting

media was added to the well to prevent the spheroid from drying out and prevent bleaching. Quantitative Laser Scanning Confocal Microscopy (LSCM) imaging was performed using a Leica SP8 confocal microscope equipped with a 10x dry objective. Z-stack images were captured, and image processing was undertaken using LAS X software and FIJI.

Table 2.3: Counterstains used in immunofluorescent staining of spheroids

Stain	Dilution	target
Hoechst 33342	1:200	Nucleus
Rhodamine Phalloidin	1:40	Cytoskeleton

2.5. Western blotting

2.5.1. Preparation of cell lysates from 3D spheroids

Spheroids were harvested from ULA plates at 4, 8, 12 and 16 d after cell seeding into Eppendorf tubes (16 spheroids/Eppendorf tube). Supernatants were aspirated using a pipette and discarded. Spheroids were then washed by carefully pipetting 500 µL pre-warmed PBS into the Eppendorf tube; PBS was then carefully aspirated using a pipette ensuring no spheroids were removed. RIPA lysis buffer was then supplemented with 10 µL/mL Phenylmethyl Sulfonyl Fluoride (PMSF) solution (Sigma-Aldrich, Ireland), 10 µL/mL sodium orthovanadate solution (Sigma, Ireland) and 10 µL/mL protease inhibitor cocktail solution (Thermofisher, 1860932). From this point on cells were kept on ice. Supernatants were discarded and cells resuspended in 200 µL of supplemented RIPA buffer. Cells were kept on ice for 15 min before sonicated for 10 min in a sonic bath (Branson digital sonifier model 450). Following sonication cells were centrifuged for 15 min at 3260 xg at 4 °C. Cell lysates were then stored at -20°C till needed.

2.5.2. Quantification of Protein Content in spheroid cell lysates

Protein content in cell lysates was quantified using the Pierce™ BCA Protein Assay (Thermo Fisher Scientific Inc) as per the manufacturer's protocol. BCA Albumin Standard (Thermo Fisher Scientific Inc) was prepared by serial dilution (2000, 1000, 750, 500, 250, 125 and 25 µg/mL) in RIPA buffer. In a sterile 96-well plate, 200 µL/well of the BCA working reagent was added. Each standard/sample was vortexed before dispensing and 10µL/well of each standard/sample was added in duplicate, including a blank consisting of RIPA buffer. The plate was gently shaken, covered in foil, and placed in a 37 °C incubator for 30 min.

Absorbance was then measured at 562 nm on a BioTek Epoch Microplate Spectrophotometer plate reader. The blank absorbance was subtracted from all standard/sample absorbances, and all duplicated wells were averaged. A standard curve was plotted with the BSA concentration on the x-axis and absorbance at 562 nm on the y-axis. The protein concentration of samples was then extrapolated using the line equation generated by the standard curve.

2.5.3. Sample preparation

Samples were then prepared (30 µg per sample) for gel loading to undergo SDS-PAGE protein separation. Samples were prepared with RIPA buffer and normalised to 20 µL in Eppendorf tubes. A volume of 5 µL of NuPAGE™ lithium dodecyl sulfate (LDS) Sample Buffer (4X) (Thermofisher, NP0007) was then added to each sample before being heated to 70°C for 10 min on a heating block (Techne Dri-Block DB-3D, Sigma Aldrich, UK). Samples were then cooled to room temperature before gel loading.

2.5.4. SDS-PAGE gel electrophoresis

Following sample preparation with the loading buffer, the mini-PROTEAN Tetra Cell (Bio-Rad) was assembled. Once removed from the fridge, gels were placed into the module with the shorter plates facing inward towards the central buffer reservoir. The module was then fitted into the tank and 1X running buffer (10X stock: 30.2g Tri's base, 144g glycine, 100 mL 10% SDS and Dh_2O to make 1L) was poured between the two gel plates to the top of the module. The well combs were removed, and a 1 mL syringe was used to flush the wells with running buffer to ensure gel loading was not interrupted. The outer chamber was then filled with 600 mL of running buffer. The first well was loaded with 6 µL NeoPRO 10 Pre-stained Protein Ladder (Generon, NB-59-0002). A volume of 20 µL per sample was loaded to each well using gel loading tips. Gels were then electrophoresed (PowerPac Universal, Bio-Rad) for 30 min at 60 V then 1 h 30 min to 1h 50 min at 100 V to 120 V. Electrophoreses was stopped when the dye front was at the bottom or for larger gels when the dye front was run off the resolving gel. Glass plates were then carefully separated, and the wells cut off from the gel. The gel was then placed in a tray with 1X transfer buffer for approximately 5 min whilst equipment and reagents for transferring were prepared.

2.5.5. Protein transfer

Once proteins were separated by SDS-PAGE, a polyvinylidene fluoride (PVDF) 0.4 µM membrane was used to transfer proteins. Briefly, this required washing the gel in transfer

buffer 3 times for 5 min whilst the membrane was activated in methanol for 2 min then washed twice in transfer buffer. Sponges and filter paper were then soaked in transfer buffer before assembling the sandwich cassette as follows: 1 sponge 2 filter papers, the gel, the membrane 2 filter papers, and another sponge. A roller was used to remove bubbles before the sandwich cassette was placed in the transfer gasket with the black side of the sandwich cassette facing the back side of the transfer gasket. The gasket was then placed into the tank which was then filled with transfer buffer. A magnetic stirrer and ice pack were also placed in the tank to control temperature and circulate the transfer buffer. The tank was then placed on the magnetic stirrer and the transfer was started using a powerpack (PowerPac Universal, Bio-Rad) at 30V for 1 hr.

2.5.6. Blocking

Once the transfer was complete the cassette was removed and disassembled using plastic tweezers to minimise contact with the membrane. Filter paper and gel were discarded. Orientation of the membrane was noted by cutting the top left edge of the membrane, the side against the gel is the side with protein and therefore the top left corner will be the cut edge. (above the ladder). The membrane was then moved gently into a 50 mL falcon tube, ensuring the protein side was facing inward and the membrane edges didn't overlap. The membrane is first blocked by washing twice in TBST and then placed in blocking buffer (dependent on primary antibody used) which either be 5% Milk or 5% BSA in TBST for 1 hr on a roller (Stuart Analogue tube roller, Bibby Scientific) at 4°C.

2.5.7. Primary Antibody and secondary antibody

Following the blocking process, proteins were probed on the PVDF membrane with specific primary antibodies (table 2.4). The blocking buffer was removed and primary antibody in its dilution buffer (either 5% Milk or 5% BSA in TBST depending on the antibody) at 4°C on a roller overnight. The membrane was then washed twice in TBST before incubating at room temperature for 1 hr on a roller with the secondary antibody in the blocking buffer used.

2.5.8. Detection

Imaging of the membranes was completed through a chemiluminescent imaging system (Molecular Imager ChemiDoc XRS with ImageLab 3.0 Software, Bio-Rad). Membranes were placed on clean acetate sheets. The Clarity Western ECL Substrate (Bio-Rad) reagents (1:1) were combined to make the chemiluminescent substrate which was then poured onto the

membranes ensuring the entire surface was covered and allowed to develop for 2 min. The membrane was then placed in the imaging system to be imaged. If re-probing was needed without stripping, the membrane was washed twice with TBST following imaging and then re-probed with the primary antibody as previously described.

Table 2.4: Primary antibodies used for protein quantification

Anti-body	host	dilution	Secondary	Catalogue number	Supplier	Blocking buffer
B-actin	Rabbit	1:500	Anti-rabbit HRP	4970	Cell Signaling Technology, Inc.	5% BSA
VEGF-A	Rabbit	1:500	Anti-rabbit HRP	50661S	Cell Signalling Technology, Inc.	5% Milk
HIF-1α	mouse	1:1000	Anti-mouse HRP	PA1-16601	Thermo Fisher Scientific Inc.	5% Milk

2.6. Statistical Analysis

All conditions were tested in triplicate ($n_{replicates}$ = 3), and three independent experiments were carried out (n_{tests} = 3) unless otherwise stated. Data are presented as average ± standard error of the mean. All graphs and statistical analysis were performed using GraphPad Prism 10 (Dotmatics, UK). The statistical test carried out for each dataset is specified in the figure captions. $p < 0.05$ was considered statistically significant. Statistical tests carried out include two-way ANOVAs like Tukey's multiple comparisons test and Šídák's multiple comparisons.

3. Results

The first aim of this project was to establish the spheroid formation protocol for heterotypic spheroids composed of A549 and MRC-5 cells with the goal of achieving reproducible spherical aggregates. Spheroid morphological parameters such as circularity can be used as a quantifiable parameter to measure the consistency of spheroids [15]. Factors that impact spheroid morphology and viability [93] and that were assessed in this project, included media composition, cell seeding density, culture time and the cell seeding ratio of A549 to MRC-5 cells.

3.1. Co-culture optimisation

3.1.1. Optimisation of cell media for co-cultures

The effects of DMEM and MEM culture media on the viability of A549 and MRC-5 homotypic spheroids were assessed using the CellTiter-Glo® luminescent cell viability assay (figure 3.1). This was done to ensure that the combination of growth media when seeding heterotypic spheroids had no effect on cell viability. The results show that there is no statistically significant difference between the different media types. However, a statistically significant difference was observed between the media type and the positive controls used (100 µM Tacrine, 120 µM Valinomycin and 10x lysis buffer).

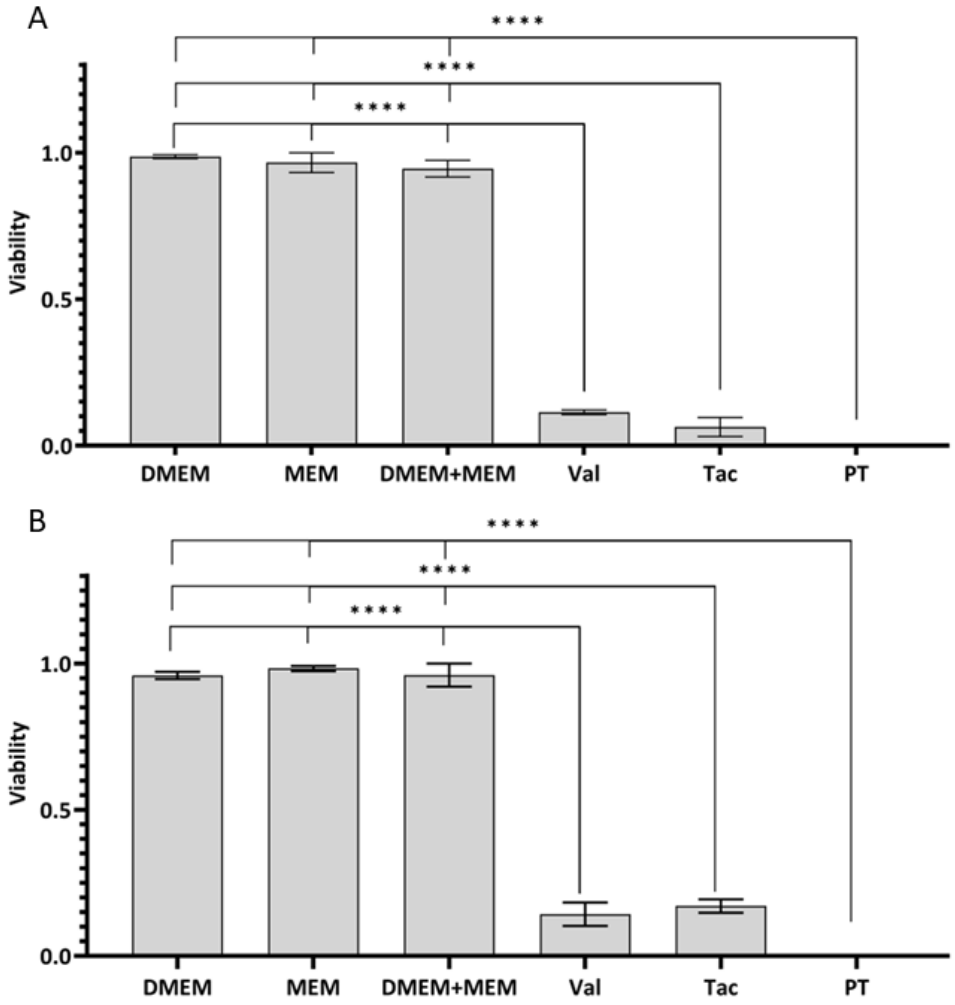

Figure 3.1: Viability of A549 cells (A) and MRC-5 cells (B). Relative luminescence was normalised to the negative control (Cells grown in DMEM for A549 cells and cells grown in MEM for MRC-5 cells). Valinomycin (Val), Tacrine (Tac) and lysis buffer (PT) were used as a positive control. Standard error of the mean was indicated with bars above each column and statistical significance compared to Valinomycin (where $P<0.001$). n=3, Statistical significance was determined using two-way ANOVA.

3.2. Spheroid Morphology

Morphology parameters such as circularity were used to develop the preselection protocol of spheroids that will be used in the following assays. Circularity was therefore a key morphological parameter assessed. Brightfield images captured using the Lionheart Fx microscope were assessed to generate circularity, solidity and diameter measurements in order to ensure spheroids used were consistent in size and shape.

3.2.1. Brightfield images of spheroids captured using the Lionheart Fx microscope.

FIJI and AnaSP were used to generate quantitative data from brightfield images of spheroids taken at multiple time points. As AnaSP is a software that has recently been developed, both FIJI and AnaSP were used to generate quantitative data. Initial spheroids

seeded with 1000 A549 cells produced spheroids that were extremely heterogeneous and inconsistent in shape (figure 3.2). As a result, viability of the spheroids was variable (as seen in section 3.5, figure 3.17). Research indicated that an increase in cell number could produce spheroids with more consistent morphology [15]. To establish what seeding density to use for future experiments, spheroids with cell densities of 1000, 2500 and 5000 cells were seeded, and their morphology and viability were compared.

Images show that A549 homotypic spheroids with initial cell densities of 1000 cells/spheroid exhibit irregular and inconsistent morphology with protruding sections of cells (figure 3.2). Whilst MRC-5 homotypic spheroids using initial cell densities of 1000 cells/spheroid exhibited relatively compact and circular spheroids (figure 3.3). Alternatively, spheroids of A549 cells with initial cell densities of 2500 and 5000 cells/spheroid exhibited more consistent and circular morphology with fewer protrusions and more uniform shape (as seen in section 3.2.2, figure 3.7). Moreover, spheroids of A549 cells with initial cell densities of 5000 cells/spheroid exhibited the most consistent and circular morphology. Spheroids of MRC-5 cells with initial cell densities of 2500 and 5000 cells/spheroid exhibited similar morphology to A549 spheroids with fewer protrusions and a more uniform shape (figure 3.4). Consequently, all subsequent spheroids generated with A549 cells had an initial cell density of 5000 cells/spheroid. Heterotypic spheroids were then developed with varying ratios of A549: MRC-5 cells to evaluate their morphology (figures 3.5). Images of the heterotypic spheroids show that co-cultured cells aggregate faster than the A549 homotypic spheroids. Whilst morphological assessment of heterotypic spheroids indicated that the 5:2 ratio produced the most homogenous and circular shaped spheroids (figure 3.5), cell viability (section 3.3) indicated that cell viability of the 1:1 ratio was more consistent and yielded more viable spheroids than a ratio of 5:2. Therefore, heterotypic spheroids composed of A549, MRC-5 and HUVEC cells were grown at a ratio of 1:1:1. Homotypic spheroids of HUVEC cells with initial seeding densities of 5000 cells/well were seeded to determine if HUVEC cells would form spheroids (figure 3.6B). Images indicated that HUVEC cells for compact spheroids are similar to those composed of MRC-5 cells. However, at day 12 and 16, cell debris was observed, indicating viability of HUVECs in spheroids may be affected over time. Images of heterotypic spheroids composed of A549, MRC-5 and HUVEC cells (figure 3.6C) showed that cells aggregated faster than A549 homotypic spheroids but slower than A549-MRC-5 heterotypic spheroids.

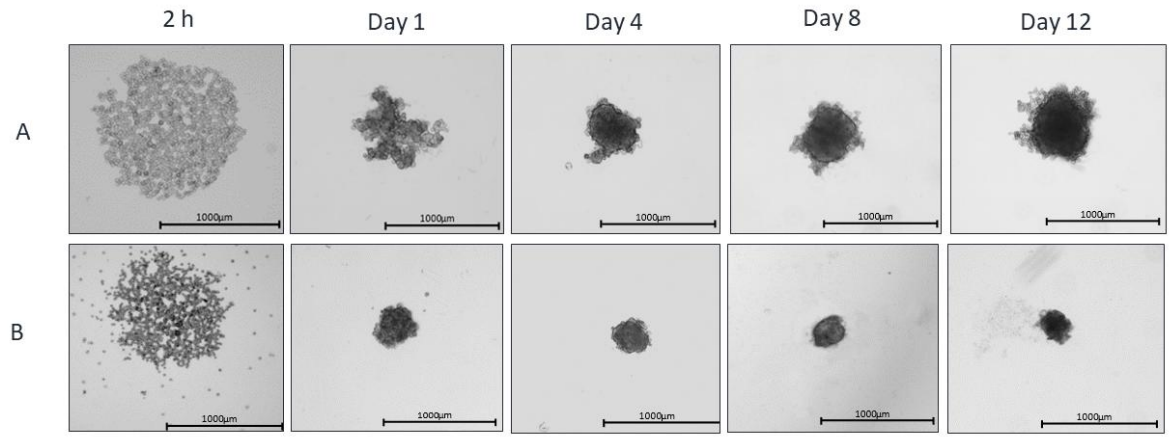

Figure 3.2: Representative images captured on the lionheart FX Microscope at 2h, 24 h, 4 days 8 days, and 12 days of A549 (A) and MRC-5 (B) spheroids (1000 cells/spheroid) at a magnification of 4X, Scale bar = 1000 µm.

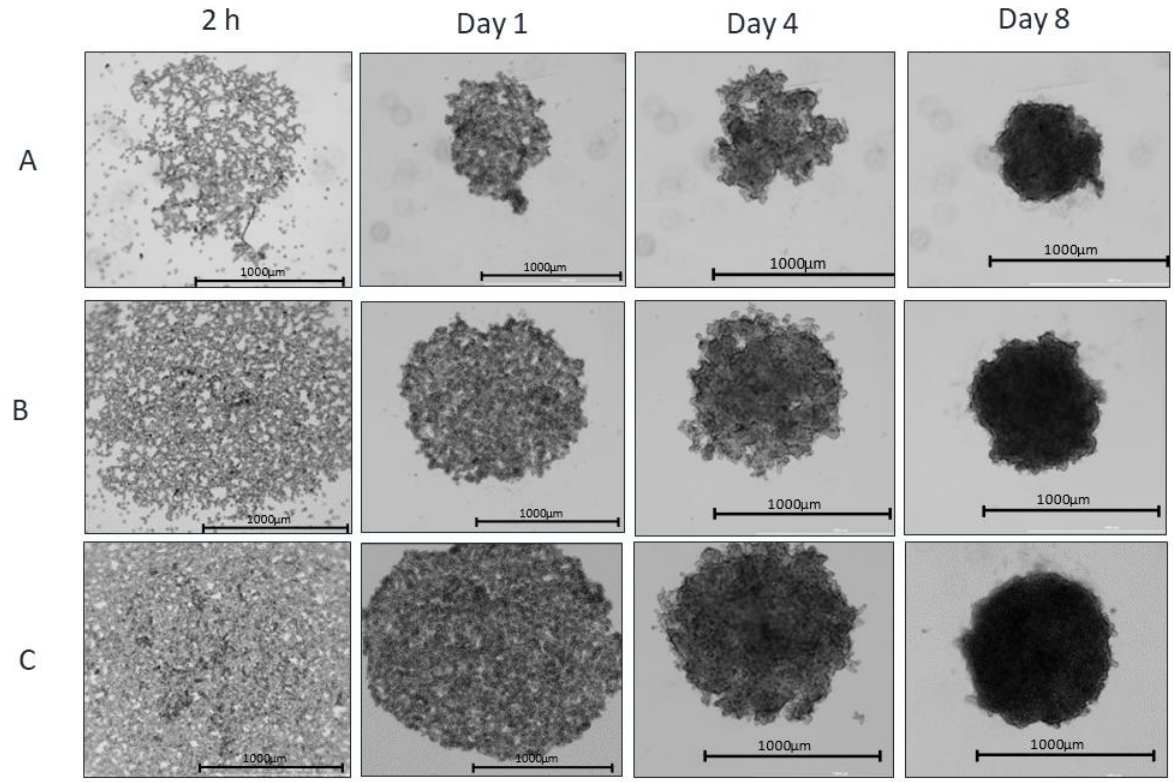

Figure 3.3: Brightfield images of A549 spheroids with 1000 cells/well (A) 5000 cells/well(B) and 10 000 cells/well (C) taken at various time points using the Lionheart FX Automated Microscope at a magnification of 4X, Scale bar = 1000 µm

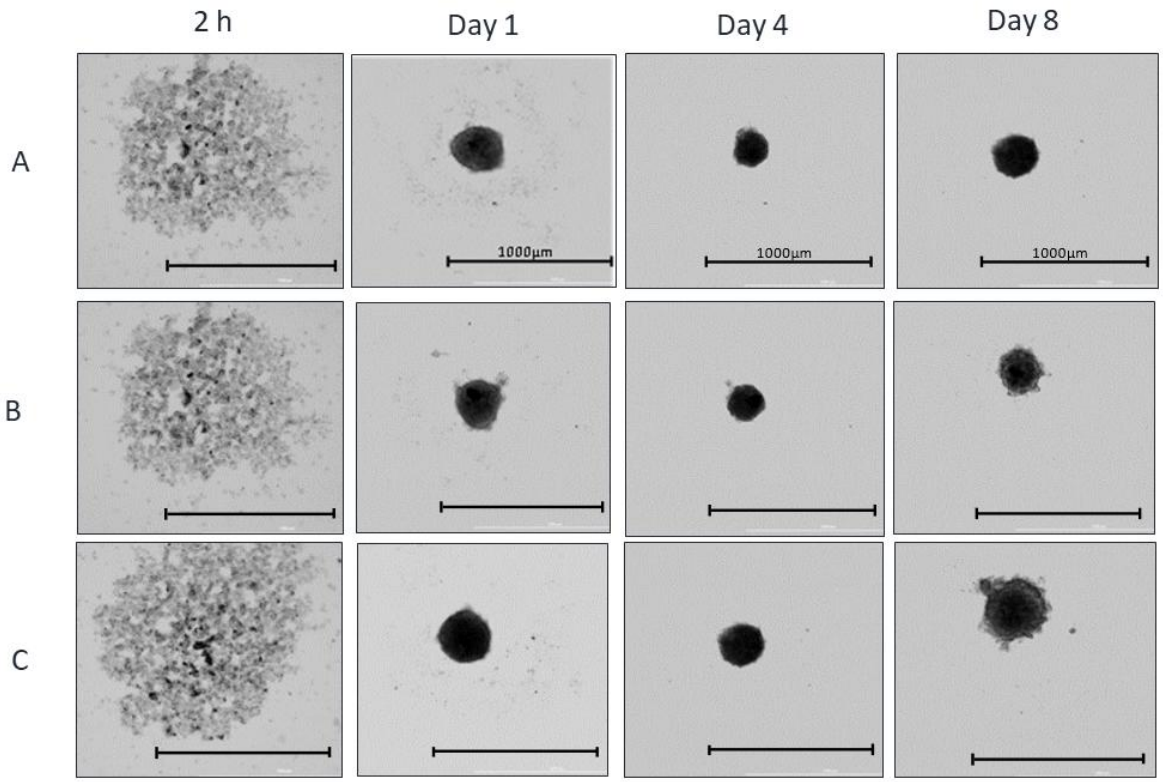

Figure 3.4: Brightfield images of MRC-5 spheroids with 1000 cells/well (A) 5000 cells/well(B) and 10 000 cells/well (C) taken at various time points using the Lionheart FX Automated Microscope at a magnification of 4X, Scale bar = 1000 µm.

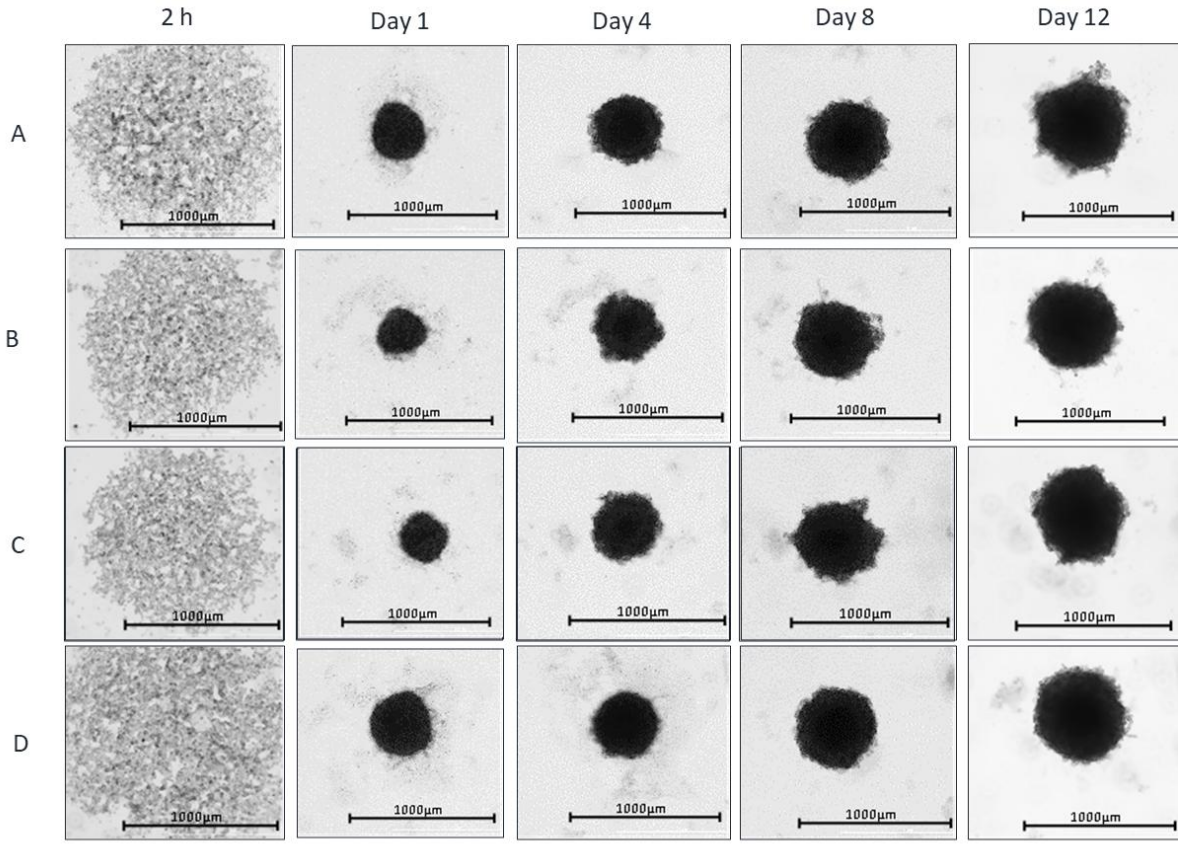

Figure 3.5: Brightfield images of A549-MRC-5 heterotypic spheroids with a ratio of 1:1 (A), 2:1 (B), 5:2 (C), and 1:2 (D) taken at various time points using the Lionheart FX Automated Microscope at a magnification of 4X, Scale bar = 1000 µm.

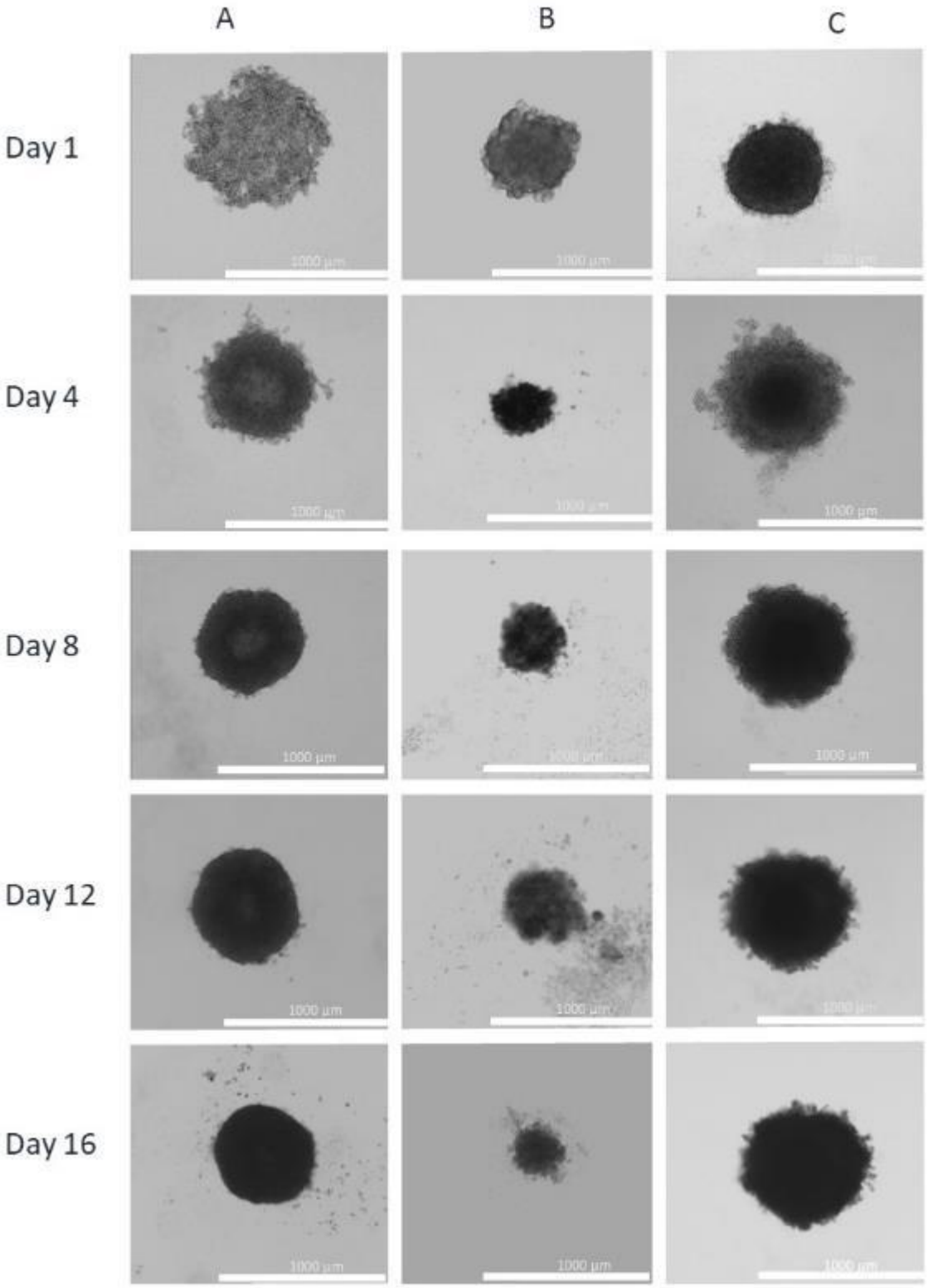

Figure 3.6: Brightfield images of A549 spheroids (A), HUVEC spheroids (B) and Heterotypic spheroids composed of A549, MRC-5, and HUVECs (C) taken at various time points using the Lionheart FX Automated Microscope at a magnification of 4X, Scale bar = 1000 µm.

3.2.2. Spheroid Morphology Characteristics

An initial assessment of spheroid circularity in A549 and MRC-5 homotypic spheroids showed that A549 spheroids exhibit higher circularity (0.74 to 0.978) than MRC-5 spheroids (0.71 to 0.88) (figure 3.7A and 3.7B). Circularity increased over time in both cell types, with the highest circularity observed at a seeding density of 5000 cells/well. However, both A549 and MRC-5 spheroids exhibited decreased circularity at day 8, suggesting a loss of circularity during the growth phase. For heterotypic spheroids, different A549 cell ratios were evaluated. A 5:2 ratio yielded the highest mean circularity (0.83) on day 8, but a 1:1 ratio showed the least variability across all parameters. Circularity, solidity, and diameter measurements for these spheroids, plotted in multivariate graphs (figure 3.8A and 3.8B), demonstrated that A549 spheroids show more variability and lower solidity than MRC-5 spheroids, which are more compact but have lower circularity. Furthermore, the circularity solidity and diameter measurements of A549-MRC-5 heterotypic spheroids with varying ratios (figure 3.9) revealed that circularity and solidity was highest in all ratios at day 8. Subsequent tri-cultured heterotypic spheroids (A549, MRC-5, and HUVEC cells) with a 1:1:1 ratio displayed consistent circularity over time, with the highest mean circularity of 0.87 at day 16 (figure 3.10). In addition, the circularity, Solidity and Diameter measurements of A549-MRC-5-HUVEC heterotypic spheroids revealed that the solidity increases over time whilst circularity remained consistent overtime (figure 3.11).

Table 3.1: Summary of Spheroid Types and Circularity

Spheroid Type	Cell Ratio	Circularity Range	Time Point for Maximum Circularity	Notes
A549 Homotypic	N/A	0.74 to 0.978	Day 4 (>0.9 circularity)	Higher circularity than MRC-5, variability observed at days 4, 8, and 12.
MRC-5 Homotypic	N/A	0.71 to 0.88	Day 4 (>0.85 circularity)	Lower circularity than A549, does not reach >0.9, peaks at 0.88.
A549: MRC-5 Heterotypic	5:2	Up to 0.83	Day 8	Highest circularity among ratios tested, with variability increasing by day 12.
A549: MRC-5 Heterotypic	1:1	Consistent over time	N/A	Least variation across all parameters, recommended for future studies.
Tri-cultured Heterotypic	1:1:1	Up to 0.87	Day 16	Includes A549, MRC-5, and HUVEC cells, more consistent circularity over extended time points.

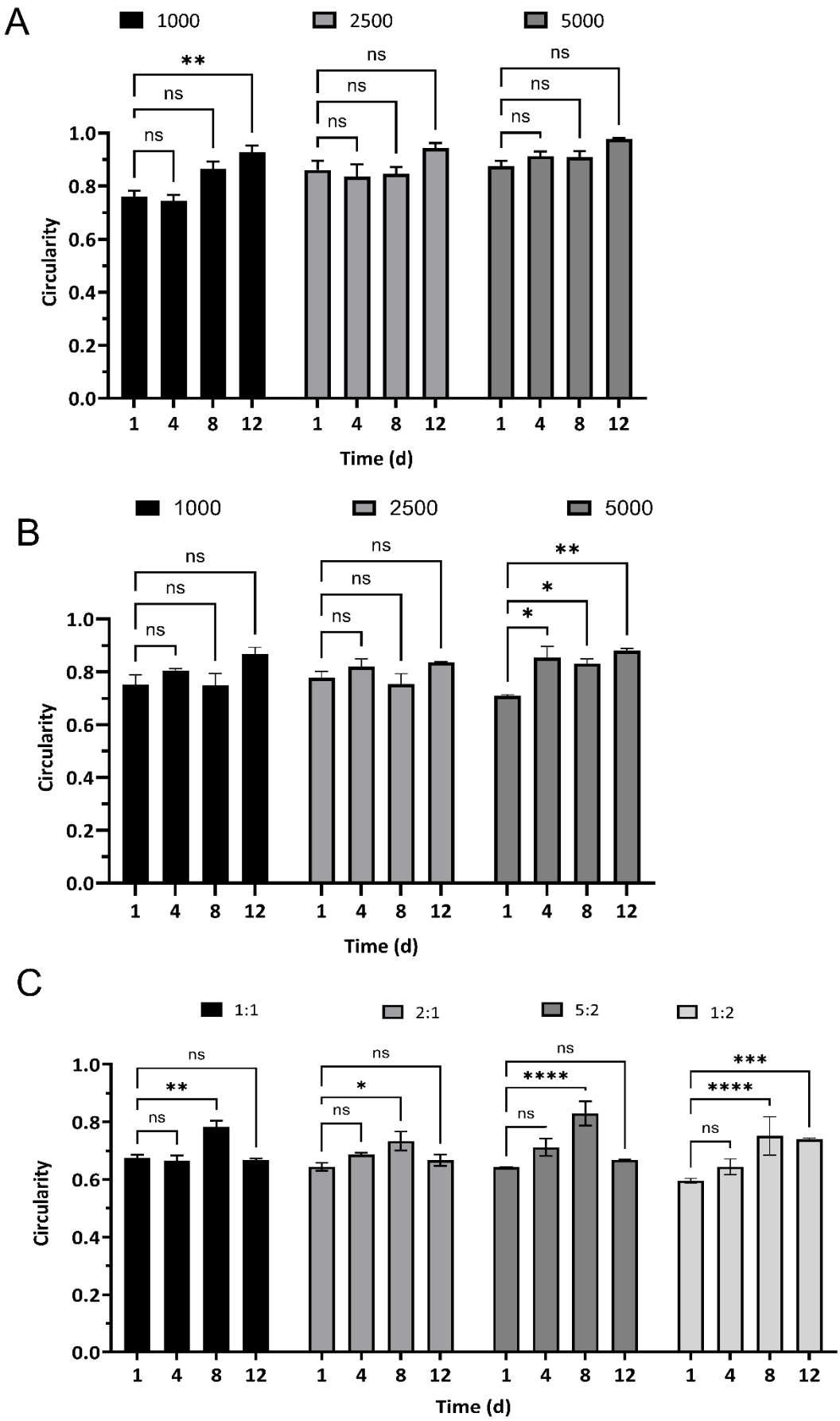

Figure 3.7: Graphs displaying the circularity of different seeding densities of A549 (A) and MRC-5 (B) spheroids and different ratios of A549:MRC-5 (C) spheroids measured after 1, 4,

8, and 12 days of growth using AnaSP software. Data used to generate these results were from 3 independent 96-well plates with 12 spheroids per plate for each seeding density. Data are represented as mean ± SEM ($n_{replicates}$= 36). Statistical significance is indicated with * (p <0.05) **(p <0.01), ***(p <0.001) and ****(p <0.0001) , when statistical significance was not obtained (P >0.05) it has been indicated with ns. Statistical significance was generated using the two-way ANOVA and Tukey's multiple comparisons test in graph pad prism 10.

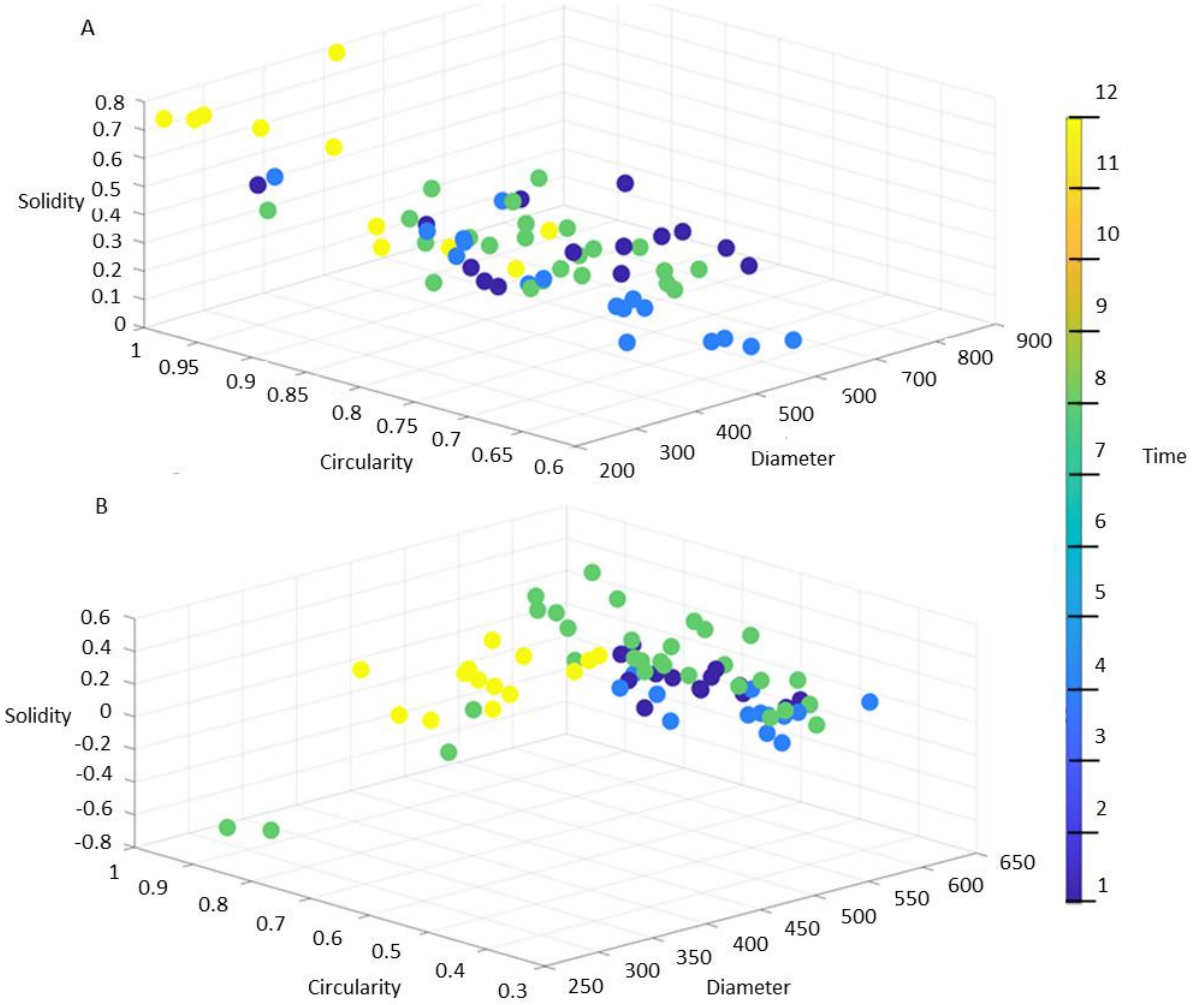

Figure 3.8: 3D morphology graphs displaying the circularity, Solidity and Diameter measurements of homotypic A549 (A) and MRC-5 (B) spheroids (5000 cells/spheroid). The colour bar indicates growth time in days. Data used to generate these results were from 3 independent 96-well plates with 12 spheroids per plate for each seeding density. Data are represented as mean ± SEM ($n_{replicates}$= 36).

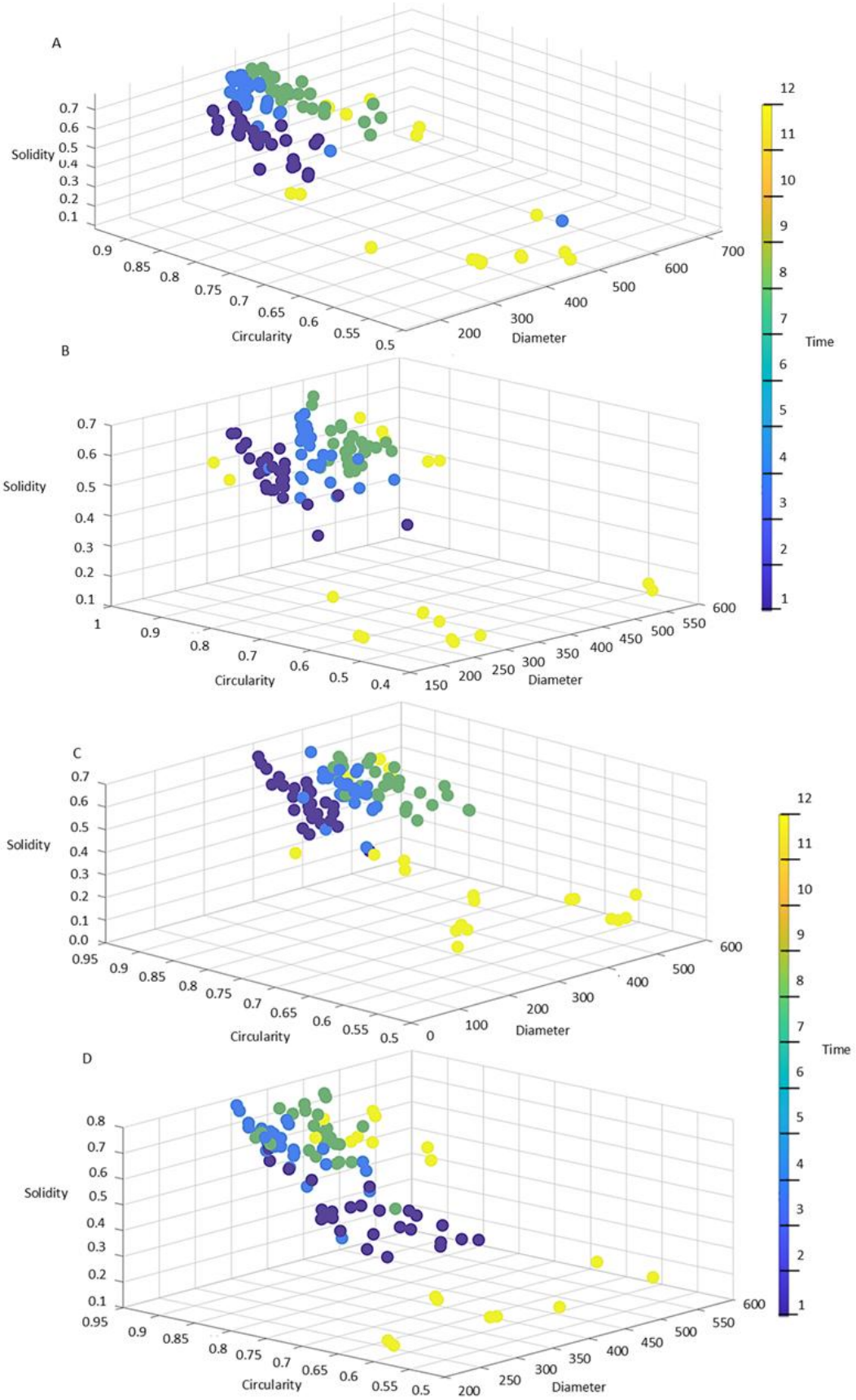

Figure 3.9: 3D morphology graphs displaying the circularity, Solidity and Diameter measurements of A549-MRC-5 heterotypic spheroids with a ratio of 1:1 (A) 2:1 (B) 5:2 (C) and 1:2 (D). The colour bar indicates growth time in days. Data used to generate these results were from 3 independent 96-well plates with 12 spheroids per plate for each seeding density. Data are represented as mean ± SEM ($n_{replicates}$= 36).

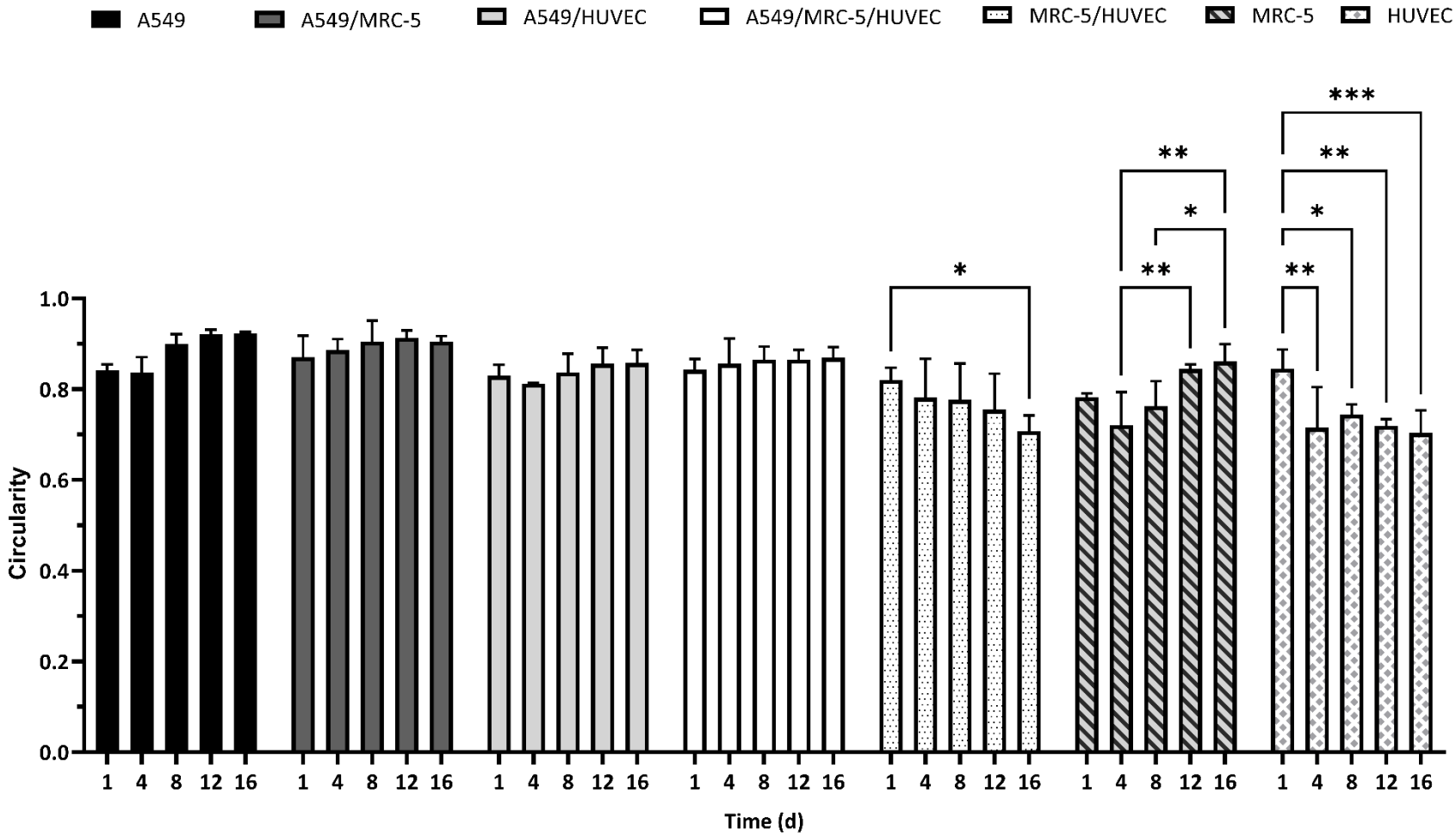

Figure 3.10: Graph displaying the circularity of homotypic and heterotypic spheroids. Each cell line was seeded at a density of 5,000 cells per well, with a 1:1:1 ratio for all heterotypic spheroids. Data used to generate these results were from 3 independent 96-well plates with 12 spheroids per plate for each seeding density. Data are represented as mean ± SEM ($n_{replicates}$= 36). Statistical significance is indicated with * (p <0.05) **(p <0.01) and ***(p <0.001) , when statistical significance was not obtained (P >0.05) it has been indicated with ns. Statistical significance was generated using the two-way ANOVA and Tukey's multiple comparisons test in graph pad prism 10.

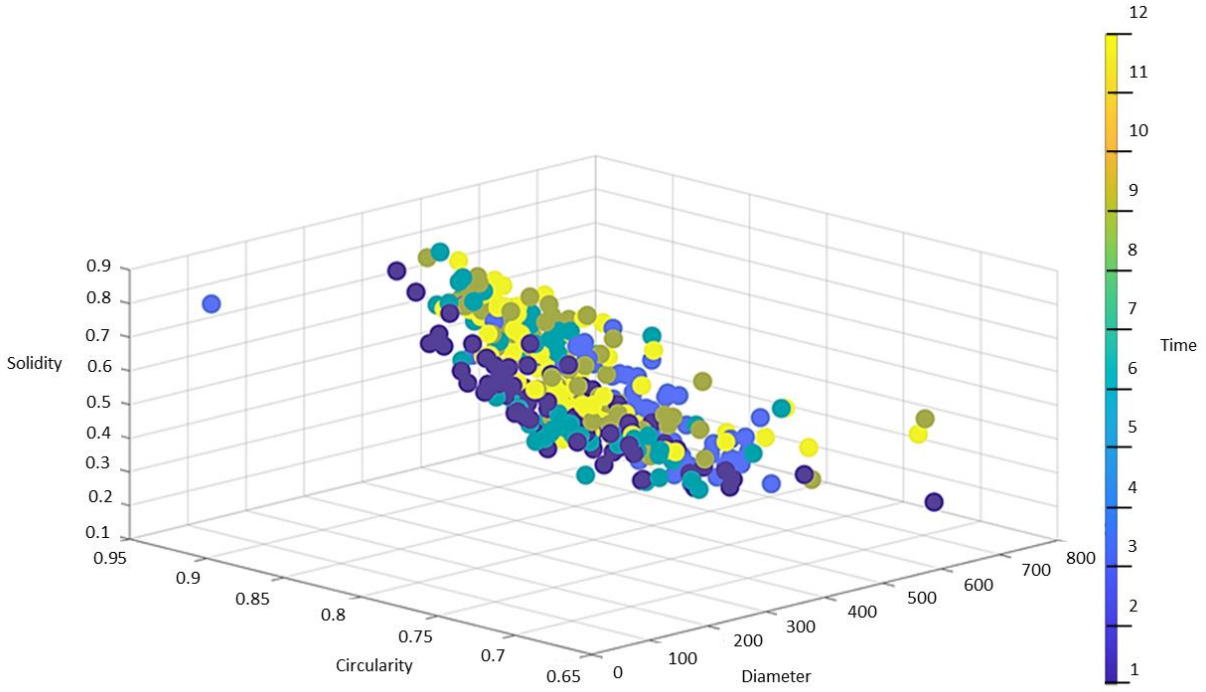

Figure 3.11: 3D morphology graphs displaying the circularity, Solidity and Diameter measurements of A549-MRC-5-HUVEC heterotypic spheroids. The colour bar indicates growth time in days. Data used to generate these results were from 3 independent 96-well plates with 20 spheroids per plate for each seeding density. Data are represented as mean ± SEM ($n_{replicates}$= 36).

3.3. Cell Number Quantification and Viability Using Flow Cytometry

Flow cytometry analysis was used to quantify the proliferation of cells in homotypic and heterotypic spheroids to confirm that spheroids enter the cell growth phase at day 4. Additionally, propidium iodide(PI) staining was used to quantify the number of dead cells within the spheroids.

The results confirm that initial seeding densities used to seed homotypic spheroids for both A549 cells and MRC-5 fibroblasts were approximately 5000 cells in 200 µL (figure 3.12). This demonstrated the accuracy of the cell-seeding technique used. Furthermore, results revealed that A549 spheroids exhibited an increase in cell number after 4 days of growth (figure 3.12A). However, cell numbers did not increase exponentially in accordance with the known doubling time of A549 cells. Furthermore, flow cytometry analysis of MRC-5 spheroids revealed that cell numbers only increase slightly after 4 days of growth (figure 3.12 B). MRC-5 cells have a slower doubling time than A549 cells so the reduced increase in cell number is in line with the MRC-5 cell line characteristics. In addition, PI staining indicated the viability of spheroids as cells stained with PI are deemed dead. For both A549

and MRC-5 cells, the percentage of cells stained with PI was less than 5% with the highest mean percentage of 4.56% of dead cells observed in 4 day old A549 homotypic spheroids (figure 3.13). In addition, the mean percentage of viable cells in A549-MRC-5 heterotypic spheroids grown for 4 days was lower in comparison to both A549 and MRC-5 homotypic spheroids. The mean percentage of viable cells was 80% in the heterotypic spheroids whilst the mean percentage of viable cells in the A549 and MRC-5 homotypic spheroids was 95.6% and 96.8%, respectively (figure 3.14). Furthermore, the comparison of A549, MRC-5 and A594-MRC-5 heterotypic spheroids grown for 4 days show that cell numbers in the heterotypic spheroids were higher than in the homotypic spheroids as expected (figure 3.15). To further validate the results described above, an additional viability assay was carried out by Trypan Blue exclusion assay (section 3.4) and by ATP quantification using CellTiter-Glo® (section 3.5)

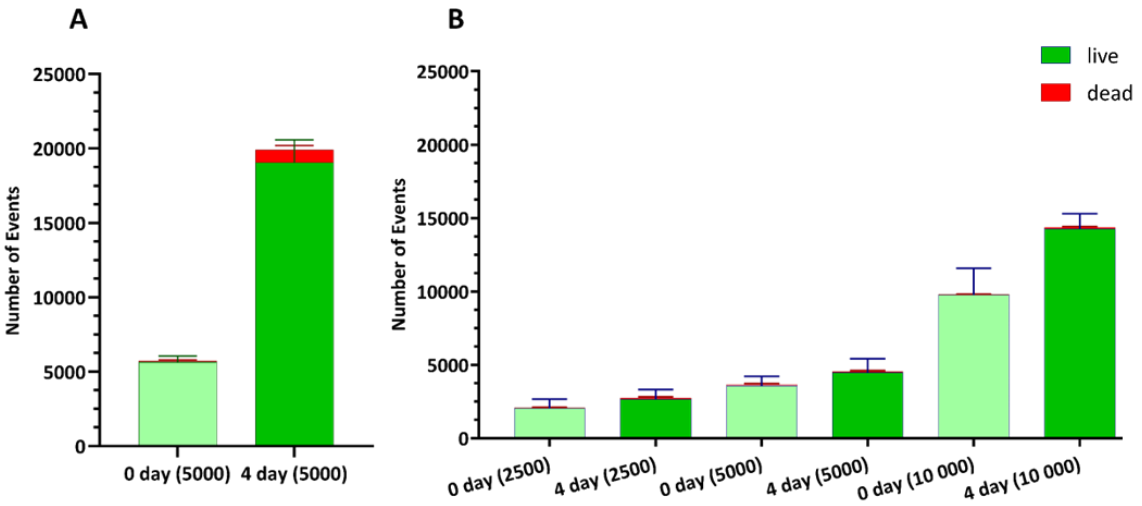

Figure 3.12: Flow Cytometry Population Analysis of A549 and MRC-5 Cells. The mean number of events of A549 (A) and MRC-5 (B) cells per 200 µL (n=6). The number of live events were determined using Hoechst staining Green) and the number of dead events was determined using propidium iodide (PI) stain (red). Data used to generate these results were from 3 independent repeats with 3 spheroids per plate ($n_{replicates}$= 9).

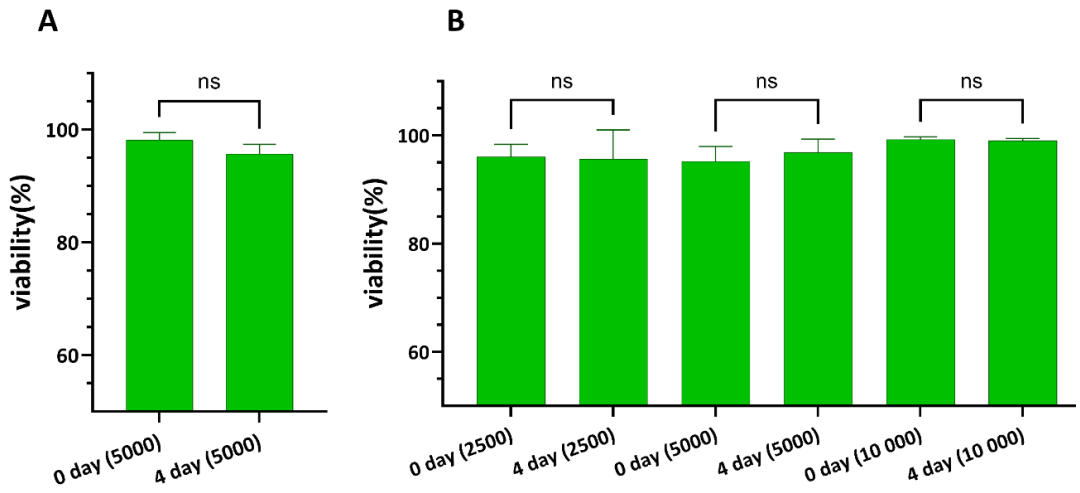

Figure 3.13: Viability as a percentage generated from PI staining of A549 (A) and MRC-5 (B) cells. Statistical significance is indicated with **** (p <0.001), when statistical significance was not obtained (P >0.05) it has been indicated with ns. Statistical significance was generated using the two-way ANOVA and Šídák's multiple comparisons test in graph pad prism 10.

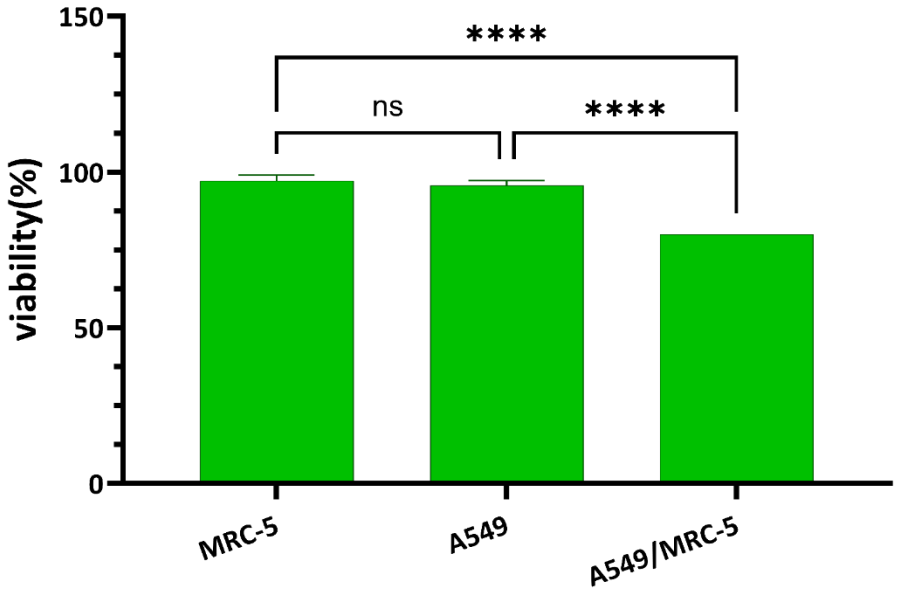

Figure 3.14: Viability as a percentage generated from PI staining of 4 day old A549-MRC-5 heterotypic spheroids compared to 4 day old homotypic spheroids (5000 cells/well/cell line). Statistical significance is indicated with **** (p <0.001), when statistical significance was not obtained (P >0.05) it has been indicated with ns. Statistical significance was generated using the two-way ANOVA and Šídák's multiple comparisons test in graph pad prism 10.

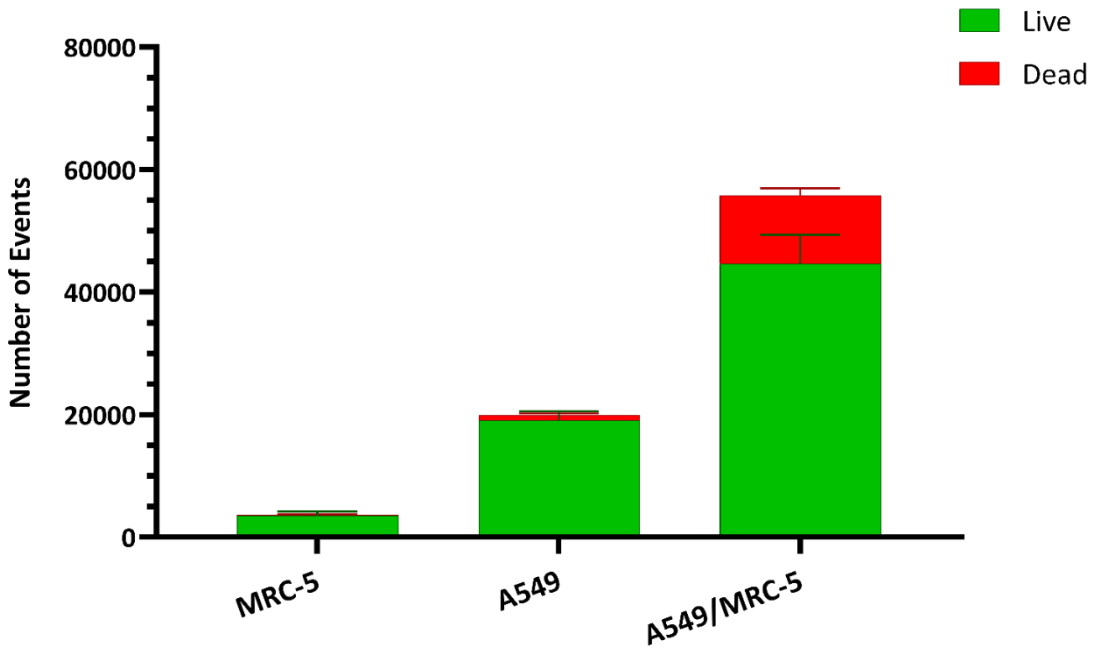

Figure 3.15: Flow Cytometry Population Analysis of A549 and MRC-5 spheroids. The mean number of events of A549 and MRC-5 spheroids (5000 cells per spheroid seeded) compared to the heterotypic spheroids (Ratio of 1:1, maintaining an A549 cell density of 5000) (n=6). The number of live events were determined using Hoechst staining (Blue) and the number of dead events were determined using propidium iodide (PI) stain (red).

3.4. Cell viability using Trypan Blue Exclusion

Cell viability was assessed using the trypan blue exclusion. Trypan blue dye solution stains dead cells blue without affecting the viable cells. Using a haemocytometer, live and dead cells were counted, and the percentage of viable cells was calculated. The cell count used for seeding spheroids was recorded and viability was calculated and displayed as time point 0 days in the below graph (figure 3.16). Each dissociated spheroid, grown for 4, 8 and 12 days, underwent trypan blue staining and was counted in a haemocytometer twice. Results indicate that viability decreases over time for A549 homotypic spheroids and A549-MRC-5 heterotypic spheroids. However, interestingly with tri-cultured heterotypic spheroids, the percentage viability decreased to 72% in spheroids grown for 4 days but increased to 76% in spheroids grown for 12 days. It is important to note that at the 0 day time point, cell viability was not 100%, this may be due to normal cell culture procedures such as some cells dying due to exposure to trypLE, overcrowding within the culture flask or passive cell death.

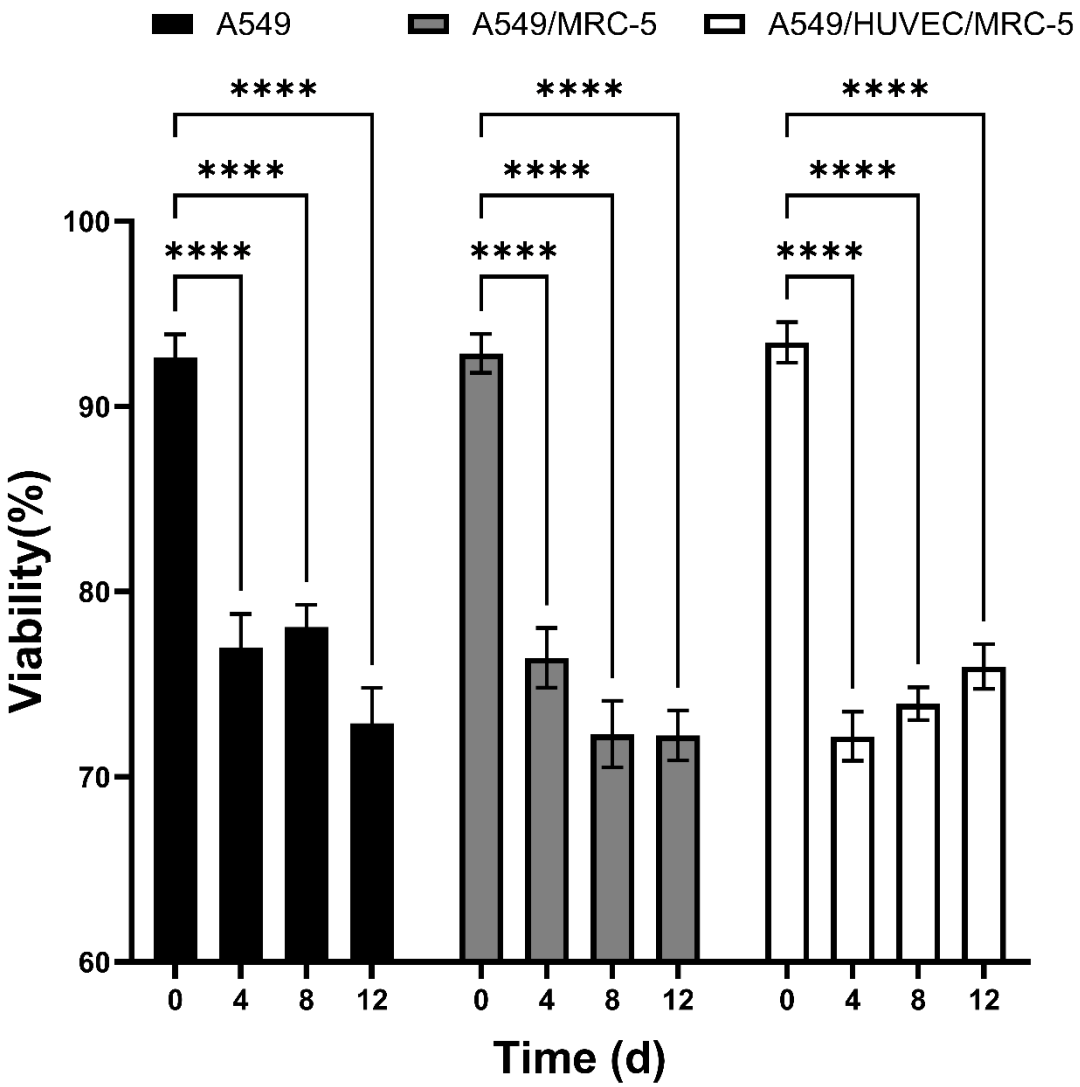

Figure 3.16: Cell viability as a percentage (%) derived from the trypan blue exclusion of A549 homotypic spheroids and A549/MRC-5 and tri-cultured heterotypic spheroids. Data used to derive the results were from two cell counts per spheroid, three spheroids per repeat and 3 independent repeats in total ($n_{replicates}$ = 9). Statistical significance is indicated with **** (p <0.0001), when statistical significance was not obtained (P >0.05) it has been indicated with ns. Statistical significance was generated using the two-way ANOVA and Tukey's multiple comparisons test in graph pad prism 10.

3.5. Cell Viability using ATP Quantification using CellTiter-Glo®

Cell viability was assessed using ATP quantification using CellTiter-Glo® luminescent cell viability assay. Relative luminescence is indicative of the amount of ATP generated by the cells and is indicative of viability, the higher the luminescence, the more ATP the higher the number of viable cells.

The results shown in figure 3.17 indicate that relative ATP luminescence was higher for spheroids with initial seeding densities of 5000 cells than 2500 and 1000 cells/spheroid

(figure 3.17A). Additionally, relative ATP luminescence increased as time increased for both A549 and MRC-5 cells. However, MRC-5 cells have a significantly lower relative ATP luminescence compared to A549 cells (figure 3.17B). Furthermore, relative ATP luminescence of heterotypic spheroids showed less variability at a ratio of 1:2 (A549: MRC-5) and 5:2, whilst the relative luminescence of 1:1 and 2:1 showed more variation (higher standard deviation) (figure 3.18). Moreover, results indicated that an increase in relative luminescence occurred as time increased for heterotypic spheroids at a ratio of 1:1, 2:1 and 1:2. Additionally, the relative ATP luminescence of tri-cultured heterotypic spheroids was conducted. Results indicate that relative ATP luminescence increased over time in line with the A549-MRC-5 heterotypic spheroids with a ratio of 1:1 (figure 3.19). Consequently, CellTiter-Glo® luminescent cell viability assay showed that ATP was produced stably over time for all culture types.

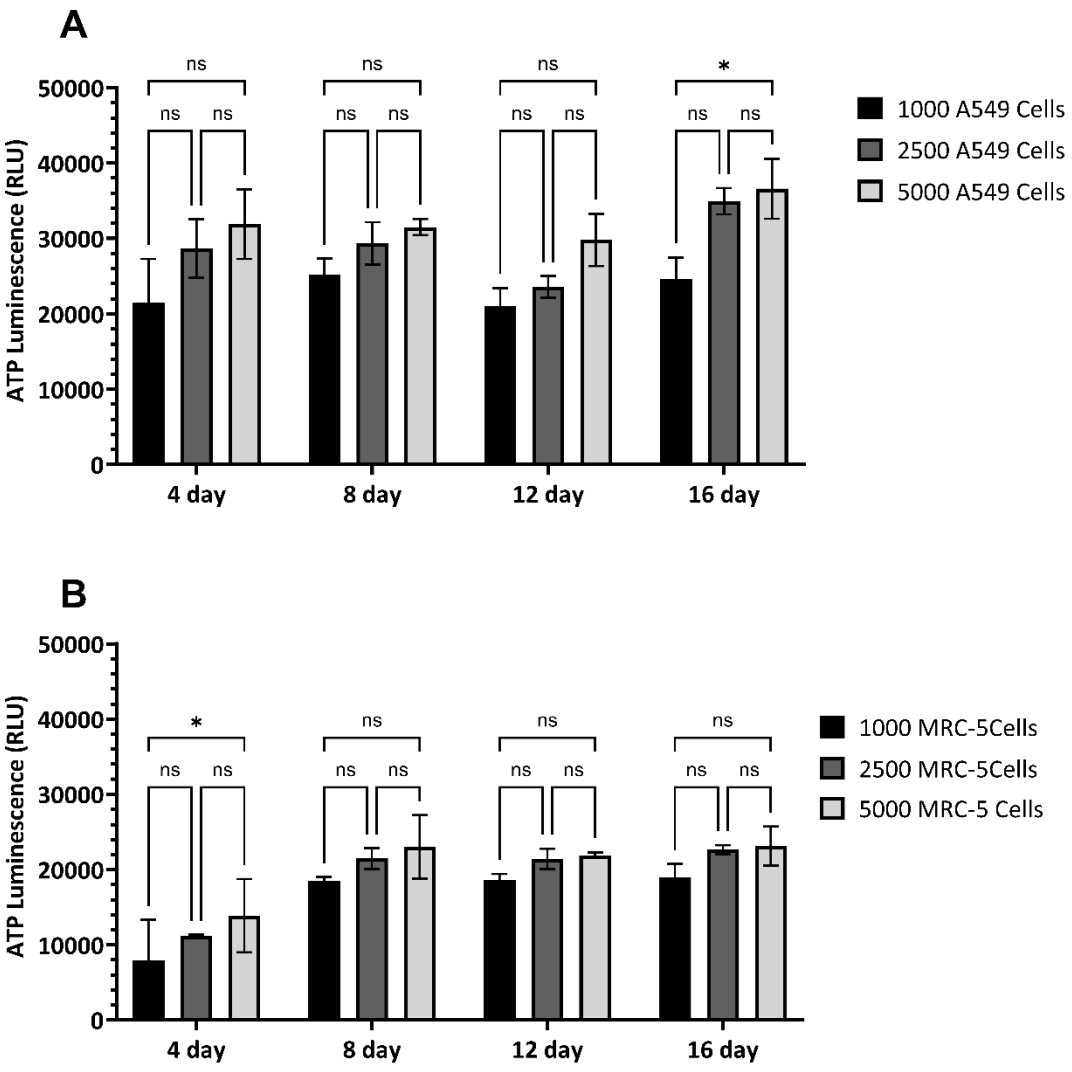

Figure 3.17: Graph displaying the mean relative ATP luminescence of A549 (A) and MRC-5 (B) spheroids seeded at different densities. Data used to generate these results were from

3 independent 96-well plates with 3 spheroids per plate for each seeding density ($n_{replicates}$=9). Statistical significance is indicated with * (p <0.05), when statistical significance was not obtained (P >0.05) it has been indicated with ns. Statistical significance was generated using the two-way ANOVA and Tukey's multiple comparisons test in graph pad prism 10.

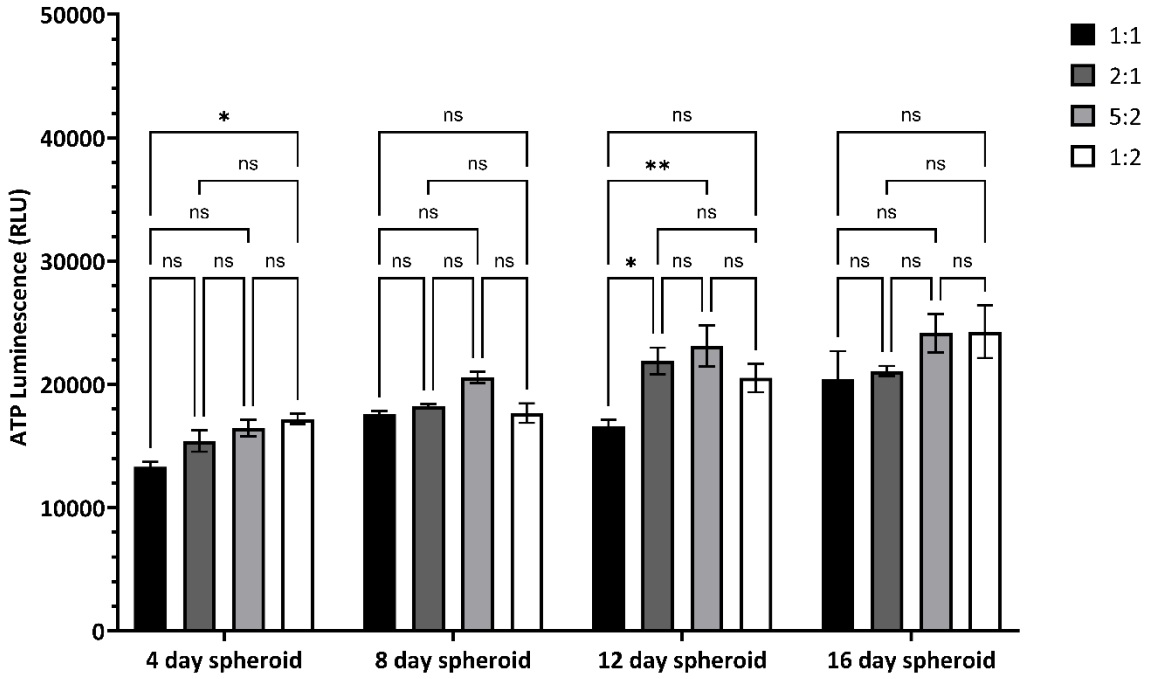

Figure 3.18: Graph displaying the mean relative ATP luminescence of A549 and MRC-5 heterotypic spheroids at varying rations of A549:MRC-5 cells.Data used to generate these results were from 3 independent 96-well plates with 3 spheroids per plate for each seeding density. Statistical significance is indicated with * (p <0.05) or ** (p <0.01), when statistical significance was not obtained (P >0.05) it has been indicated with ns. Statistical significance was generated using the two-way ANOVA and Tukey's multiple comparisons test in graph pad prism 10.

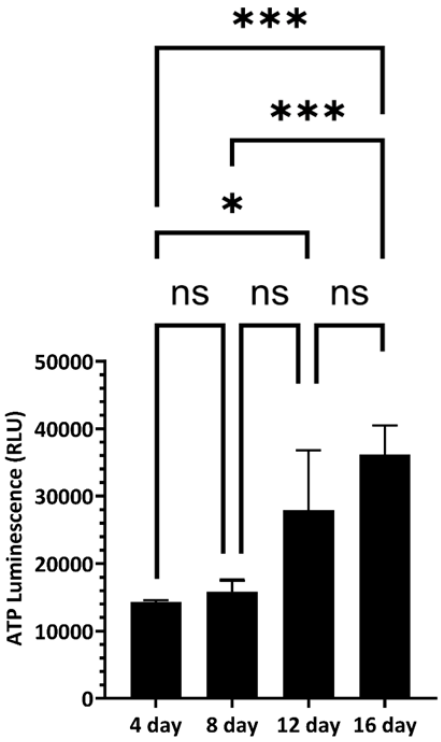

Figure 3.19: Graph displaying the mean relative ATP luminescence of tri-cultured heterotypic spheroids at different time points. Data used to generate these results were from 3 independent 96-well plates with 3 spheroids per plate for each seeding density. Statistical significance is indicated with * ($p < 0.05$) or *** ($p < 0.001$), when statistical significance was not obtained ($P > 0.05$) it has been indicated with ns. Statistical significance was generated using the two-way ANOVA and Šídák's multiple comparisons test in graph pad prism 10.

3.6. Internal characteristics using Immunofluorescent microscopy.

Whilst spheroid morphological analysis has provided some insight into the external characteristics of spheroids, internal structure and features including biological activity need to be assessed. Immunofluorescent microscopy was used to visualise the expression of specific proteins including Antigen Kiel 67 (Ki-67) and Alpha smooth muscle actin (α-SMA). Images of spheroids stained with Ki-67 show that after 4 days of growth, homotypic and heterotypic spheroids express Ki-67 (figure 3.20). In A549 homotypic spheroids and tri-cultured heterotypic spheroids, Ki-67 is spread throughout the spheroid indicating that cells are proliferating throughout the spheroid. However, in MRC-5 homotypic and A549-MRC-5 heterotypic spheroids, Ki-67 is localised towards the outer rim. This indicates that the spheroids at day 4 have developed an inner core of non-proliferating cells and an outer core of proliferating cells.

Alpha smooth muscle actin (α-SMA) is exclusively expressed by MRC-5 cells and consequently can be used as an indicator of MRC-5 presence and localisation within a

spheroid. Images in figure 3.21 show spheroids stained for α-SMA revealed that A549 homotypic spheroids express no α-SMA whilst MRC-5 homotypic spheroids and A549-MRC-5 heterotypic spheroids and tri-cultured heterotypic spheroids express α-SMA localised towards the rim of the spheroid (figure 3.21). Furthermore, to determine if the number of MRC-5 cells seeded affects the expression of α-SMA, A549-MRC-5 heterotypic spheroids with a ratio of 2:1 A549s: MRC-5s were stained for α-SMA. Images show that the intensity of α-SMA staining was reduced in the 2:1 ratio in comparison to the 1:1. Therefore, α-SMA expression is dependent on the number of MRC-5 cells present.

To further assess the internal features of spheroids, CD31 and HIF-1α were used to indicate the presence and localisation of HUVEC cells and hypoxia, respectively. The expression of CD31 is restricted to ECs, tri-cultured heterotypic spheroids stained with anti-CD31 show that at 4 days, HUVEC cells are spread throughout the spheroid (figure 3.22). Tri-cultured heterotypic spheroids grown for 8 days have a reduced expression of CD31 which is localised towards the outer rim of the spheroid. However, spheroids grown for 12 days show more CD31 expression localised to the outer rim than spheroids grown for 8 days.

Finally, spheroids were assessed for the expression of HIF-1α, an indicator of hypoxia. Images show that HIF-1α is expressed in A549 homotypic spheroids, A54-MRC-5 heterotypic spheroids and tri-cultured heterotypic spheroids after 4 days of growth (figure 3.23). The intensity of HIF-1α stain in the tri-cultured heterotypic spheroids was higher than that seen in the A54-MRC-5 heterotypic spheroids, whilst the intensity seen in A549 cells was the lowest.

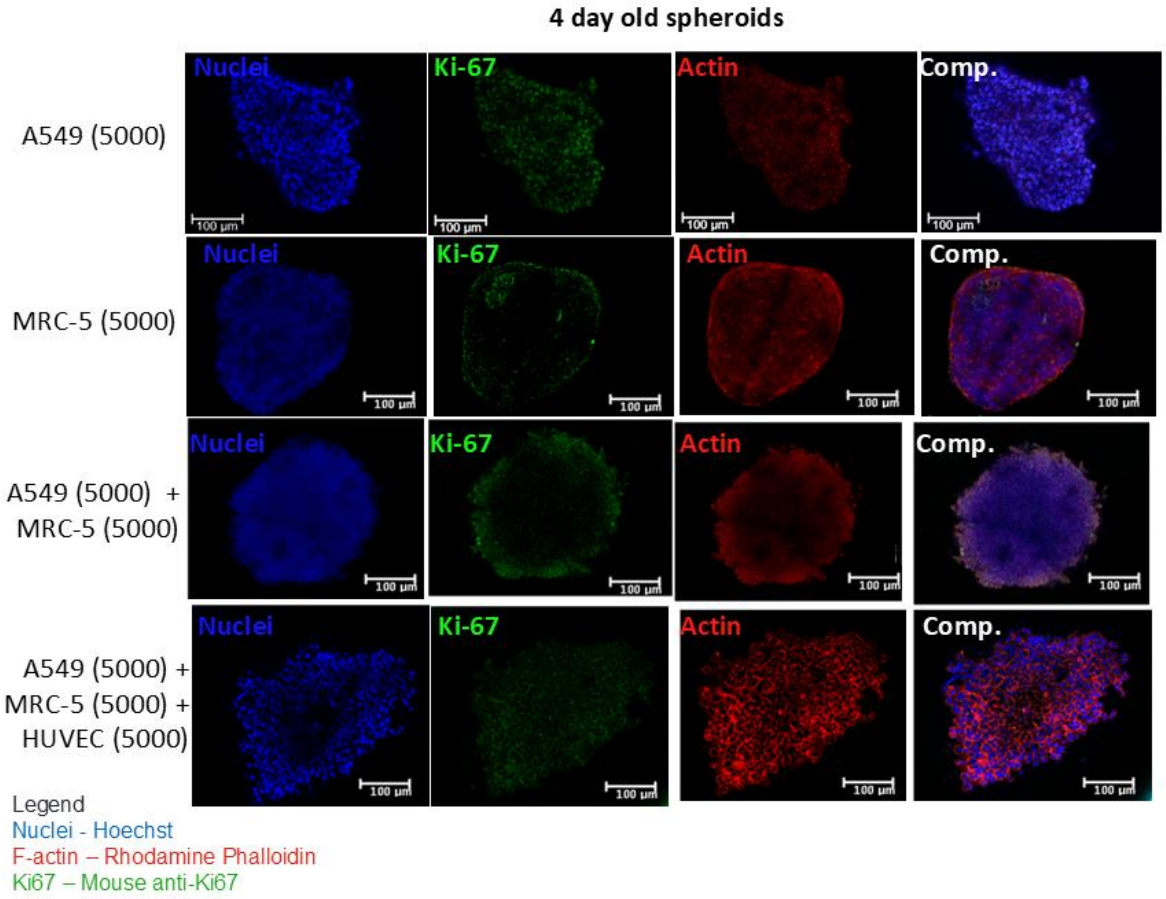

Figure 3.20: Representative Confocal images of A549, MRC-5, and heterotypic spheroids stained with Hoechst (blue), Rhodamine phalloidin (Red), and Ki-67 (Green). Images were captured using a magnification of 10X. Scale bar = 100 µm

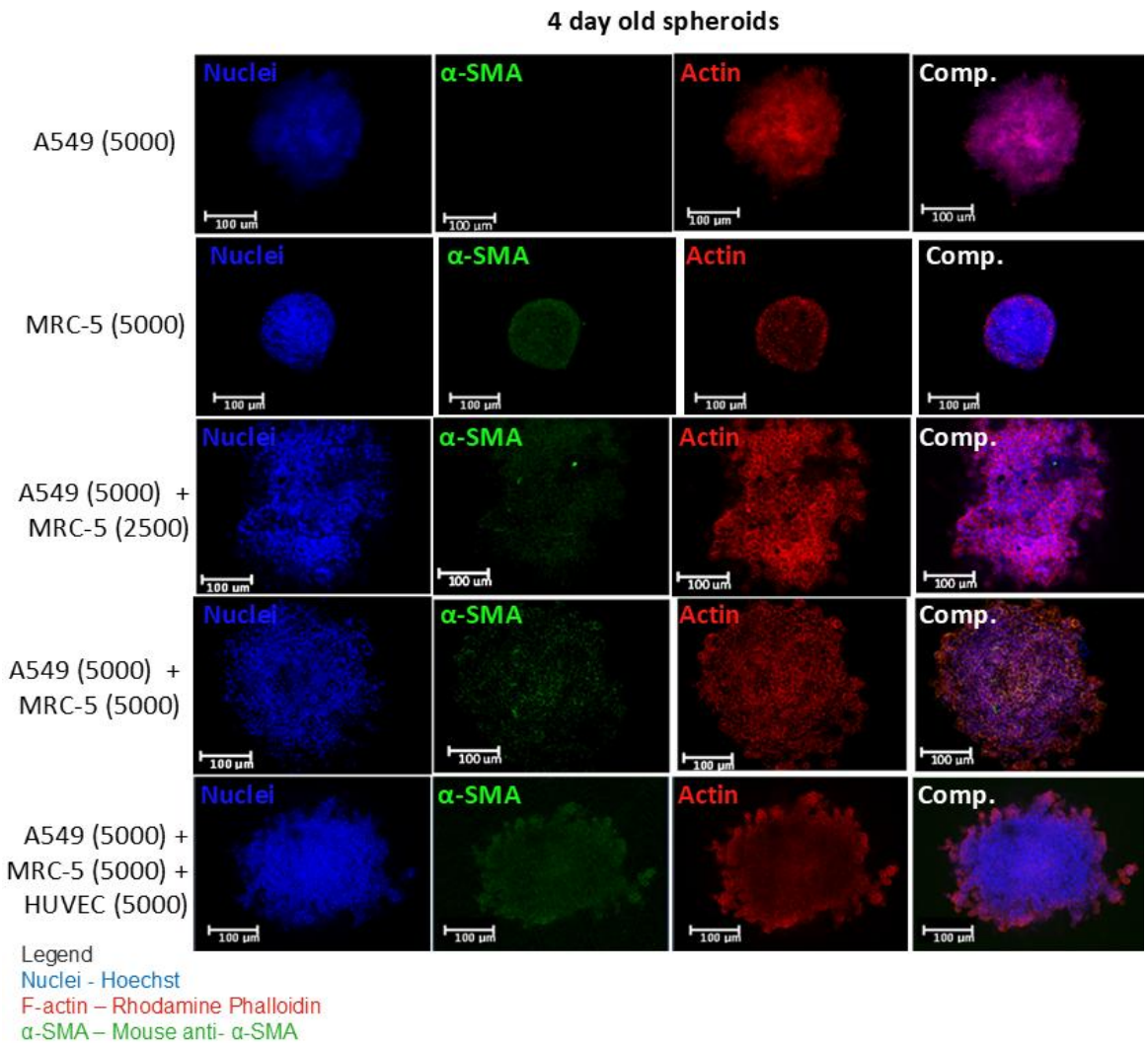

Figure 3.21: Representative Confocal images of 4 day old A549, MRC-5, and heterotypic spheroids stained with Hoechst (Blue), Rhodamine phalloidin (Red) and α-SMA (Green). Images were captured using a magnification of 10X. Scale bar = 100 µm

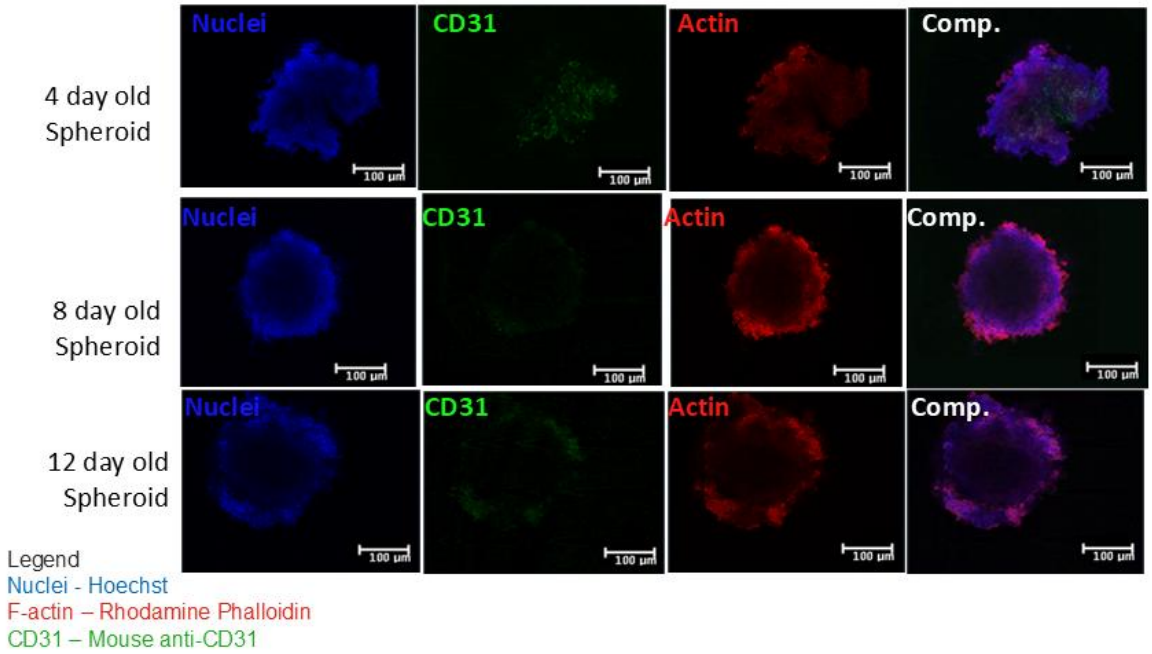

Figure 3.22 : Representative Confocal images of 4 day old A549, MRC-5 and heterotypic spheroids stained with Hoechst (Blue), Rhodamine phalloidin (Red) and CD31 (Green). Images were captured using a magnification of 10X. Scale bar = 100 µm.

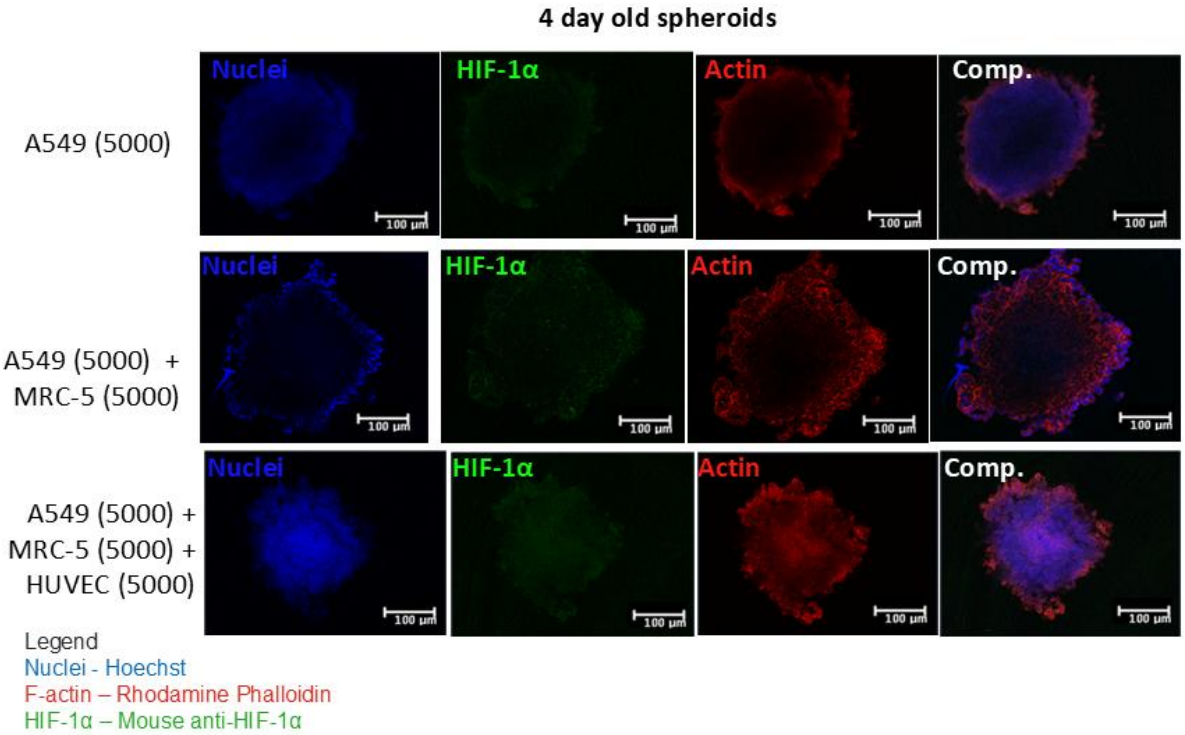

Figure 3.23 : Confocal images of 4 day old A549, MRC-5 and heterotypic spheroids stained with Hoechst, Hoechst (Blue), Rhodamine phalloidin (Red) and HIF-1α (Green). Images were captured using a magnification of 10X. Scale bar = 100 µm.

3.7. Confirmation of VEGF-A and HIF-1α expression using western blot.

Protein analysis was conducted to quantify the expression of HIF-1α and VEGF-A using western blotting (figure 3.24). A total of 16 Tri-cultured heterotypic spheroids at different time points were lysed to conduct a western blot. Results show that HIF-1α is slightly present in spheroids grown for 4 and 8 days whilst peaking at 12 days but remaining present at 16 days of growth. Furthermore, VEGF-A was present at all time points. However, as the western blot is an image of one experimental replicate, no quantitative date was extractable.

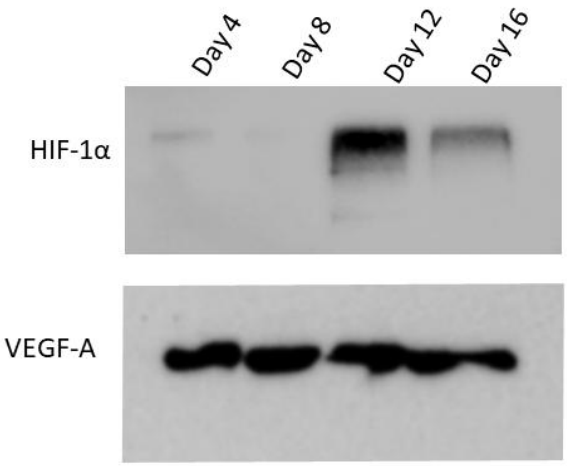

Figure 3.24: Western blot for HIF-1α and VEGF-A. Cell lysates were harvested from 16 tri-cultured heterotypic spheroids grown for 4,8,12 and 16 days. HIF-1α bands were located at approximately 90 kDa and VEGF-A bands were located at approximately 20 kDa. Image shown is of 1 single gel used to probe for HIF-1α and VEGF-A

4. Discussion

Spheroids are aggregated structures which can be formed by multiple cells that can resemble some of the architecture and biological characteristics of solid tumours. It is well established that spheroids have a hypoxic core that often becomes necrotic as a result [16]. Spheroids are becoming an increasingly popular method for 3D cell culture. Research into new *in vitro* models that can better mimic *in vivo* environments has also grown in popularity. To develop more complex models, such as lung on a chip or microfluidic models that incorporate shear stress and flow, the co-culture of several cell lines into spheroids can be seen as one way to increase complexity.

Tri-cultured heterotypic spheroids provide an advanced approach to increasing the complexity of *in vitro* tumour models through the incorporation of multiple cell types, allowing for better mimicry of the TME. This allows research into the signalling between cancer cells, endothelial cells, and stromal cells, which is crucial for understanding the regulation of angiogenesis. Whilst homotypic spheroids have proven beneficial, heterotypic spheroids that incorporate endothelial cells have shown enhanced utility in angiogenesis assays [46]. Studies using spheroids in combination with other models such as the lung on a chip model have been successful, developing novel techniques that can be used to build on the complexity of *in vitro* culture systems [94, 95]. Due to their increased complexity, tri-cultured spheroids therefore serve as a valuable step between traditional spheroid models and more advanced microfluidic tumour-on-a-chip systems, contributing to the development of robust and reproducible *in vitro* platforms for studying NSCLC angiogenesis and therapeutic response [96]. Whilst spheroids provide a simple precursor to these more advanced models, they still providing more physiologically relevant information than traditional 2D cell cultures[13, 28]. Spheroid characteristics such as the hypoxic core can benefit more complex models developed to investigate angiogenesis, as the hypoxic core is one of the first steps in stimulating the angiogenic cascade. As tumour angiogenesis plays a significant role in tumour progression and therapeutic response, increased angiogenesis in NSCLC patients often correlates to a poorer prognosis [97]. Novel preclinical models that can mimic tumour angiogenesis in NSCLC are being explored as a result of current therapies showing limited clinical benefits [98].

Tumour angiogenesis is typically stimulated due to the lack of nutrients and oxygen within the tumour and is often triggered by hypoxia [70, 74, 99]. The development of a hypoxic core within spheroids means that they have the potential to stimulate angiogenesis within a more complex model so that novel treatments can be tested. However, few studies effectively evaluate or preselect spheroids based on their overall morphological characteristics, such as circularity, compactness, solidity, volume or size. Zanoni *et al* showed that the overall spheroid morphology can affect the internal characteristics and biological responses of spheroids (figure 6.1). This should be a significant factor to consider when developing a more complex model specific for tumour angiogenesis research [15, 100, 101]. Inconsistency in spheroid morphology and size can introduce inaccuracies particularly when evaluating therapeutic response. This is due to larger spheroids having multiple cell layers, with the core experiencing reduced oxygen, nutrients and growth factors [15, 16]. Furthermore, misshapen spheroids can have differences in the surface area in the outer core of the spheroids; thus affecting the viability of cells throughout the spheroid as well as the gradient of growth factors including angiogenic factors within the spheroid [15, 16].

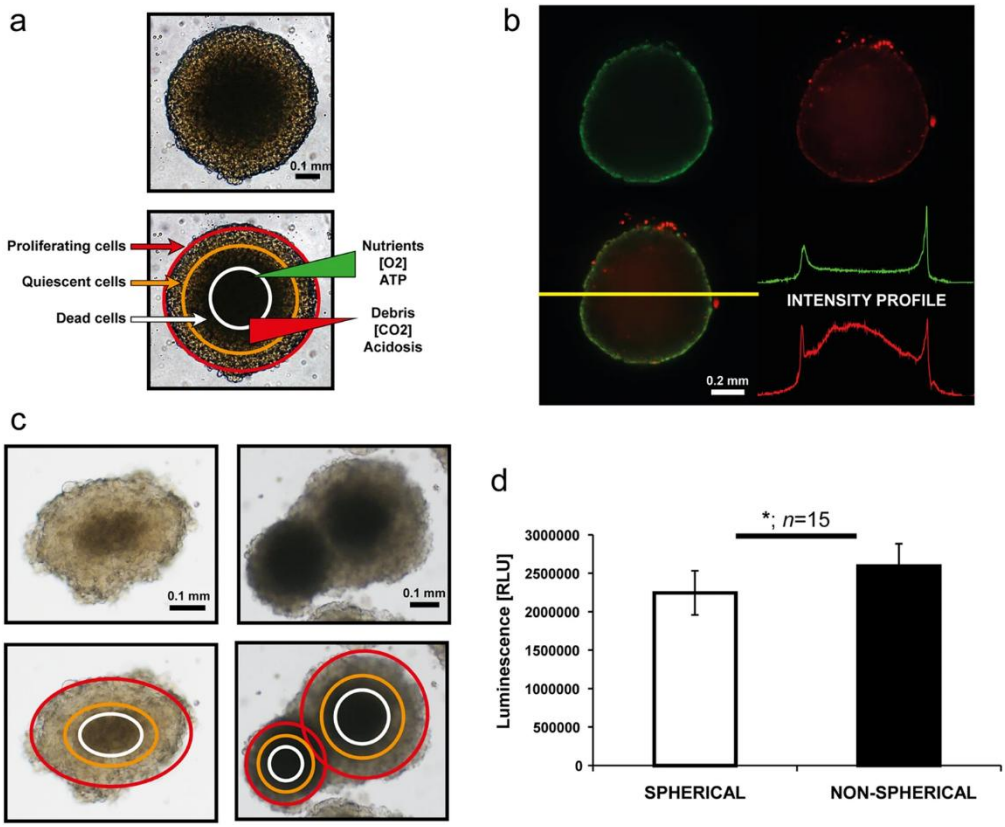

Figure 6.1: The impact of spheroid shape on Viability and shows the relationship between shape and viability of cells. Where A shows the inner ring of dead/necrotic cells, a mid ring of quiescent cells and an outer ring of proliferating cells, B shows a live, spherical spheroid imaged with light sheet fluorescence microscopy (LSFM, Lightsheet Z.1, Zeiss).

Green = calcein-positive (live) cells; red = ethidium-positive (dead) cells. Scale bar = 0.2 m. C shows that variability in tumour shape results in alterations to the inner core size and thickness of the outer layers. D shows the cell viability of spheroids with a homogenous volume but different shapes (spherical vs non-spherical) using CellTiter-Glo®3D Cell Viability assay. (Zanoni *et al*., 2016) [15].

These differences in size and shape can therefore affect the hypoxic core and diffusion distances which can impact drug penetration and thus influence dose-response characteristics [15, 16]. For example, a drug may be less effective in larger spheroids due to its inability to diffuse uniformly throughout the spheroids, whereas in smaller spheroids or less compact spheroids, it may be more potent [102, 103]. Additionally, the size variability of spheroids can affect experimental consistency. Large spheroids typically contain a higher density of cells and thus require a higher drug concentration to achieve the same therapeutic effect as seen in smaller spheroids. The inconsistency in size can therefore skew experimental outcomes, making it challenging to establish reliable and reproducible dose-response relationships [102-104]. Therefore, the characterisation and selection of spheroids with consistent morphology are necessary to develop reliable and predictive 3D cell culture models for drug development. Additionally, for the development of models that are more complex than 3D spheroids, such as microfluidic devices, the preselection of spheroids at specific time points that are in the same growth phase and similar circularity can be crucial in limiting the variation in the model formed. By controlling the initial seeding density and cell ratios, and selecting spheroids of a specific size, circularity and solidity, researchers should be able to develop a robust complex model, such as microfluidic devices, that can mimic NSCLC angiogenesis [15, 33, 100, 101, 105, 106]. For example, Hirschhaeuser *et al* suggest that A549 spheroids grown in ULA plates respond differently to cisplatin dependent on spheroid size [107]. Spheroids with a diameter over 400 µm showed lower cisplatin sensitivity in comparison to spheroids under 200 µm. It was suggested that this was due to limited drug penetration into the spheroid core of larger spheroids. Thus smaller spheroids with a higher surface area to volume ratio allowed efficient drug diffusion in comparison to larger spheroids [106]. However, Riffle *et al* demonstrated that large spheroids can be useful in researching hypoxic regions within the spheroid and how this can regulate tumour angiogenesis through HIF-1 α. The large spheroid size is therefore essential in creating the hypoxic gradient within the spheroid and how this can trigger angiogenic pathways [108].

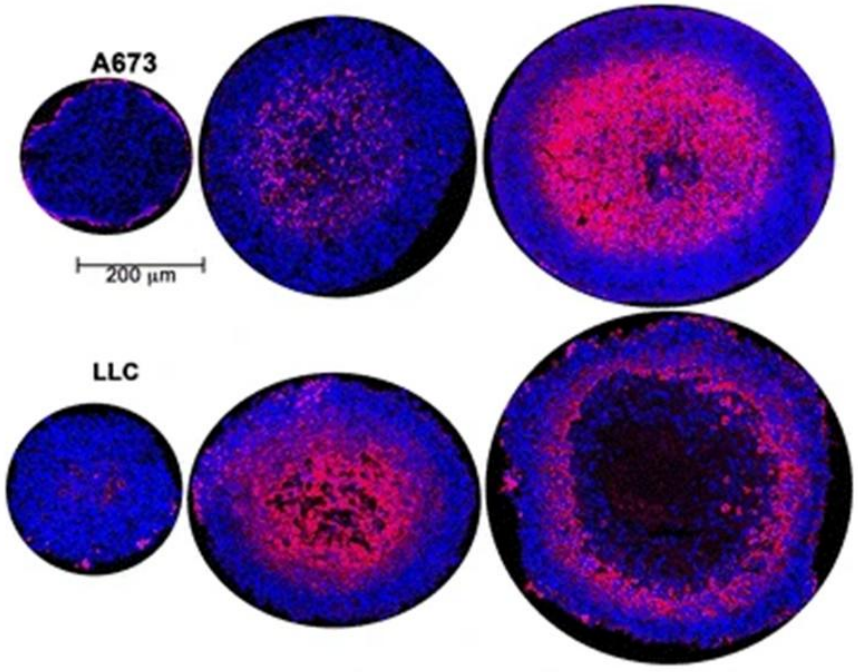

Figure 6.2: Image showing the development of hypoxia in growing spheroids. Images show immunostaining of A673 and LLC spheroids. Spheroid cryo-sections were stained for the hypoxia marker pimonidazole (red) and indicates the hypoxia development at different sizes in the central core. Cells were counter stained with Hoechst 33342. (Riffle *et al.*, 2017)) [108].

My project demonstrates that assessing the three morphological characteristics of spheroids, namely circularity, solidity and diameter, to develop a preselection method ensures spheroids generated have a circularity of 0.8 or higher, a solidity of 0.4 or higher and a diameter of 400 µm or higher. Whilst previous research has suggested that spheroids with a diameter over 400 µm have lower sensitivity to therapeutics due to limited drug penetration, this is a necessary requirement for spheroids that will be used in a more complex model, like microfluidic devices, to research NSCLC angiogenesis [106, 108]. This selection criteria was then used to select spheroids for subsequent assays. Consequently, the results generated following this preselection were less variable. This was in line with the study conducted by Zanoni *et al* which showed that through the use of a preselection method to control the circularity and volume of spheroids, variability in subsequent cytotoxicity assay was reduced [15]. Furthermore, Gunay *et al* showed that preselecting spheroids based on uniform size and shape reduces variability in drug resistance assays [101]. Larger and irregular spheroids were found to exhibit higher drug resistance. However, through the use of a selection method, which standardised spheroid size, more reliable and consistent results were achieved. This further supports the findings of my

project which demonstrated that controlling spheroid morphology characteristics can improve reproducibility.

Having confirmed the growing evidence shown in literature, in my work, I have also shown that cell type, cell densities and culture time affect the morphology of spheroids. Understanding how cell type, cell density and culture time can affect morphology can enable researchers to select spheroids with the most physiologically relevant phenotype depending on the research being carried out. For example smaller spheroids (less than 200 µm) for dose-response testing or larger spheroids (more than 400 µm) for researching hypoxia. Predicting the spheroid morphology by controlling these parameters can enable the development of more consistent and reliable 3D models to be generated [84].

For instance, in the results presented when using the MRC-5 cells, I showed that these cells produced spheroids with a rounder, smoother edge compared to A549 cells for the same seeding densities. Interestingly, this may be due to the production of collagen by MRC-5 cells which assist cell aggregation and the formation of the ECM as presented in a previous work by Zuchowska *et al*. [79]. The ECM has been shown to regulate several processes including proliferation and migration, and thus ECM production by MRC-5 cells within the heterotypic spheroid could play an important role in the resulting angiogenic potential of the spheroids [109]. Cross-talk between cancer cells and stromal cells is a critical regulator of angiogenesis, as shown by the upregulation of proangiogenic factors like VEGF within these 3D models [74]. Whilst homotypic spheroids of MRC-5s may have altered ECM protein secretions due to being cultured in 3D, compared to 2D, it is possible that the heterotypic spheroids have completely different alterations to ECM proteins due to the cross talk between cancer and stromal cells [74, 110].

In my study, homotypic spheroids of different cell densities were initially assessed to determine what cell density produced the most consistent morphology as cell density is one of the factors that can introduce variability in spheroid morphology [15, 100, 101, 105]. My results showed that spheroids consisting of lower cell densities are more variable and have a lower overall circularity compared to spheroids with a higher seeding density. A study by Białkowska *et al* showed that spheroids seeded with lower cell densities show greater variability in size and shape and often have lower circularity. It was suggested that this inconsistency was as a result of reduced cell-cell interactions and incomplete aggregation, an outcome observed more prominently at lower seeding densities[111].

Consequently, results observed in my project are in line with this work and further support the suggestion that lower seeding densities produce spheroids with more variability in size and shape. Thus reinforcing the significance of optimising cell seeding densities when developing novel models to research NSCLC angiogenesis.

Results obtained in my project therefore shows that by taking into account the analysis of the overall spheroid circularity, solidity and diameter, A549 homotypic spheroids of 5000 cells/spheroid can generate spheroids with less variation in the circularity, solidity and diameter (figure 3.8 and 3.9). This highlights the importance of using morphology characteristics as a robust indicator for selecting suitable spheroids for further testing, such as drug response evaluations. Furthermore, as previously discussed, selecting the most suitable characteristics that produce spheroids which have the most relevant physiology depending on the type of research question is important to consider. In my project, as spheroids were being assessed as the basic building blocks that would be used to develop a more complex model like lung-on-a-chip or microfluidic devices, larger spheroids that had developed a hypoxic core were required. As such, the parameters for inclusion were set to a circularity of 0.8 or higher, a diameter of 400 µm or more and a solidity of 0.4. These spheroids would be large enough to have a hypoxic core, consistency in circularity regulated the surface area to volume ratio and the low solidity, which is indicative of proliferation, showed that spheroids were in the growth phase and more likely to have developed a hypoxic core.

Additionally, using this assessment method, differences between the morphological characteristics of A549 and MRC-5 homotypic spheroids were observed. MRC-5 spheroids aggregated faster, this can be seen in the multivariate graphs (figure 3.8) which shows that MRC-5 spheroids are more compact and smaller than A549 spheroids, whilst A549 spheroids showed higher circularity measurements. Furthermore, A549 spheroids exhibited more variation which is in line with observations by Zanoni *et al* and Saleh *et al*. They suggest that the variation in A549 spheroids is dependent on cell density and the technique used for spheroid formation [15, 87]. Additionally, Zuchowska *et al* suggest that MRC-5 cells have an enhanced ability to aggregate due to their capacity to secrete collagen for ECM formation [79]. The results observed in my project support this suggestion as MRC-5 spheroids aggregated faster and formed more compact spheroids.

As reported in the literature, there is disagreement in the ratio of lung fibroblasts to NSCLC cells forming the TME. The specific ratios used often depend on the functional outcomes required for the experiment. For instance, Vicent *et al* showed that the presence and density of fibroblasts can impact tumour behaviour through the use of NSCLC cell lines in a mouse model. They further showed that the CAF phenotypes that influence NSCLC function differently depending on their proportions [112]. Additionally, variability in fibroblast-to-cancer cell ratios in co-culture models was shown by Mei *et al* through the use of 3D bioprinting lung cancer models to emphasise the different ratios of fibroblasts to NSCLC cells. In this study, specific ratios were chosen based on the required simulation of the tumour's physiological characteristics [113]. Whilst variability is seen in these ratios, Amann *et al* suggest that NSCLC typically contains a higher proportion of tumour cells to stromal cells [35]. This was shown by culturing a higher proportion of fibroblasts with tumour cells and observing the change in fibroblasts after 10 days. The results showed that there was 19% more tumour cells than fibroblasts [35]. However, they also further highlight the pivotal role of fibroblasts in tumour progression and angiogenesis in the TME. Once the optimal number of fibroblasts was determined, Amann *et al* found that fibroblasts significantly enhance both tumour growth and vascular formation [35]. Thus highlighting the influence of fibroblasts in the TME and indicating that fibroblasts are crucial for replicating angiogenesis *in vitro*. This intriguing aspect led to the investigation of the relationship between various cell density ratios and morphological characteristics (such as circularity and solidity) to be assessed in my work when co-culturing heterotypic spheroids of A549 and MRC-5 cells. As presented in the results section, the morphology assessment of spheroids using circularity and solidity revealed that A549-MRC-5 heterotypic spheroids aggregated faster than A549 homotypic spheroids but slower than the MRC-5 homotypic spheroids (figure 3.8 and 3.9). This further supports the suggestion that MRC-5 cells aggregate fast due to the expression of ECM proteins. In addition, solidity, the measure of the smoothness of the spheroid, can be indicative of cell proliferation and thus indicates spheroids are in the growth phase. A549 homotypic spheroids show high variability in all 3 morphology parameters (circularity, solidity and diameter) in comparison to MRC-5 cells (figure 3.8A and 3.8B). The results obtained by assessing these parameters indicate that by 12 days, A549 homotypic spheroids are compact and have fewer proliferating cells on the outer rim in comparison to 1, 4 and 8 day old spheroids. As previously discussed, the faster aggregation of MRC-5 cells compared to A549 cells can be associated with their role in

promoting cell-cell adhesions and production of the ECM [112]. The high variability seen in A549 spheroids aligns with Amann *et al* who show that tumour cells form a more irregular structure when mono-cultured, whereas when co-cultured with fibroblasts a more consistent and smooth spheroid shape was observed [35]. In addition, the reduced proliferation in A549 cells in A549 homotypic spheroids seen after 8 days is in line with known growth dynamics of spheroids where nutrient diffusion is limited [107, 114, 115]. This is indicative of an increase in the hypoxic condition which typically slows cell proliferation in the outer layers of older and larger spheroids [107, 114, 115]. Thus, the relationship between cell density ratios, spheroid morphology (including circularity, solidity and size) and spheroid aggregation observed in my work is in line with the existing literature and further highlights the significant role fibroblasts have in tumour progression and angiogenesis.

Known growth dynamics of spheroids suggest that spheroids with reduced proliferation at the outer rim are often in the growth phase and thus more likely to have a hypoxic core [114-116]. The morphological characteristics assessed in my work, namely circularity, solidity and diameter, can be together used as an indicator for spheroids that are large enough to have reached the phase at which proliferation has reduced at the outer rim and are therefore have a hypoxic inner core. However, these morphological characteristics are indicative and need to be supported with hypoxia assessments to definitively confirm that a hypoxic core has formed. Furthermore, research suggests that ECs incorporated into heterotypic spheroids to develop the tri-cultured spheroids can promote angiogenesis-associated signalling and lead to the formation of vascular-like structures within the spheroid [47, 74, 110]. The incorporation of endothelial cells into the spheroid can enhance the hypoxic regions and pro-angiogenic signalling within the spheroid [9]

Zhang *et al* show that spheroids have an increase in ATP production as they mature over time. This was revealed using a DNA-based nano-sensor, which allows continuous monitoring without disturbing the growth process, to monitor ATP levels in spheroids over extended periods of time [117]. They discovered that as spheroids increase in size, the metabolic activity of the cells increases, thus resulting in higher ATP production to meet the energy demands of the proliferating cells [117]. Furthermore, this highlighted that as spheroids mature and develop more complex structures such as a hypoxic or necrotic core where the metabolic need switches from oxidative phosphorylation to glycolysis to

compensate for the lack of oxygen, a phenomenon often referred to as the Warburg effect [118], a steady rise in ATP levels is observed. This is necessary to sustain cell function as the spheroid further increases in size and creates a more physiologically relevant environment specifically beneficial for studying phenomena like angiogenesis. Therefore, ATP assessment of spheroids can be beneficial as it indicates the viability of cells and can be indicative of the physiological state of the 3D structure, highlighting the metabolic capacity of the spheroid model [81]. ATP assessment using CellTiter-Glo® 3D Cell Viability Assay showed that the production of ATP was stable throughout all culture types (figures 3.17 3.18 and 3.19), indicating consistent cell growth over time. The ATP levels were comparable across all cell ratios, with the 5:2 (A549:MRC-5) ratio generating slightly higher levels of ATP production compared to the other ratios. Through the evaluation of spheroid morphology and metabolic activity, my research has demonstrated the importance of developing standardised and reproducible spheroids that can then be used to develop 3D tumour models like lung-on-a-chip for robust preclinical testing. The findings from my work highlight that by controlling key parameters such as cell type, seeding density and co-culture ratios, it is possible to generate homotypic and heterotypic spheroids with consistent size, shape, and metabolic profiles that can mimic the TME which supports the findings in the literature [119].

Flow cytometry results obtained in my project emphasize the differences in cell proliferation between A549 and MRC-5 spheroids, this is in line with published literature which shows that proliferation rates in 3D cultures are altered. Results revealed that the number of A549 and MRC-5 homotypic spheroids did not follow the expected doubling time for A549 cells (figure 3.12), supporting prior research that demonstrates reduced proliferation in 3D spheroid cultures compared to 2D monolayers [120, 121]. The deviation from typical growth rates highlights the impact that the 3D environment has on tumour behaviour which supports the findings observed by Fischbach *et al* [122]. The techniques used, including flow cytometry, trypan blue and ATP luminescence assays, have provided key insights into the growth dynamics of these spheroids. Specifically, flow cytometry and trypan blue confirmed that while cell numbers did not expand in line with standard doubling rates, relative ATP luminescence increased over time in both A549 and MRC-5 spheroids (figures 3.12, 3.15, 3.16, and 3.17), suggesting ongoing proliferation. This indicates that, as ATP production is an indirect measure of cell viability, viable cells continue to increase despite the lower than expected proliferation rates which is in line with the

research conducted by Zang *et al* as previously discussed [117]. However, the significantly lower ATP luminescence in MRC-5 spheroids suggests that non-tumorigenic cells, like MRC-5, have lower metabolic activity compared to tumorigenic A549 cells, consistent with the findings by Farah *et al* on increased metabolic needs in cancer cells [123, 124]. My work indicated that A549 spheroids exhibited a higher number of dead cells as shown through PI staining (figure 3.13) which supports the suggestion that larger spheroids (more than 400 µm) can develop a necrotic core [114, 123]. This may be due to the higher proliferation rate of A549 cells which results in the faster expansion in size of the spheroid (as observed in the morphology assessment) which ultimately results in the faster formation of a necrotic core in comparison to the MRC-5 spheroids. This suggests that the higher metabolic demand of A549 cells and the limited diffusion due to the increased spheroid size drives the formation of a necrotic core. This is in line with previous research which indicates that a necrotic core is a common feature in solid tumours and can be replicated by larger spheroids [107]. The differences observed in metabolic activity and proliferation demonstrated through flow cytometry, trypan blue exclusion and the ATP CellTiter-Glo® 3D Cell Viability Assay provide some understanding of how the proliferation and metabolic needs vary between tumourigenic and stromal homotypic spheroids.

Findings obtained in my project can provide insights into the proliferation and localisation of cells within spheroids using immunofluorescence staining. Through the use of an anti-Ki-67 antibody, the localisation of cell proliferation within the spheroids was revealed (figure 3.20). Ki-67 is a widely recognised marker for cellular proliferation, seen at all stages of the cell cycle, and its presence and localisation provide valuable information about where cells are proliferating within the spheroid structure [16, 125]. It is well established that spheroids develop an inner hypoxic/necrotic core surrounded by a proliferating outer edge [16, 107, 115]. Images of Ki-67 staining in MRC-5 homotypic and A549-MRC-5 heterotypic spheroids showed that Ki-67 was predominantly observed at the outer rim. However, A549 homotypic and tri-cultured heterotypic spheroids showed Ki-67 staining throughout the spheroid structure, suggesting active proliferation across the entire spheroid. This observation could be explained by the relatively young age (4 days) of the spheroids, as older spheroids are more likely to develop a hypoxic core, limiting proliferation to the outer rim.

To investigate the activation and localisation of fibroblasts into CAFs, immunofluorescent staining with anti-α-SMA was conducted. Images (figure 3.21) show that green fluorescence was present in MRC-5 homotypic and heterotypic spheroids, indicating the presence of activated α-SMA-positive fibroblasts, which is consistent with previous studies showing that fibroblasts in a tumour microenvironment often transition into CAFs [126]. The intensity of α-SMA staining was notably higher in heterotypic spheroids, suggesting that the interaction between A549 and MRC-5 cells may enhance the activation of fibroblasts into CAFs. These findings align with prior research, which has shown that CAFs play a key role in promoting tumour progression and can aid in remodelling the ECM. [127].

In addition, CD31 staining was used to evaluate the presence of HUVEC cells and their localization within the tri-cultured spheroids. CD31 is a well-established marker for endothelial cells and is commonly used to study angiogenesis [128]. Donovan *et al* demonstrated that ECs, such as HUVECs, consistently localise to the outer regions of spheroids and can form capillary-like structures. [129]. Additionally, Saibene *et al* used a tetra-culture model with ECs to show the localisation of CD31 which was limited to ECs within the co-culture [34]. Similar to the CD31 staining results observed in tri-cultured spheroids used in my project, where CD31 was expressed predominantly at the outer rim of spheroids indicating. Both these models highlight the importance of CD31 in assessing endothelial integrity and cell interactions in multi-cell type systems. This is supported by the images of anti-CD31 stained spheroids in my work where CD31 expression was localised to the outer rim of tri-cultured heterotypic spheroids (figure 3.22). This suggests that the tri-cultured spheroids may be promoting early stages of angiogenesis. However, further quantification and characterisation of the potential vascular network formed within the spheroids needs to be done to determine the angiogenic potential of this model. However, Lamichhane et al. developed spheroids composed of endothelial cells, lung epithelial cells and mesenchymal stems cells showed that the epithelial cells were not present within the inner core whilst a small population of endothelial cells where found close to mesenchymal stem cells and were present in the inner core [130]. Indicating that it is possible to for endothelial cells to penetrate the inner core of spheroids.

In addition, anti-HIF-1α staining was conducted to visualise if 4 day old spheroids develop a hypoxic core. Muz *et al* indicate that spheroid size correlates with an increase in hypoxia [131]. Additionally, Friedrich *et al* also demonstrated that larger spheroids tend to develop

more pronounced hypoxic regions due to diffusion limitations [132]. Furthermore, as previously described, spheroids tend to form a proliferating outer rim with a hypoxic core [114-116]. This is supported by my work which shows that images of A549 homotypic, A549-MRC-5 heterotypic, and tri-cultured heterotypic spheroids after 4 days of growth (figure 3.23) expressed HIF-1α. The intensity of staining varied amongst the spheroid types with the heterotypic spheroids exhibiting more HIF-1α staining compared to homotypic spheroids. This may be due to the larger size and increased cell number seen in heterotypic spheroids in comparison to homotypic spheroids. This highlights the significance of cell density and morphology in the formation of the hypoxic cores, a key factor in tumour biology.

Evidence in the literature suggests that HIF-1α quantification is commonly used to investigate the hypoxic status of spheroids [108]. As demonstrated by Riffle et al, cells within the core of larger spheroids become deprived of oxygen, resulting in an upregulation of HIF-1α to mediate the cellular response to hypoxia [108]. In my results, despite their preliminary nature, I show that HIF-1α can be detected using western blotting, highlighting the hypoxic conditions within tri-cultured heterotypic spheroids at different time points. On days 4 and 8, the faint bands suggest lower levels of HIF-1α expression compared to the more prominent bands on days 12 and 16. This is consistent with existing studies, which report increased HIF-1α expression as the spheroid size grows, correlating with greater diffusion distances and hypoxic conditions in the inner core of the spheroid [52, 108, 133]. Furthermore, the observed decrease in HIF-1α expression by day 16 could reflect the transition from hypoxia to necrosis in the spheroid core, a phase seen in larger spheroids where cell death reduces the need for hypoxic regulation [134]. The preliminary results presented here provide proof of principle, reinforcing the established role of HIF-1α as a critical marker of hypoxia in 3D tumour models. Future work, including additional western blot analyses, will further substantiate these findings and help to delineate the precise relationship between spheroid size, cell density, and HIF-1α expression. Thus, my results align closely with the current literature on the value of assessing HIF-1α to understand the hypoxic microenvironment within spheroids [135]. Overall, these findings indicate that the tri-cultured heterotypic spheroid model is capable of recapitulating the hypoxic conditions of the tumour microenvironment, which is a critical factor in tumour progression.

In addition, preliminary analysis of the angiogenic potential of the tri-cultured heterotypic spheroids was assessed by probing the western blot for VEGF-A. The expression of VEGF-A was highly present at all time points. This suggests that the tumour cell-to-fibroblast-to-EC interactions within the heterotypic spheroids are capable of promoting the upregulation of VEGF-A, which is crucial for stimulating the formation of new blood vessels to support the growing tumour [136, 137]. As A549 cells have a high angiogenic potential specifically through the secretion of VEGF-A [138]. The expression of VEGF-A is further stimulated by the co-culture of A549 cells with MRC-5s [139]. The preliminary results generated in my work are indicative of the angiogenic potential of these spheroids. However, more extensive experimentation and quantification of angiogenic markers and vessel-like structures will be necessary to fully understand the pro-angiogenic capabilities of this model.

More research is being conducted that explores the use of tri-cultured spheroids containing cancer cells, fibroblasts, and endothelial cells as a means to create a more physiologically relevant in vitro model [140, 141]. Valdoz et al. developed tri-cutlured spheroids to mimic the internal architecture of the human lung. They found that these spheroids exhibited branching and perfusable vasculature and an increase in fibronectin. Furthermore, the spheroids were cultured for an extended period of time (up to 70 days), showing the longevity of the model [140] . Whilst the spheroids cultured in my study were only cultured to a maximum of 12 days, Valdoz et al suggest that it is possible to culture tri-cultured spheroids long term. Furthermore, morphological characteristics of the spheroids reported by Valdoz suggests that a lumen like structure was formed which mimicked the alveoli lumen [140]. It is therefore possible that longer term culture of tri-cultured spheroids would allow for more *in vivo* like characteristics to develop.

4.1. Limitations

Whilst this project has provided insight into the use of a preselection method of spheroids, some limitations that should be addressed in future research. These include the lack of drug screening validation which could be used to show that the preselection method reduces variability in subsequent experiments. Future research should focus on validating the impact of using this preselection method by testing a panel of known therapeutic compounds to assess the reliability of results in drug response experiments. This was not conducted due to time limitations. Furthermore, limited molecular assessment such as the

expression of pro-angiogenic markers including VEGF and HIF-1α needs to be done more comprehensively. Whilst this project provided preliminary results, due to time constraints, a more in-depth assessment of these markers as well as additional pro-angiogenic markers like VEGF-R2 or FGF needs to be conducted to confirm the angiogenic potential of these spheroids and the impact of the preselection method on these results. Additionally, as only one experimental replicate of western blots were achieve, more robust experimentation needs to be conducted so that quantitative analysis of western blots can be conducted. Furthermore, the development of the necrotic core and cell proliferation exhibited inconsistencies across different spheroid types and time points. To better predict how various conditions impact spheroid viability, growth, and responses to therapies, future studies should investigate the time-dependent dynamics of these processes in greater detail. By addressing these limitations, it may be possible that an improved model can be established to investigate tumour angiogenesis in NSCLC

5. Conclusion

In conclusion, my work has demonstrated that by precisely controlling the cell seeding parameters (cell types, densities and ratios), it is possible to fabricate highly reproducible tumour spheroid models that can mimic key aspects of the tumour such as alterations to metabolism and a hypoxic core or necrotic core. By implementing a preselection method, with the inclusion criteria of spheroids with a circularity of 0.8 or higher, solidity of 0.4 or more and a diameter of 400 µm or higher, spheroids were kept consistent and optimised so that future research could use these spheroids for the development of a more complex model such as lung-on-a-chip or microfluidic devices. This project has therefore shown that the preselection process requires an understanding of the requirements for subsequent use. For example, spheroids will be used for dose-response assays or for hypoxia and angiogenesis research. As spheroid size and shape can contribute significantly to the outcome of both dose-response research and hypoxia research.

The preselection method established provided a means to determine the optimal cell density, growth time, and cell line combinations that would produce spheroids with consistent shape and size. These findings suggest that spheroids can serve as an effective starting point for more advanced models aimed at mimicking tumour angiogenesis. Future research should focus on further assessing the pro-angiogenic factors, such as fibroblast

growth factor, to gain deeper insights into the angiogenic potential of tri-cultured heterotypic spheroids. More molecular characteristics assessments including western blots for VEGF and HIF-1α should be conducted to confirm preliminary results shown in this project. Additionally, the application of preselected spheroids in more complex models like microfluidic devices could provide a more accurate representation of tumour angiogenesis in NSCLC.

5.1. Future Outlook

This project focused on spheroids alone and did not incorporate spheroids in a more complex model. Future research should use preselected spheroids in a more complex model such as microfluidic devices to mimic additional physiological factors such as shear stress. Further assessment of pro-angiogenic factors such as fibroblast growth factor could provide more insight into the angiogenic potential of tri-cultured heterotypic spheroids. The assessment of spheroids has provided valuable insights into spheroid dynamics and the angiogenic potential. However, future research needs to assess the use of these preselect spheroids in a more complex model like microfluidic devices. The development of a model that can incorporate heterotypic spheroids with the capacity to mimic tumour angiogenesis in NSCLC. Thus, the future use of the preselection model developed in this project can be used in the development of novel models that can mimic tumour angiogenesis in NSCLC.

Additionally, the ECM secretions of homotypic and heterotypic spheroids could be investigated to further understand the cross-talk between cancer, stromal and endothelial cells and how this can impact the angiogenic potential of spheroids for use in more complex models. Through the dissociation of spheroids and the use of fluorescence-activated cell sorting (FACs), it may be possible to better understand the cell populations within heterotypic spheroids, for example, it would be possible to establish the population of fibroblasts that are activated into CAFs. Understanding the complexity of heterotypic spheroids can then allow the expansion into more complex models. Once such a model has been established, the new complex model can be verified and tested with known therapeutics. Therefore, the aim of this project to assess the feasibility of spheroids as the basic foundation for a more complex model has allowed for the development of a preselection method that can benefit the development of future models that use spheroids.

Developing these complex models will allow for more precise research of tumour angiogenesis, enabling the testing of known therapeutics and potentially contributing to the discovery of novel treatments. By building on the foundation provided by this project, future research can advance the development of preclinical models that more accurately reflect the tumour microenvironment, ultimately improving therapeutic strategies for NSCLC.

6. References

1. National Cancer Registry Ireland (2023) Cancer in Ireland 1994-2021: Annual statistical report of the National Cancer Registry. NCRI, Cork, Ireland.
2. Molina JR, Yang P, Cassivi SD, Schild SE, Adjei AA. Non-small cell lung cancer: epidemiology, risk factors, treatment, and survivorship. Mayo Clin Proc. 2008;83(5):584-94.
3. Miller KD, Nogueira L, Devasia T, Mariotto AB, Yabroff KR, Jemal A, et al. Cancer treatment and survivorship statistics, 2022. CA: a cancer journal for clinicians. 2022;72(5):409-36.
4. Wilkerson MD, Yin X, Walter V, Zhao N, Cabanski CR, Hayward MC, et al. Differential pathogenesis of lung adenocarcinoma subtypes involving sequence mutations, copy number, chromosomal instability, and methylation. PloS one. 2012;7(5):e36530.
5. Chen Z, Fillmore CM, Hammerman PS, Kim CF, Wong K-K. Non-small-cell lung cancers: a heterogeneous set of diseases. Nature Reviews Cancer. 2014;14(8):535-46.
6. Xie S, Wu Z, Qi Y, Wu B, Zhu X. The metastasizing mechanisms of lung cancer: Recent advances and therapeutic challenges. Biomedicine & Pharmacotherapy. 2021;138:111450.
7. Ngaha TYS, Zhilenkova AV, Essogmo FE, Uchendu IK, Abah MO, Fossa LT, et al. Angiogenesis in Lung Cancer: Understanding the Roles of Growth Factors. Cancers. 2023;15(18):4648.
8. DiMasi JA, Feldman L, Seckler A, Wilson A. Trends in risks associated with new drug development: success rates for investigational drugs. Clinical Pharmacology & Therapeutics. 2010;87(3):272-7.
9. Altorki NK, Markowitz GJ, Gao D, Port JL, Saxena A, Stiles B, et al. The lung microenvironment: an important regulator of tumour growth and metastasis. Nature Reviews Cancer. 2019;19(1):9-31.
10. Zhang Y, Bian Y, Wang Y, Wang Y, Duan X, Han Y, et al. HIF-1α is necessary for activation and tumour-promotion effect of cancer-associated fibroblasts in lung cancer. J Cell Mol Med. 2021;25(12):5457-69.
11. Cheng YQ, Wang SB, Liu JH, Jin L, Liu Y, Li CY, et al. Modifying the tumour microenvironment and reverting tumour cells: New strategies for treating malignant tumours. Cell proliferation. 2020;53(8):e12865.
12. Suzuki J, Tsuboi M, Ishii G. Cancer-associated fibroblasts and the tumor microenvironment in non-small cell lung cancer. Expert Review of Anticancer Therapy. 2022;22(2):169-82.
13. Mehta G, Hsiao AY, Ingram M, Luker GD, Takayama S. Opportunities and challenges for use of tumor spheroids as models to test drug delivery and efficacy. Journal of Controlled Release. 2012;164(2):192-204.
14. Hofer M, Lutolf MP. Engineering organoids. Nature Reviews Materials. 2021;6(5):402-20.
15. Zanoni M, Piccinini F, Arienti C, Zamagni A, Santi S, Polico R, et al. 3D tumor spheroid models for in vitro therapeutic screening: a systematic approach to enhance the biological relevance of data obtained. Scientific Reports. 2016;6(1):19103.
16. Achilli TM, Meyer J, Morgan JR. Advances in the formation, use and understanding of multi-cellular spheroids. Expert Opin Biol Ther. 2012;12(10):1347-60.
17. Guex AG, Di Marzio N, Eglin D, Alini M, Serra T. The waves that make the pattern: a review on acoustic manipulation in biomedical research. Materials Today Bio. 2021;10:100110.

18. Caliari SR, Burdick JA. A practical guide to hydrogels for cell culture. Nature methods. 2016;13(5):405-14.
19. Bray LJ, Werner C. Evaluation of three-dimensional in vitro models to study tumor angiogenesis. ACS Biomaterials Science & Engineering. 2018;4(2):337-46.
20. Baghban R, Roshangar L, Jahanban-Esfahlan R, Seidi K, Ebrahimi-Kalan A, Jaymand M, et al. Tumor microenvironment complexity and therapeutic implications at a glance. Cell Communication and Signaling. 2020;18(1):59.
21. Costard LS, Hosn RR, Ramanayake H, O'Briena FJ, Curtin CM. Influences of the 3D microenvironment on cancer cell behaviour and treatment responsiveness: a recent update on lung, breast and prostate cancer models. Acta Biomaterialia. 2021.
22. Ayuso JM, Virumbrales-Muñoz M, Lacueva A, Lanuza PM, Checa-Chavarria E, Botella P, et al. Development and characterization of a microfluidic model of the tumour microenvironment. Sci Rep. 2016;6:36086.
23. Bazou D, Maimon N, Gruionu G, Grahovac J, Seano G, Liu H, et al. Vascular beds maintain pancreatic tumour explants for ex vivo drug screening. Journal of tissue engineering and regenerative medicine. 2018;12(1):e318-e22.
24. Bazou D, Ng MR, Song JW, Chin SM, Maimon N, Munn LL. Flow-induced HDAC1 phosphorylation and nuclear export in angiogenic sprouting. Scientific reports. 2016;6(1):34046.
25. Blache U, Ehrbar M. Inspired by nature: hydrogels as versatile tools for vascular engineering. Advances in wound care. 2018;7(7):232-46.
26. Taubenberger AV, Bray LJ, Haller B, Shaposhnykov A, Binner M, Freudenberg U, et al. 3D extracellular matrix interactions modulate tumour cell growth, invasion and angiogenesis in engineered tumour microenvironments. Acta Biomaterialia. 2016;36:73-85.
27. Ziółkowska-Suchanek I. Mimicking Tumor Hypoxia in Non-Small Cell Lung Cancer Employing Three-Dimensional In Vitro Models. Cells. 2021;10(1):141.
28. El Harane S, Zidi B, El Harane N, Krause K-H, Matthes T, Preynat-Seauve O. Cancer Spheroids and Organoids as Novel Tools for Research and Therapy: State of the Art and Challenges to Guide Precision Medicine. Cells. 2023;12(7):1001.
29. Shamir ER, Ewald AJ. Three-dimensional organotypic culture: experimental models of mammalian biology and disease. Nature reviews Molecular cell biology. 2014;15(10):647-64.
30. Sen C, Freund D, Gomperts BN. Three-dimensional models of the lung: past, present and future: a mini review. Biochemical Society Transactions. 2022;50(2):1045-56.
31. Hanahan D, Weinberg RA. Hallmarks of cancer: the next generation. cell. 2011;144(5):646-74.
32. Baker BM, Chen CS. Deconstructing the third dimension–how 3D culture microenvironments alter cellular cues. Journal of cell science. 2012;125(13):3015-24.
33. Fennema E, Rivron N, Rouwkema J, van Blitterswijk C, De Boer J. Spheroid culture as a tool for creating 3D complex tissues. Trends in biotechnology. 2013;31(2):108-15.
34. Saibene M, Serchi T, Bonfanti P, Colombo A, Nelissen I, Halder R, et al. The use of a complex tetra-culture alveolar model to study the biological effects induced by gold nanoparticles with different physicochemical properties. Environmental Toxicology and Pharmacology. 2024;106:104353.
35. Amann A, Zwierzina M, Gamerith G, Bitsche M, Huber JM, Vogel GF, et al. Development of an innovative 3D cell culture system to study tumour-stroma interactions in non-small cell lung cancer cells. PloS one. 2014;9(3):e92511.

36. Korff T, Augustin HG. Integration of endothelial cells in multicellular spheroids prevents apoptosis and induces differentiation. The Journal of cell biology. 1998;143(5):1341-52.
37. Arakelian L, Lion J, Churlaud G, Bargui R, Thierry B, Mutabazi E, et al. Endothelial CD34 expression and regulation of immune cell response in-vitro. Scientific Reports. 2023;13(1):13512.
38. Siemerink MJ, Klaassen I, Vogels IM, Griffioen AW, Van Noorden CJ, Schlingemann RO. CD34 marks angiogenic tip cells in human vascular endothelial cell cultures. Angiogenesis. 2012;15:151-63.
39. Aguilar Cosme JR, Gagui DC, Bryant HE, Claeyssens F. Morphological response in cancer spheroids for screening photodynamic therapy parameters. Frontiers in molecular biosciences. 2021;8:784962.
40. Kim S, Lam PY, Jayaraman A, Han A. Uniform sized cancer spheroids production using hydrogel-based droplet microfluidics: a review. Biomedical Microdevices. 2024;26(2):26.
41. Abolhassani H, Zaer M, Shojaosadati SA, Hashemi-Najafabadi S. Rapid generation of homogenous tumor spheroid microtissues in a scaffold-free platform for high-throughput screening of a novel combination nanomedicine. PLoS One. 2023;18(2):e0282064.
42. Lee J, Kim Y, Lim J, Jung H-I, Castellani G, Piccinini F, et al. Optimization of Tumor Spheroid Preparation and Morphological Analysis for Drug Evaluation. BioChip Journal. 2024;18(1):160-9.
43. Stroock AD, Fischbach C. Microfluidic Culture Models of Tumor Angiogenesis. Tissue Engineering Part A. 2010;16(7):2143-6.
44. Khaitan D, Chandna S, Arya MB, Dwarakanath BS. Establishment and characterization of multicellular spheroids from a human glioma cell line; Implications for tumor therapy. J Transl Med. 2006;4:12.
45. Jensen C, Teng Y. Is it time to start transitioning from 2D to 3D cell culture? Frontiers in molecular biosciences. 2020;7:33.
46. Asghar W, El Assal R, Shafiee H, Pitteri S, Paulmurugan R, Demirci U. Engineering cancer microenvironments for in vitro 3-D tumor models. Materials Today. 2015;18(10):539-53.
47. Vörsmann H, Groeber F, Walles H, Busch S, Beissert S, Walczak H, et al. Development of a human three-dimensional organotypic skin-melanoma spheroid model for in vitro drug testing. Cell Death & Disease. 2013;4(7):e719-e.
48. Bhat SM, Badiger VA, Vasishta S, Chakraborty J, Prasad S, Ghosh S, et al. 3D tumor angiogenesis models: recent advances and challenges. Journal of Cancer Research and Clinical Oncology. 2021;147(12):3477-94.
49. Liu X-q, Kiefl R, Roskopf C, Tian F, Huber RM. Interactions among lung cancer cells, fibroblasts, and macrophages in 3D co-cultures and the impact on MMP-1 and VEGF expression. PLoS One. 2016;11(5):e0156268.
50. Movia D, Bazou D, Prina-Mello A. ALI multilayered co-cultures mimic biochemical mechanisms of the cancer cell-fibroblast cross-talk involved in NSCLC MultiDrug Resistance. BMC Cancer. 2019;19(1):854.
51. Shen H, Yu X, Yang F, Zhang Z, Shen J, Sun J, et al. Reprogramming of normal fibroblasts into cancer-associated fibroblasts by miRNAs-mediated CCL2/VEGFA signaling. PLoS genetics. 2016;12(8):e1006244.
52. Carmeliet P, Jain RK. Angiogenesis in cancer and other diseases. Nature. 2000;407(6801):249-57.

53. Sophia F, Caroline L, Ting-Yu C. Angiogenesis and Its Role in the Tumour Microenvironment: A Target for Cancer Therapy. In: Mirjana R, Eva S, editors. Current Cancer Treatment. Rijeka: IntechOpen; 2020. p. Ch. 2.
54. Bergers G, Benjamin LE. Tumorigenesis and the angiogenic switch. Nature reviews Cancer. 2003;3(6):401-10.
55. Vallon M, Chang J, Zhang H, Kuo CJ. Developmental and pathological angiogenesis in the central nervous system. Cell Mol Life Sci. 2014;71(18):3489-506.
56. Folkman J, editor Role of angiogenesis in tumor growth and metastasis. Seminars in oncology; 2002: Elsevier.
57. Ziyad S, Iruela-Arispe ML. Molecular mechanisms of tumor angiogenesis. Genes & cancer. 2011;2(12):1085-96.
58. Karamysheva A. Mechanisms of angiogenesis. Biochemistry (Moscow). 2008;73:751-62.
59. Xiong Y-Q, Sun H-C, Zhang W, Zhu X-D, Zhuang P-Y, Zhang J-B, et al. Human hepatocellular carcinoma tumor–derived endothelial cells manifest increased angiogenesis capability and drug resistance compared with normal endothelial cells. Clinical Cancer Research. 2009;15(15):4838-46.
60. Hida K, Hida Y, Amin DN, Flint AF, Panigrahy D, Morton CC, et al. Tumor-associated endothelial cells with cytogenetic abnormalities. Cancer research. 2004;64(22):8249-55.
61. Craft PS, Harris AL. Clinical prognostic significance of tumour angiogenesis. Ann Oncol. 1994;5(4):305-11.
62. Wu S, Zhou C, King JA, Stevens T. A unique pulmonary microvascular endothelial cell niche revealed by Weibel-Palade bodies and Griffonia simplicifolia. Pulm Circ. 2014;4(1):110-5.
63. Zhang G, Li M, Zhou D, Yang X, Zhang W, Gao R. Loss of endothelial EMCN drives tumor lung metastasis through the premetastatic niche. Journal of Translational Medicine. 2022;20(1):446.
64. Tsuchiya T, Doi R, Obata T, Hatachi G, Nagayasu T. Lung microvascular niche, repair, and engineering. Frontiers in Bioengineering and Biotechnology. 2020;8:105.
65. Kahn BM, Lucas A, Alur RG, Wengyn MD, Schwartz GW, Li J, et al. The vascular landscape of human cancer. The Journal of Clinical Investigation. 2021;131(2).
66. Stevens T, Phan S, Frid MG, Alvarez D, Herzog E, Stenmark KR. Lung vascular cell heterogeneity: endothelium, smooth muscle, and fibroblasts. Proc Am Thorac Soc. 2008;5(7):783-91.
67. Macchiarini P, Fontanini G, Squartini F, Angeletti C, Hardin M. Relation of neovascularisation to metastasis of non-small-cell lung cancer. The Lancet. 1992;340(8812):145-6.
68. Pang RW, Poon RT. Clinical implications of angiogenesis in cancers. Vasc Health Risk Manag. 2006;2(2):97-108.
69. Zachary I. VEGF signalling: integration and multi-tasking in endothelial cell biology. Biochemical Society Transactions. 2003;31(6):1171-7.
70. Graves EE, Maity A, Le QT. The tumor microenvironment in non-small-cell lung cancer. Semin Radiat Oncol. 2010;20(3):156-63.
71. Papetti M, Herman IM. Mechanisms of normal and tumor-derived angiogenesis. American Journal of Physiology-Cell Physiology. 2002;282(5):C947-C70.
72. Goel S, Duda DG, Xu L, Munn LL, Boucher Y, Fukumura D, et al. Normalization of the vasculature for treatment of cancer and other diseases. Physiological reviews. 2011;91(3):1071-121.

73. Viallard C, Larrivée B. Tumor angiogenesis and vascular normalization: alternative therapeutic targets. Angiogenesis. 2017;20(4):409-26.
74. Eldridge L, Wagner EM. Angiogenesis in the lung. J Physiol. 2019;597(4):1023-32.
75. Eldridge L, Moldobaeva A, Zhong Q, Jenkins J, Snyder M, Brown RH, et al. Bronchial artery angiogenesis drives lung tumor growth. Cancer research. 2016;76(20):5962-9.
76. Guo X-b, Chen X-j, Tong L-j, Peng X, Huang M, Liu H-c, et al. DCLAK11, a multi-tyrosine kinase inhibitor, exhibits potent antitumor and antiangiogenic activity in vitro. Acta Pharmacologica Sinica. 2015;36(10):1266-76.
77. Gomes DA, Joubert AM, Visagie MH. The Biological Relevance of Papaverine in Cancer Cells. Cells. 2022;11(21):3385.
78. Han Y, Kuang S-Z, Gomer A, Ramirez-Bergeron DL. Hypoxia Influences the Vascular Expansion and Differentiation of Embryonic Stem Cell Cultures Through the Temporal Expression of Vascular Endothelial Growth Factor Receptors in an ARNT-Dependent Manner. Stem Cells. 2010;28(4):799-809.
79. Zuchowska A, Jastrzebska E, Zukowski K, Chudy M, Dybko A, Brzozka Z. A549 and MRC-5 cell aggregation in a microfluidic Lab-on-a-chip system. Biomicrofluidics. 2017;11(2):024110.
80. Nicosia RF, Bonanno E, Smith M. Fibronectin promotes the elongation of microvessels during angiogenesis in vitro. Journal of cellular physiology. 1993;154(3):654-61.
81. Nishikiori N, Takada K, Sato T, Miyamoto S, Watanabe M, Hirakawa Y, et al. Physical Properties and Cellular Metabolic Characteristics of 3D Spheroids Are Possible Definitive Indices for the Biological Nature of Cancer-Associated Fibroblasts. Cells. 2023;12(17):2160.
82. Song JW, Bazou D, Munn LL. Microfluidic model of angiogenic sprouting. Vascular Morphogenesis: Springer; 2015. p. 243-54.
83. Ro J, Kim J, Cho Y-K. Recent advances in spheroid-based microfluidic models to mimic tumour microenvironment. Analyst. 2022.
84. Tevlek A, Kecili S, Ozcelik OS, Kulah H, Tekin HC. Spheroid Engineering in Microfluidic Devices. ACS Omega. 2023;8(4):3630-49.
85. Tutty MA, Vella G, Prina-Mello A. Pre-clinical 2D and 3D toxicity response to a panel of nanomaterials; comparative assessment of NBM-induced liver toxicity. Drug Delivery and Translational Research. 2022;12(9):2157-77.
86. MOVIA D, PRINA MELLO A. Nanotoxicity in cancer research: technical protocols and tips considerations for the use of 3D tumour spheroids. InTech; 2018.
87. Saleh F, Harb A, Soudani N, Zaraket H. A three-dimensional A549 cell culture model to study respiratory syncytial virus infections. Journal of Infection and Public Health. 2020;13(8):1142-7.
88. Mandavilli BS, Aggeler RJ, Chambers KM. Tools to measure cell health and cytotoxicity using high content imaging and analysis. High Content Screening: A Powerful Approach to Systems Cell Biology and Phenotypic Drug Discovery. 2018:33-46.
89. Staedler D, Passemard S, Magouroux T, Rogov A, Maguire CM, Mohamed BM, et al. Cellular uptake and biocompatibility of bismuth ferrite harmonic advanced nanoparticles. Nanomedicine: Nanotechnology, Biology and Medicine. 2015;11(4):815-24.
90. Tutty MA, Prina-Mello A. A Method for the In Vitro Cytotoxicity Assessment of Anti-cancer Compounds and Materials Using High Content Screening Analysis. Cancer Cell Culture: Methods and Protocols: Springer; 2023. p. 241-9.
91. Piccinini F, Peirsman A, Stellato M, Pyun J-C, Tumedei MM, Tazzari M, et al. Deep learning-based tool for morphotypic analysis of 3D multicellular spheroids. Journal of Mechanics in Medicine and Biology. 2023;23(06):2340034.

92. Yang X. 3D Microtumours fabricated by microfluidics: applications in ovarian cancer: University of Oxford; 2023.
93. Rozenberg JM, Filkov GI, Trofimenko AV, Karpulevich EA, Parshin VD, Royuk VV, et al. Biomedical applications of non-small cell lung cancer spheroids. Frontiers in Oncology. 2021;11:791069.
94. Vickerman V, Blundo J, Chung S, Kamm R. Design, fabrication and implementation of a novel multi-parameter control microfluidic platform for three-dimensional cell culture and real-time imaging. Lab on a Chip. 2008;8(9):1468-77.
95. Lee S-J, Nowicki M, Harris B, Zhang LG. Fabrication of a highly aligned neural scaffold via a table top stereolithography 3D printing and electrospinning. Tissue Engineering Part A. 2017;23(11-12):491-502.
96. Fang Y, Eglen RM. Three-dimensional cell cultures in drug discovery and development. Slas discovery: Advancing Life Sciences R&D. 2017;22(5):456-72.
97. Cox G, Jones JL, Walker RA, Steward WP, O'Byrne KJ. Angiogenesis and non-small cell lung cancer. Lung Cancer. 2000;27(2):81-100.
98. Daum S, Hagen H, Naismith E, Wolf D, Pircher A. The role of anti-angiogenesis in the treatment landscape of non-small cell lung cancer–new combinational approaches and strategies of neovessel inhibition. Frontiers in Cell and Developmental Biology. 2021;8:610903.
99. Kowanetz M, Ferrara N. Vascular endothelial growth factor signaling pathways: therapeutic perspective. Clinical Cancer Research. 2006;12(17):5018-22.
100. Verjans ET, Doijen J, Luyten W, Landuyt B, Schoofs L. Three-dimensional cell culture models for anticancer drug screening: Worth the effort? Journal of cellular physiology. 2018;233(4):2993-3003.
101. Gunay G, Kirit HA, Kamatar A, Baghdasaryan O, Hamsici S, Acar H. The effects of size and shape of the ovarian cancer spheroids on the drug resistance and migration. Gynecologic Oncology. 2020;159(2):563-72.
102. Barrera-Rodríguez R, Fuentes JM. Multidrug resistance characterization in multicellular tumour spheroids from two human lung cancer cell lines. Cancer Cell International. 2015;15(1):47.
103. Qi X, Prokhorova AV, Mezentsev AV, Shen N, Trofimenko AV, Filkov GI, et al. Comparison of EMT-Related and Multi-Drug Resistant Gene Expression, Extracellular Matrix Production, and Drug Sensitivity in NSCLC Spheroids Generated by Scaffold-Free and Scaffold-Based Methods. International Journal of Molecular Sciences. 2022;23(21):13306.
104. Hulo P, Deshayes S, Fresquet J, Chéné A-L, Blandin S, Boisgerault N, et al. Use of non-small cell lung cancer multicellular tumor spheroids to study the impact of chemotherapy. Respiratory Research. 2024;25(1):156.
105. Zanoni M, Pignatta S, Arienti C, Bonafè M, Tesei A. Anticancer drug discovery using multicellular tumor spheroid models. Expert opinion on drug discovery. 2019;14(3):289-301.
106. Senrung A, Lalwani S, Janjua D, Tripathi T, Kaur J, Ghuratia N, et al. 3D tumor spheroids: morphological alterations a yardstick to anti-cancer drug response. In vitro models. 2023;2(6):219-48.
107. Hirschhaeuser F, Menne H, Dittfeld C, West J, Mueller-Klieser W, Kunz-Schughart LA. Multicellular tumor spheroids: An underestimated tool is catching up again. Journal of Biotechnology. 2010;148(1):3-15.
108. Riffle S, Pandey RN, Albert M, Hegde RS. Linking hypoxia, DNA damage and proliferation in multicellular tumor spheroids. Bmc Cancer. 2017;17:1-12.

109. Kai F, Drain AP, Weaver VM. The extracellular matrix modulates the metastatic journey. Dev Cell. 2019;49(3):332-46.
110. Vakhshiteh F, Bagheri Z, Soleimani M, Ahvaraki A, Pournemat P, Alavi SE, et al. Heterotypic tumor spheroids: a platform for nanomedicine evaluation. Journal of Nanobiotechnology. 2023;21(1):249.
111. Białkowska K, Komorowski P, Bryszewska M, Miłowska K. Spheroids as a Type of Three-Dimensional Cell Cultures—Examples of Methods of Preparation and the Most Important Application. International Journal of Molecular Sciences. 2020;21(17):6225.
112. Vicent S, Sayles LC, Vaka D, Khatri P, Gevaert O, Chen R, et al. Cross-species functional analysis of cancer-associated fibroblasts identifies a critical role for Clcf1 and Il-6 in non–small cell lung cancer in vivo. Cancer research. 2012;72(22):5744-56.
113. Mei Y, Lakotsenina E, Wegner M, Hehne T, Krause D, Hakimeh D, et al. Three-Dimensional-Bioprinted Non-Small Cell Lung Cancer Models in a Mouse Phantom for Radiotherapy Research. International Journal of Molecular Sciences. 2024;25(19):10268.
114. Sutherland RM, McCredie JA, Inch WR. Growth of multicell spheroids in tissue culture as a model of nodular carcinomas. Journal of the National Cancer Institute. 1971;46(1):113-20.
115. Nath S, Devi GR. Three-dimensional culture systems in cancer research: Focus on tumor spheroid model. Pharmacol Ther. 2016;163:94-108.
116. Costa EC, Moreira AF, de Melo-Diogo D, Gaspar VM, Carvalho MP, Correia IJ. 3D tumor spheroids: an overview on the tools and techniques used for their analysis. Biotechnology advances. 2016;34(8):1427-41.
117. Zhang K, Wang Y, Xue J, Liang N, Wei Z. Real-time monitoring ATP variation in human cancer organoids for a long term by DNA-based nanosensor. Analytica Chimica Acta. 2023;1275:341608.
118. Warburg O. On the origin of cancer cells. Science. 1956;123(3191):309-14.
119. Tartagni O, Borók A, Mensà E, Bonyár A, Monti B, Hofkens J, et al. Microstructured soft devices for the growth and analysis of populations of homogenous multicellular tumor spheroids. Cellular and Molecular Life Sciences. 2023;80(4):93.
120. Hamilton G. Multicellular spheroids as an in vitro tumor model. Cancer Letters. 1998;131(1):29-34.
121. Duval K, Grover H, Han L-H, Mou Y, Pegoraro AF, Fredberg J, et al. Modeling physiological events in 2D vs. 3D cell culture. Physiology. 2017;32(4):266-77.
122. Fischbach C, Chen R, Matsumoto T, Schmelzle T, Brugge JS, Polverini PJ, et al. Engineering tumors with 3D scaffolds. Nature methods. 2007;4(10):855-60.
123. Farah IO, Lewis VL, Ayensu WK, Cameron JA. Therapeutic implications of the Warburg effect: assessing the survival of MRC-5 and A549 cell lines upon exposure to honey and D-glucose. Biomed Sci Instru. 2013;49:101-8.
124. Vander Heiden MG, Cantley LC, Thompson CB. Understanding the Warburg effect: the metabolic requirements of cell proliferation. science. 2009;324(5930):1029-33.
125. Scholzen T, Gerdes J. The Ki-67 protein: from the known and the unknown. Journal of cellular physiology. 2000;182(3):311-22.
126. Kalluri R. The biology and function of fibroblasts in cancer. Nature Reviews Cancer. 2016;16(9):582-98.
127. Öhlund D, Elyada E, Tuveson D. Fibroblast heterogeneity in the cancer wound. Journal of Experimental Medicine. 2014;211(8):1503-23.
128. DeLisser HM, Christofidou-Solomidou M, Strieter RM, Burdick MD, Robinson CS, Wexler RS, et al. Involvement of endothelial PECAM-1/CD31 in angiogenesis. The American journal of pathology. 1997;151(3):671.

129. Donovan D, Brown N, Bishop E, Lewis C. Comparison of three in vitro human 'angiogenesis' assays with capillaries formed in vivo. Angiogenesis. 2001;4:113-21.
130. Lamichhane SP, Arya N, Kohler E, Xiang S, Christensen J, Shastri VP. Recapitulating epithelial tumor microenvironment in vitro using three dimensional tri-culture of human epithelial, endothelial, and mesenchymal cells. BMC Cancer. 2016;16:581.
131. Muz B, De La Puente P, Azab F, Kareem Azab A. The role of hypoxia in cancer progression, angiogenesis, metastasis, and resistance to therapy. Hypoxia. 2015:83-92.
132. Friedrich J, Seidel C, Ebner R, Kunz-Schughart LA. Spheroid-based drug screen: considerations and practical approach. Nature Protocols. 2009;4(3):309-24.
133. Arora L, Patra D, Roy S, Nanda S, Singh N, Verma AK, et al. Hypoxia-induced miR-210-3p expression in lung adenocarcinoma potentiates tumor development by regulating CCL2 mediated monocyte infiltration. Molecular Oncology. 2024;18(5):1278-300.
134. Guillotin B, Bareille R, Bourget C, Bordenave L, Amédée J. Interaction between human umbilical vein endothelial cells and human osteoprogenitors triggers pleiotropic effect that may support osteoblastic function. Bone. 2008;42(6):1080-91.
135. Nishikiori N, Takada K, Sato T, Miyamoto S, Watanabe M, Hirakawa Y, et al. Physical properties and cellular metabolic characteristics of 3D spheroids are possible definitive indices for the biological nature of cancer-associated fibroblasts. Cells. 2023;12(17):2160.
136. Roy M, Alix C, Bouakaz A, Serrière S, Escoffre J-M. Tumor Spheroids as Model to Design Acoustically Mediated Drug Therapies: A Review. Pharmaceutics. 2023;15(3):806.
137. Mokhames Z, Rezaie Z, Ardeshirylajimi A, Basiri A, Taheri M, Omrani MD. VEGF-incorporated PVDF/collagen nanofibrous scaffold for bladder wall regeneration and angiogenesis. International Journal of Polymeric Materials and Polymeric Biomaterials. 2021;70(8):521-9.
138. Liu W, Xu J, Wang M, Wang Q, Bi Y, Han M. Tumor-derived vascular endothelial growth factor (VEGF)-a facilitates tumor metastasis through the VEGF-VEGFR1 signaling pathway. International journal of oncology. 2011;39(5):1213-20.
139. Ziółkowska-Suchanek I. Mimicking Tumor Hypoxia in Non-Small Cell Lung Cancer Employing Three-Dimensional In Vitro Models. Cells 2021, 10, 141. s Note: MDPI stays neu-tral with regard to jurisdictional clai-ms in …; 2021.
140. Valdoz JC, Franks NA, Cribbs CG, Jacobs DJ, Dodson EL, Knight CJ, et al. Vascular lung triculture organoid via soluble extracellular matrix suspension.
141. Lamichhane SP, Arya N, Kohler E, Xiang S, Christensen J, Shastri VP. Recapitulating epithelial tumor microenvironment in vitro using three dimensional tri-culture of human epithelial, endothelial, and mesenchymal cells. BMC Cancer. 2016;16(1):581.

Appendix I – Methodology used to generate multivariate graphs.

Briefly data in excel format was imported into MATLAB and retitled e.g. A549 spheroid data. The following syntax was then input into the command window to generate the graph:

The following syntax was then input into the command window to generate the graph:

```
feretsX = A549 spheroid data.FeretsXDiameter;
feretsY = A549 spheroid data.FeretsYDiameter;
time = A549 spheroid data.Time;
viability = A549 spheroid data.Viability;

% Set a constant size for all points
pointSize = 2000;

% Create a scatter plot with constant size and variable color
figure;
scatter3(feretsX, feretsY, time, pointSize, viability, 'filled');
xlabel('Feret''s X Diameter');
ylabel('Feret''s Y Diameter');
zlabel('Time');
colormap(cool);
colorbar;
title('Multivariate Plot of Feret''s X and Y Diameter, Time, and Viability');
```

Appendix II – Flow cytometry gating

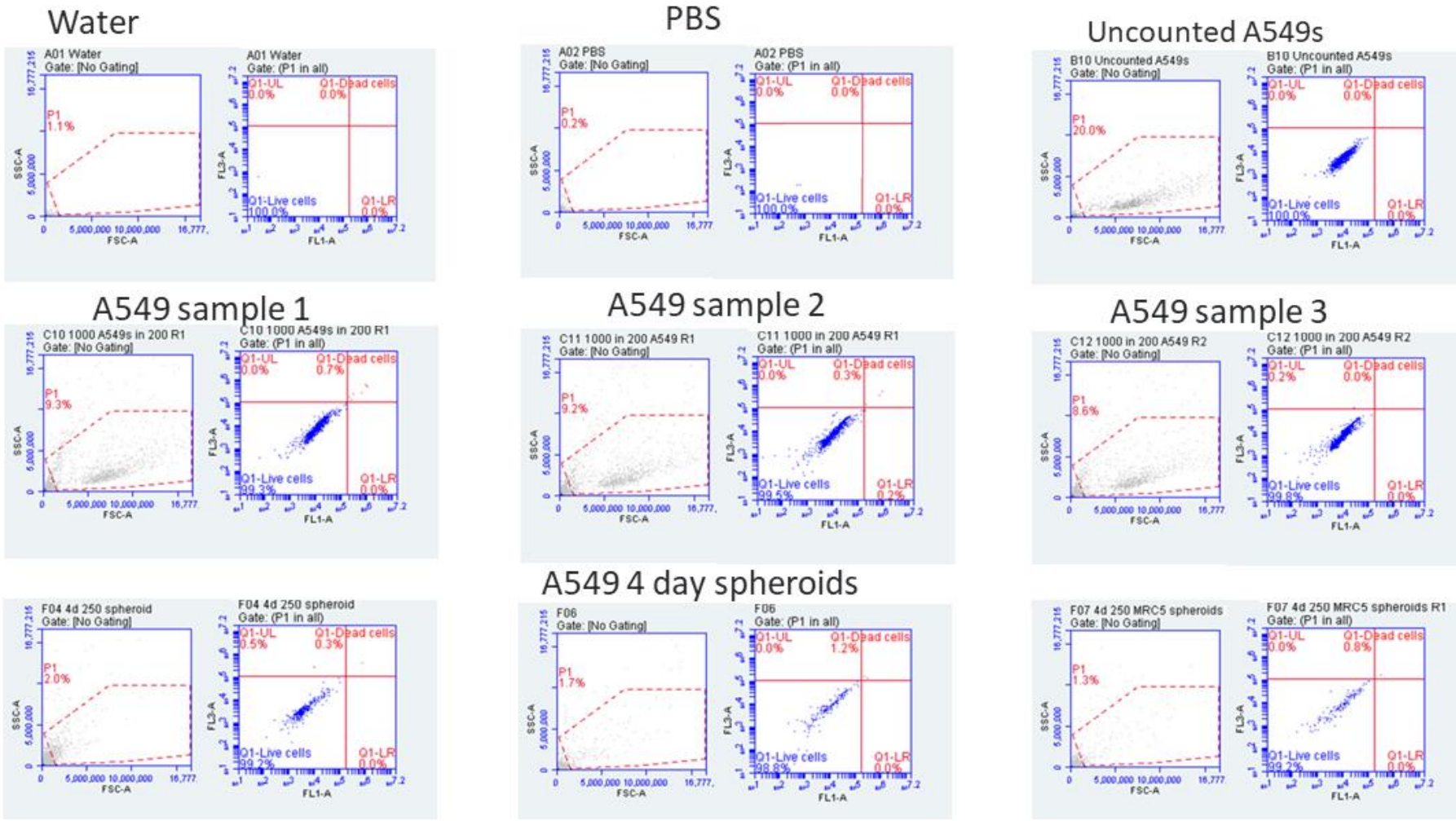

Figure II.1: Flow cytometry sample gating. Images of flow cytometry plots illustrating gating used for the analysis of 5000 A549 cell populations of initially seeded cells and of 4 day old spheroids.

Appendix III -Confirmation of spheroid dissociation using brightfield imaging of haemocytometers:

Spheroids were dissociated using the methodology described in section 2.3.1 To confirm dissociation into single cells, 10 µL of the cell suspension was inserted into a haemocytometer and images captured on the EVOS M5000 Imaging System Microscope (figure III.1).

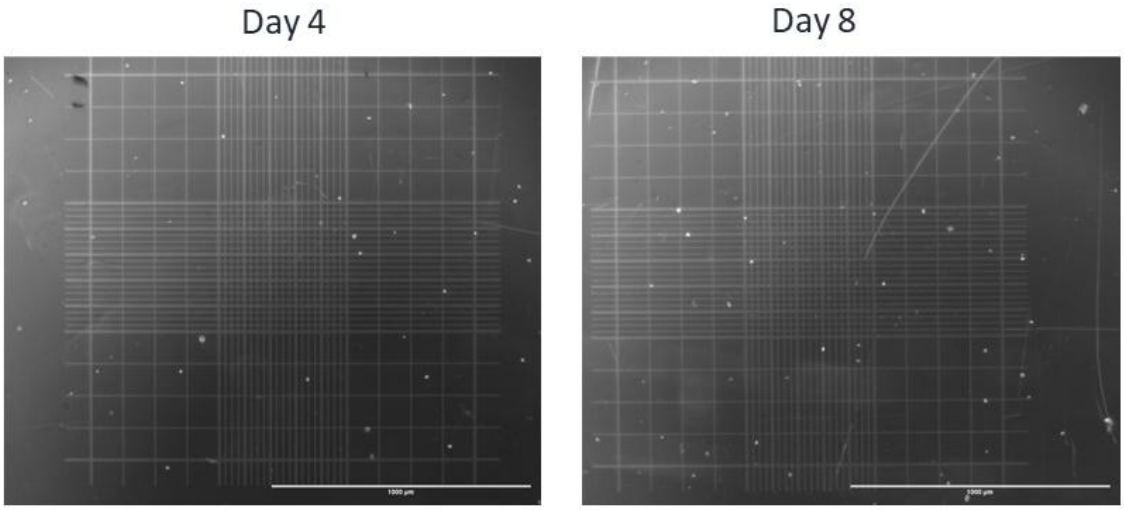

Figure III.1: Representative brightfield image showing the dissociation of a spheroid into single cells captured on an EVOS M5000 Imaging System Microscope.

Appendix IV – Gel preparation for western blot

Gel preparation.

Prepared proteins were loaded into hand cast gels according to the following protocol. The gel casting apparatus (mini-PROTEAN Tetra System (Bio-Rad, UK)) was assembled with the glass spacer plate pressed to a short plate and clamped onto the casting stand, both glass plates were cleaned with isopropanol prior to assembly. The glass plates were then checked for leaks by using a Pasteur pipette to inject isopropanol between the plates. If leaks were present the casting equipment was reassembled ensuring plates were clamped tightly together. The isopropanol was then poured out and plates left to dry before adding gel solutions. The resolving gel was prepared first in a 50 mL falcon tube. Resolving gel percentage was cast depending on the protein of interest as follows:

Table IV.1: Low molecular weight proteins need a higher gel %

Protein Size (kDa)	Gel Percentage (%)
4-40	15
12-45	15
10-70	12
15-100	10
25-200	7.5
>200	5

Table IV.2: Reagents and quantities used to make specific percentages of resolving gel for western blots

Component	6%	7.5%	10%	12%	15%	20%
H_2O	8.13 mL	7.4 mL	6.07 mL	5.2 mL	3.75 mL	1.1 mL
1.5 M Tris pH 8.8	3.75 mL	3.75 mL	3.75 mL	3.75 mL	3.75 mL	3.75 mL
Acrylamide	2.92 mL	3.65 mL	4.95 mL	5.8 mL	7.25 mL	10 mL
10% SDS	150 µL	150 µL	150 µL	150 µL	150 µL	150 µL
10% APS	75 µL	75 µL	75 µL	75 µL	75 µL	75 µL
TEMED	18 µL	18 µL	18 µL	18 µL	18 µL	18 µL

TEMED was added last, and the gel solution gently mixed before being pipetted between the plates with a Pasteur pipette, allowing a 1/1.5 cm gap from the top of the short plate to allow space for the stacking gel. Isopropanol was then pipetted above the resolving gel to ensure an even gel to form. Excess resolving gel was left in the 50 mL tube to view polymerisation. Once the excess resolving gel had polymerised (20-30 min), the isopropanol was poured off and the stacking gel was prepared in a new 50 mL falcon tube as follows.

Table IV.3: reagents and quantities used to the stacking gel for western blots.

Component	Amount
H_2O	6.1 mL
0.5 M Tris Ph 6.8	2.5 mL

Acrylamide	1.3 mL
10% SDS	100 µL
10% APS	100 µL
TEMED	20 µL

As with the resolving gel, TEMED was added last, and the gel solution mixed before being pipetted between the plates above the resolving gel with a Pasteur pipette to the top of the short plate. A 10-well comb was then pushed between the plates, ensuring no bubbles were underneath the wells. Excess stacking gel was left in the 50 mL tube to view polymerisation. Once the excess stacking gel had polymerised (10-15 min), the plates were removed from the casting apparatus and soaked in 1x running buffer and stored in the fridge overnight.

Appendix V – Additional spheroid images

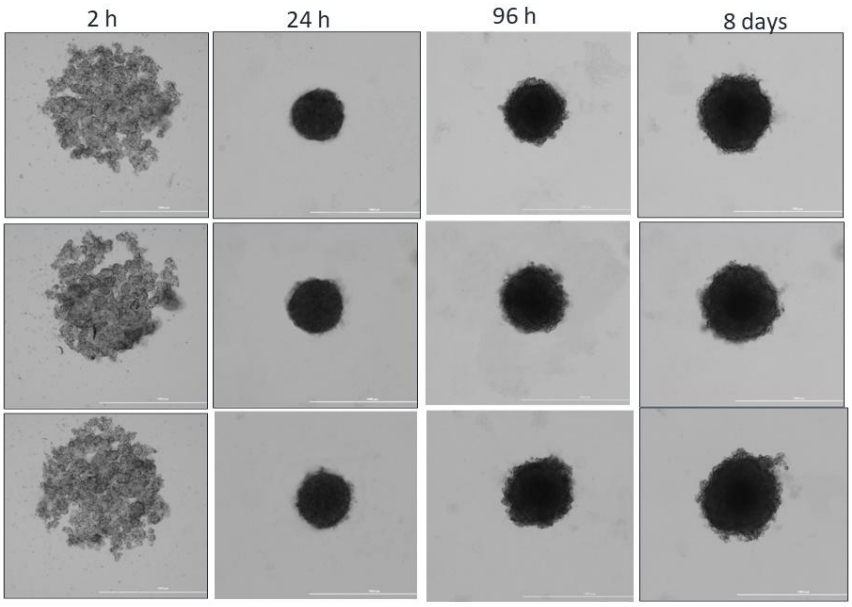

Figure V.1: Additional images of A549 - MRC-5 spheroids with a ratio of 1:1 to show consistency in the production of spheroids.

Appendix VI – Standard curve for BCA

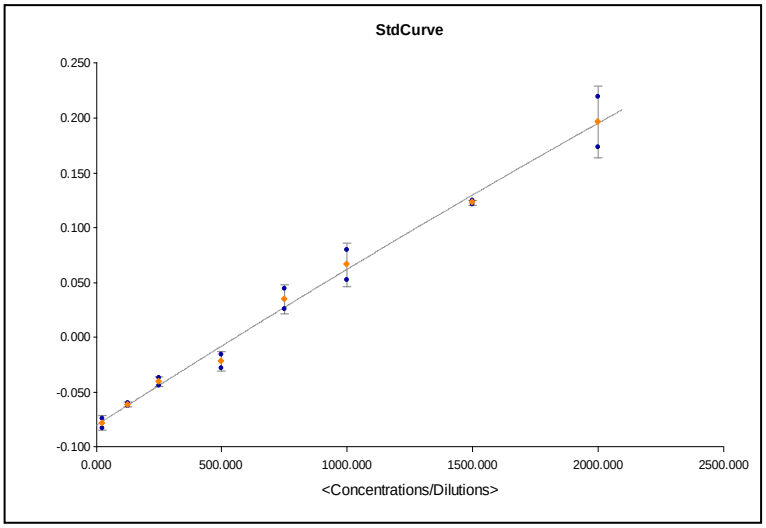

Figure VI. 1: Standard Curve for the BCA assay

Appendix VII –Full western blot image

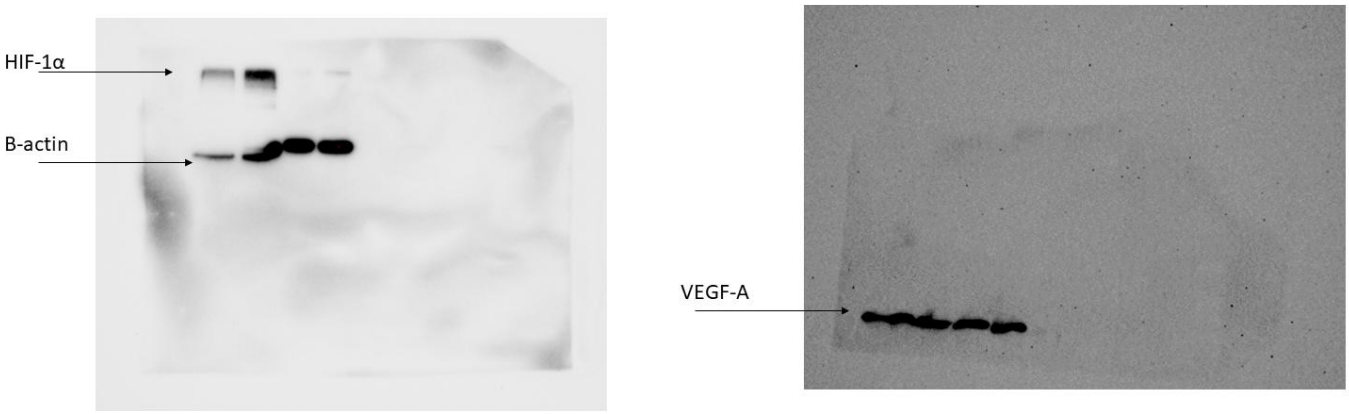

Figure VII.1: un-edited Imaged of western blot probed for HIF-1α and β-actin and reprobed after stripping for VEGF-A.